The Complexities on Ultra-Intense Laser Interaction with Plasmas

Baiwen Li

DOCTOR OF PHILOSOPHY

Department of Fusion Science
School of Physical Science
The Graduate University for Advanced Studies

2004 (School Year)

Abstract

The interaction of intense laser electromagnetic (EM) wave with plasma has become a basic and important problem in plasma physics due to its potential applications, ranging from astrophysics to fusion science. Inertial confinement fusion (ICF) has been considered as an attractive energy source, which motivates many scientists to pay much attention to the research of intense laser-plasma interactions. On the other hand, the particle acceleration by intense laser interacting with plasma also became a very attractive research topic because of its widespread applications, such as laser-induced nuclear reaction, particle acceleration, medical treatment, radiography and so on.

Intense laser pulse interacting with plasma is a source of various electronic instabilities. When an laser EM wave propagates in an underdense plasma, many electronic instabilities, such as stimulated Raman scattering (SRS) instability and stimulated Brillouin scattering (SBS) instability then can be excited and developed. These instabilities do not appear isolated but are often interconnected in the real intense laser-plasma interaction. In the past years, large efforts have been put into the studies of SRS and SBS, which produce energetic particles to preheat the core of a fusion pellet. Recently, a new type of stimulated scattering on the so-called Stimulated Electron-Acoustic Wave Scattering (SEAWS) instability was proposed by Montgomery et al., to reinterpret a underdense plasma data from the Trident laser facility. This novel SEAWS induced by relativistic laser interacting with a subcritical density plasma layer has been studied by Nikolić et al. by means of one-dimensional fully relativistic EM Particle In Cell (1D-PIC) simulations.

When an ultra-intense laser pulse propagates in a plasma, a dispersion effect comes to play an important role due to the finite inertia with which plasma particles respond to the high laser EM field, while plasma density redistribution is caused by the ponderomotive force that pushes the plasma particles away from the region of maximum EM field. These effects can lead to well-known nonlinear phenomena such as self-focusing, transparency of an overdense plasma and the generation of EM soliton. Relativistic solitons are EM structures self-trapped by locally modified plasma refractive index through the relativistic plasma particle mass increase and the plasma density redistribution by the ponderomotive force of an intense laser pulse. These solitons are generated behind the front of the laser pulse and are made of nonlinear, spatially localized low-frequency EM fields with a close to zero group velocity. A fairly large part of the laser pulse energy can be transformed into EM solitons. The formation mechanism and spatial structure

of EM soliton have been investigated by theoretical analysis and Particle-In-Cell (PIC) simulations. The solitons found in previous particle simulations consist of slowly or non-propagating electron density cavities inside which EM fields are trapped and oscillate coherently with frequencies below the unperturbed electron plasma frequencies. In homogeneous plasmas, solitons have been found to exist for a long time, close to the regions where they are generated and eventually decay due to their interaction with fast particles; as a result, the soliton energy is transformed into the fast particle energy. In inhomogeneous plasmas solitons are accelerated with the acceleration proportional to the plasma density gradient toward the low density side. When a soliton reaches some critical region, for example, the plasma-vacuum interface, it radiates away its energy in the form of a short burst of low-frequency EM radiation.

Particle acceleration by laser pulse propagating in plasmas has also become a very attractive research topic due to the advent of short-pulse, high-intensity lasers and their many potential applications. Various concepts of laser accelerators in a plasma, such as, beat-wave accelerator, laser wakefield accelerator, etc., are presently under discussion and investigation as possible approaches to accelerate to ultra-high energies. When an intense laser pulse propagates in underdense plasma, by backward and forward SRS, and other nonlinear processes e.g., the ponderomotive force of an intense laser pulse, a large amplitude electron plasma wave can be excited. This large amplitude plasma wave has a very high phase velocity close to the group velocity of a laser pulse, and can be used to accelerate electrons, protons or ions to high energies.

My research motivations come from inertial confinement fusion and particle acceleration. In the thesis, the researches are mainly concentrated on instabilities, relativistic EM soliton and electron acceleration, induced by linearly-polarized intense laser interacting with underdense plasmas, by means of fully relativistic EM 1D-PIC simulations.

The first part is the generation of accelerated large amplitude relativistic EM solitons in a long underdense homogeneous plasma. In simulations, ions are initially placed as a neutralizing background and are kept immobile. When laser enters the plasma layer, the first stage is dominated by SRS interactions. In our low density and long plasma condition, Stimulated Backward Raman Scattering (B-SRS) has shorter growth time than Stimulated Forward Raman Scattering (F-SRS). A nonlinear interplay between B-SRS and F-SRS produces a strong spatial modulation of the laser pulse. After that, there is typically the stimulated Raman cascade in the EM frequency spectra and wavenumber spectra both for backscattered and transmitted EM waves; which effectively scatter incident laser energy to higher order (Stokes and anti-Stokes) EM modes. In the later time, the continuing instability growth through stimulated Raman cascade downshifts the power maximum from the fundamental to the bottom of EM wave spectra. They clearly reveal a tendency of a transition from the stimulated Raman cascade regime to the regime of energy accumulation at the about electron plasma frequency, the so-called photon condensate. The cascade-to-condensate transition becomes more

pronounced with increasing laser intensity. After the photon-condensate process, the standing, backward- and forward-accelerated large amplitude relativistic EM solitons are observed. As a new research results, we found that the acceleration of EM soliton depends upon the incident laser intensity in a homogeneous plasma. The accelerated solitons are accelerated toward the plasma-vacuum interfaces and it radiate their energy in the form of low-frequency intense EM bursts. The frequency of the EM wave trapped inside soliton region is about the half of the unperturbed electron plasma frequency, while the corresponding ES frequency is about four and half times the unperturbed electron plasma frequency. The transverse electric and magnetic field have half- and one-cycle structure in space, while the corresponding ES field has one-cycle structure in space, respectively.

The second part is the generation of ion-vortices in phase-space in subcritical density plasmas ($n_{cr}/4 < n/\gamma < n_c$, γ - relativistic factor). When intense laser light enter a subcritical plasma, a stimulated trapped electron-acoustic wave scattering (T-SEAWS) instability takes place. It can be well-explained by a resonant three-wave parametric decay of the relativistic laser pump into the slowed Stokes EM wave with $\omega_s \sim \omega_{pe}$ and the trapped electron-acoustic wave (EAW) with $\omega_{eaw} < \omega_{pe}$ in the early stage, where ω_{pe} is the electron plasma frequency. There appear a rapid growth and strong localization of the Stokes wave by forming narrow intense EM soliton-like structures with downshifted laser light. The train of EM soliton-like structures get irradiated through the front vacuum-plasma boundary in a form of intense coherent reflection of the downshifted laser light. Large trapped EAW quickly heats up electrons to relativistic energies, which eventually suppresses the T-SEAWS instability. The ion dynamics does not play a significant role on the early physics behaviors of T-SEAWS. However, the ion wave created in the upstream region breaks in time and generates a large amplitude relativistic EM soliton in its breaking place. Thus this forms a large ES field inside. As a new phenomenon, we found that an ion-vortex (ion-hole) structure in phase-space is created because the large part of ions are accelerated and trapped by the regular EM and ES fields inside soliton. As this large amplitude EM soliton is accelerated in the backward direction, several ion-vortices in phase-space are generated due to the continuing ion acceleration and trapping.

In the third part of this thesis, the formation of high-quality and well-collimated return relativistic electron beam in long underdense homogeneous plasma is studied. A short ultra-relativistic electron beam acceleration by an intense laser pulse in a finite plasma is examined by 1D-PIC simulations. The mechanism is the combined effect of the electron acceleration by longitudinal field: synchrotron radiation source (SRS) and driven oscillatory relativistic electron plasma wave and the electrostatic (ES) Debye sheath field at the plasma-vacuum interface. The standard dephasing limit and the electron acceleration process are briefly discussed. The novel point is that, at relativistic laser intensities, a phenomenon of pushed short high-quality and well-

collimated return relativistic electron beam with thermal energy spread in the direction opposite to laser propagation, is observed. It operates like a two-stage accelerator. In the initial phase: rapid electron heating by the SRS driven relativistic plasma wave allows a massive initial electron blow-off into a vacuum. Large potential Debye sheath fields are created which further accelerate electrons (second stage) to ultra-relativistic beam energies. The mechanism of the beam formation, its characteristics and the time history in x and p_x space for selected test electrons in a beam, are analyzed and clearly exposed.

Contents

Chapter 1

Introduction

1.1 General overview

1.1.1 High intensity laser-plasma interaction

The research of the interaction between intense laser electromagnetic (EM) waves with plasmas is a basic problem and serves as an excellent introduction to the field of plasma physics. Both the linear and nonlinear theory of plasma waves, instabilities and wave-particle interactions are important for understanding the interaction of intense laser EM waves with plasmas [1]. The research on this problem has wide-spread applications ranging from astrophysics to fusion science. A lot of plasma phenomena have been observed in intense laser EM wave-plasma experiments, and many challenging problems still remain to be understood.

In the last 30 years, the research on laser-plasma interactions are of interest to many physics scientist. The most of motivations are mainly come from inertial confinement fusion (ICF), over this time, huge progresses in laser technology have been made. In addition to the research on ICF, the high-intensity laser pulse has other wide-spread applications, such as, particle acceleration, medical treatment, radiography, and so on.

Recent developments in high-intensity laser technology provide unique laboratory conditions for studies of nonlinear dynamics of ultra-intense laser-plasma interaction in a relativistic regime. Now it is possible to explore new kind of physical phenomena by creating extreme conditions in the laboratory.

On the other hand, in order to understand the problem of the laser-plasma interaction, computer simulation method, as a powerful tool, has been extensively used in the study of the interaction of intense laser pulses with plasmas. Not only, it can help us to understand physical phenomena clearly, but also, some new physical phenomena can be predicted by utilizing computer simulation method.

1.1.2 The development in high-intensity laser pulse technology

Inertial confinement fusion (ICF) as an attractive energy source has attracted much attention of many physicists to the ICF research in the past years. In order to realize the ignition of nuclear fusion fuel in ICF experiment by intense laser radiation, this extremely stimulated the development in high-power and ultra-short laser technology.

In Japan, at the Institute of Laser Engineering, Osaka University, a petawatt laser has been constructed for the purpose of the fast ignition in ICF fusion research. Current energy on target of this laser is $360J$ in $1ps$. In addition, as a heating laser of the imploded plasma for fast ignition concept, a four-beam petawatt laser, which energy up to $10kJ$ in $10ps$, will be developed [2].

In Europe, several facilities are utilized terawatt lasers with intensity $10^{18}-10^{21}W/cm^2$ and the pulse duration $30-750fs$ ($9-225$ wave periods), and several short petawatt pulse facilities are under construction [3]. These lasers at the peak of the pulse will deliver intensities about $10^{22}W/cm^2$ and duration of the pulses will be $500fs$ (150 wave periods).

In the United States, the National Ignition Facility (NIF) is under construction [4]. Its laser system will consist of 192 high-power laser beams with total energy 1.8×10^6J, wavelength $351nm$ (which is in near-ultraviolet range) and pulse duration $3ns$, planed for 2008. The facility will have two configurations to operate: "indirect drive", which directs half of the laser beams into two cones in the upper and lower parts of the target, and "direct drive", by moving beams into a more symmetric arrangement. It is expected that the laser beams will compress fusion targets to conditions to burn. Recently, there are extensive activities to study plasmas emulating conditions of NIF [5, 6, 7, 8].

Based on the interaction between such ultra-intense laser EM waves and plasmas, it is possible to generate the extremely high EM and electrostatic (ES) field, what never produced in the laboratory. For example, for intensity $I\sim10^{21}W/cm^2$ laser, the associated electric field is $E[V/m]=2.7\times10^3I^{1/2}[W/cm^2]\sim10^{14}V/m$, which is stronger than the electric field $E=5\sim10^{11}V/m$ that keeps an electron in the ground state of hydrogen atom. The interaction between such ultra-intense laser EM waves and plasmas, *there is no doubt*, can result in rich and complex nonlinear phenomena.

When an intense laser pulse propagates in a medium, the electrons in the atoms start to oscillate. For the laser intensities beyond $10^{10}W/cm^2$, these oscillations can become large enough to strip the electrons from the atoms [9]. For ions, they remain almost stationary due to their much higher mass, providing an ES force. As a result, the natural electron plasma oscillation will be caused with electron plasma frequency $\omega_{pe}=(e^2n/(\epsilon_0m_e))^{1/2}$, where e, n, ϵ_0 and m_e denote the electron charge, density, electric permittivity and the electron mass, respectively. As is known, the EM waves which propagate inside plasma have dispersion relation $\omega_0^2=\omega_{pe}^2+k_0^2c^2$, where ω_0, k_0 and c

are EM wave frequency, wavenumber and the velocity of light, so the electron plasma frequency ω_{pe} is the minimum frequency for EM waves propagation in a plasma, in other words, in a cold and nonrelativistic plasma, EM waves cannot propagate through a plasma of density $n > n_{cr}$, here, $n_{cr} = n(\omega_0/\omega_{pe})^2$ is the critical density or cutoff density for laser propagation. However, at high laser intensity, the velocities of free electrons oscillating with laser EM field close to the speed of light c, which causes a relativistic increase of electron mass, namely, $m_e \rightarrow \gamma m_e$, here $\gamma = (1 - v^2/c^2)^{-1/2} = (1 + a_0^2)^{1/2}$ is the relativistic Lorentz factor and $a_0 = \gamma v_{osc}/c$ is the normalized vector potential. The relativistic increase of electron mass will result in the decrease of the electron plasma frequency.

The ratio between the quiver velocity v_{osc} and the speed of light c defines the laser amplitude,

$$a = \frac{eE_0}{m\omega_0 c} = \frac{v_{osc}}{c} = 0.85 \times 10^{-9}\lambda[\mu m]I^{1/2}[W/cm^2] \tag{1.1}$$

where E_0 is the amplitude of the laser electric field.

1.2 Instabilities in laser-plasma interaction

The interaction of high intense laser EM waves with plasmas has been the subject of experimental investigations for many years [10]. Many experiments have been focused on measuring a broad range of phenomena, such as resonance and collisional absorption, filamentation, density profile and particle distribution modification, and the growth and saturation of various parametric instabilities. These phenomena depend on both the properties of the laser (its intensity, wavelength, pulse length coherence, etc.) and the composition of the plasma. Motivated by laser-driven ICF, experimental studies of laser-plasma instabilities have become particularly important in recent years. The success of ICF depends partly on mitigating the undesirable effects of two particular parametric instabilities, stimulated Raman scattering and stimulated Brillouin scattering.

These two instabilities are of particular importance because both degrade the target compression efficiency in a spherical implosion experiment. Electron Landau damping from the stimulated Raman scattering (SRS) instability produces fast electrons that can preheat the core of an imploding sphere prior to the arrival of the compression shock front [11]. The stimulated Brillouin scattering (SBS) instability can scatter a substantial fraction of the incident laser light, causing an overall reduction in the laser-to-X-ray drive efficiency and modifying the X-ray drive symmetry. In addition to SRS and SBS, other instabilities, *such as, two-plasmon decay, decay of incident EM wave into an electron plasma wave (EPW) plus an ion acoustic wave (IAW)*, etc., can be also excited by high-intensity laser EM wave propagating through underdense plasmas.

These instabilities can be simply described as the resonant decay of the incident laser EM wave into two other waves. The three-wave interaction is the lowest-order nonlinear effect for a system approximately described by a linear superposition of discrete waves. The frequencies and wave vectors for three-wave interaction satisfy the following conditions.

$$\omega_0 = \omega_s + \omega_p \tag{1.2}$$

$$\mathbf{k_0} = \mathbf{k_s} + \mathbf{k_p} \tag{1.3}$$

where ω_0, ω_s and ω_p stand for the frequencies of incident EM, scattered EM and plasma waves, while k_0, k_s and k_p represent the their corresponding wave numbers, respectively.

When the incident laser amplitude exceeds a threshold value which corresponds to a certain instability, the remaining two waves which are start growing at noise level initially by absorbing energy from the incident laser EM wave. In fact, these instabilities do not appear isolated but are often interconnected other. Laser pulse will lose large part of its energy by these instability processes.

According to plasma density, these instabilities can be classified. For example, around the incident laser critical density n_{cr} laser EM wave can decay into an EPW and an IAW. When plasma density near $0.25n_{cr}$, two-plasmon decay ($2\omega_p$ instability) occurs by laser EM wave decaying into two EPWs. When plasma density below $0.25n_{cr}$, stimulated Raman scattering (SRS), *a decay of incident laser EM wave into a scattered EM wave plus an EPW*, can grow. In the case of plasma density $n < n_{cr}$, stimulated Brillouin scattering (SBS), *an incident laser EM wave coupling to a scattered EM wave plus an IAW*, can take place.

Recently, a new type of stimulated scattering, the so-called stimulated electron-acoustic wave scattering (SEAWS), has been reported in experiment [12, 13] and studied by particle simulation [14, 15, 16, 17].

1.2.1 Stimulated Raman scattering (SRS)

The stimulated Raman scattering (SRS) can be most simply characterized as the resonant decay of an incident laser EM wave (ω_0, k_0) into a scattered EM wave (ω_s, k_s) plus an electron plasma wave (EPW) (Langmuir wave) (ω_{epw}, k_{epw}). The matching conditions for frequencies and wave numbers are as follows

$$\omega_0 = \omega_s + \omega_{epw}, \quad k_0 = \pm k_s + k_{epw} \tag{1.4}$$

where the wave numbers for the EM waves have

$$k_0 = \frac{\omega_0}{c}(1 - \frac{n}{n_{cr}})^{1/2}, \quad k_s = \frac{\omega_s}{c}(1 - \frac{\omega_{pe}^2}{\omega_s^2})^{1/2} \tag{1.5}$$

Here, "+/−" in $\pm k$ in the equation (1.4), denote stimulated Raman forward and backward scattering (F-SRS/B-SRS), respectively. n and $n_{cr} = n(\omega_0/\omega_{pe})^2$ are the plasma density and critical density, respectively. $\omega_{pe} = (e^2 n/\epsilon_0 m_e)^{1/2}$ and $\omega_{epw} = (\omega_{pe}^2 + 3k_{epw}^2 v_{the}^2)^{1/2}$ are the electron plasma frequency and Bohm-Gross frequency of EPW, respectively. The $v_{the} = (T_e/m_e)^{1/2}$ is the electron thermal velocity, T_e is the temperature.

Since an EM wave propagating in a plasma has dispersion relation $\omega_0^2 = \omega_{pe}^2 + k_0^2 c^2$, the minimum frequency of an EM wave in plasma is the electron plasma frequency ω_{pe}. Thus, SRS instability requires the condition

$$\omega_0 \geq 2\omega_{pe} \implies n \leq n_{cr}/4 \tag{1.6}$$

It should be noted that this condition can be shifted to higher densities because the high-intensity laser EM wave causes a relativistic increase of electron mass $m_e \rightarrow \gamma m_e$ (γ is relativistic Lorentz factor), which reduces the frequency of EPW.

By SRS instability, ω_s/ω_0 part of the incident energy is scattered and ω_{epw}/ω_0 part is deposited into the EPW. When EPW damps, this portion of the energy will heat the plasma. This EPW has a very high phase velocity of the order the light velocity, so it can produce very energetic electrons, such electrons can preheat the fuel in laser fusion application. Therefore SRS instability is particularly significant concern in ICF research.

The phase velocity of EPW produced during SRS process can be slow enough to reach back into the tail of the background electron Maxwellian distribution function. The tail electrons trapped by the EPW can obtain energy from the EPW and therefore damp it. When the phase velocity of EPW for low density is $v_{ph} \approx \omega_{epw}/2k_0$, then the B-SRS occurs dominantly. For F-SRS, because its the phase velocity is nearly the speed of light, in initial electron Maxwellian distribution function, a very low number of electrons have initial energy to be trapped. When the laser EM wave propagates through a plasma for long enough distance, a large amplitude EPW can produces a significant number of high energetic electrons [9].

When a relativistic laser propagates in an underdense plasma, B-SRS and F-SRS can develop [18, 19]. They do not appear isolated but are often interconnected. A nonlinear interplay between B-SRS and F-SRS produces a strong spatial modulation of the laser pulse and the stimulated Raman cascade in its frequency spectrum. The continuing instability growth through stimulated Raman cascade downshifts the pulse frequency from the fundamental to the bottom of the EM wave spectra. The spectra of F-SRS clearly reveal the Raman cascade containing not only the first-, second- and higher-order Stokes modes, but also the first-, second- and higher-order anti-Stokes modes. It gets saturated by the photon condensation mechanism, related to strong depletion and possible break-up of the laser beam. In the final stage of the cascade-into-condensation process, the depleted downshifted laser pulse gradually transforms into a train of ultra-

short relativistic EM solitons [18, 19].

1.2.2 Stimulated electron-acoustic wave scattering (SEAWS)

Electron-acoustic wave (EAW), as a mode of plasma waves, it has been studied by early authors. By examining the linearized Vlasov ES dispersion relation and ignoring particle trapping effect, they obtained EAW solutions with dispersion relation in the long wavelength limit $\omega \approx 3.6kv_{the}$, where ω, k and $v_{the} = (T_e/m_e)^{1/2}$ are the frequency, wave number and the electron thermal velocity, respectively [20, 21, 22]. The phase velocity $v_\phi = \omega/k$ of EAW is between the weakly damped slow phase velocity IAW ($v_\phi/v_{the} \ll 1$) and the high phase velocity EPW ($v_\phi/v_{the} \gg 1$). Since the EAW has large linear damping with Maxwellian distributions, $-Im(\omega)/Re(\omega) \geq 1$ [20, 22], it often were neglected. However, other analytical studies of nonlinear Vlasov-Maxwell solutions have been found that strong electron trapping can occur even for small amplitude ES wave, resulting in undamped nonlinear traveling wave solutions, the so-called BGK (Bernstein-Greene-Kruskal) modes, allowing the EAW with a lower phase velocity $\omega \approx 1.31kv_{the}$, *which is compared to the least-damped linear EAW solution* $\omega \approx 3.6kv_{the}$, to exist [23, 24, 25].

The stimulated electron-acoustic wave scattering (SEAWS), *as a novel stimulated scattering*, was proposed by Montgomery et al., in the recent single hot spot experiment to reinterpret an underdense homogeneous plasma experiment data from the Trident laser facility [12, 13]. In their experiments, plasma density $n \approx 0.03n_{cr}$, temperature $T_e \approx 350Ev$, plasma length $L_p \approx 900c/\omega_0$, laser intensity $I \approx 1.6 \times 10^{16}W/cm^2$, respectively, where ω_0 is laser frequency. They observed a wave signal in the backscattered spectra with phase velocity $v_{ph} \approx 1.4v_{the}$ besides the first backscattered EM signal which comes from the SRS. It was shown, that among electronic instabilities, stimulated scattering of laser light from the trapped EAW with frequency $\omega < \omega_{pe}$ can possibly explain the second anomalous backscatter signal. However, in these experiments, the signal ratio of SEAWS to SRS was reported smaller than 10^{-3}.

Similar to the SRS instability, the SEAWS can also be explained as three-wave resonant decay of an incident laser EM wave (ω_0, k_0) into a scattered (Stokes) EM wave (ω_s, k_s) plus an EAW (ω_{EAW}, k_{EAW}). When this instability takes place, the corresponding matching conditions for the wave frequencies and wave numbers will satisfy as follows:

$$\omega_0 = \omega_s + \omega_{EAW}, \quad \mathbf{k_0} = \mathbf{k_s} + \mathbf{k_{EAW}} \tag{1.7}$$

By a linearly-polarized intense laser pulse interacting with a plasma layer at a sub critical density range, $n_{cr}/4 < n/\gamma < n_{cr}$ *(γ - relativistic factor), which are overdense for standard SRS*, this novel SEAWS has been studied by means of one-dimensional fully relativistic EM particle-in-cell (1D-PIC) simulations [14, 15, 16, 17]. In the early stage, the frequency spectra can be well explained by a resonant 3-wave parametric decay of

the relativistic laser pump into the slowed ($\sim$ "critical") Stokes light sideband $\omega_s \sim \omega_{pe}$ and the trapped electron-acoustic wave (T-EAW) with $\omega_{eaw} < \omega_{pe}$.

Recently, we also put some attention on this novel SEAWS instability. We found that in its nonlinear saturation, there is a rapid growth and strong localization of the Stokes wave by forming narrow intense EM soliton-like structures with (downshifted) laser light trapped inside. The train of relativistic EM solitons-like gets irradiated through the front vacuum-plasma boundary in a form of intense coherent reflection of the downshifted laser light. Large T-EAW excited in the plasma quickly heats up electrons to relativistic energies which eventually suppresses the instability in our simulations.

The physics of the SRS and SEAWS instabilities are straight forward. For example for SRS [1], consider a laser EM wave propagating through a plasma with density ripple along the direction of laser propagation by the density fluctuation δn associated with an EPW. Because the electrons are oscillating in the laser electric field $\mathbf{E_0}$ with the velocity $\mathbf{v_L} = -\mathbf{eE_0/m\omega_0}$, a transverse current $\delta\mathbf{J} = \mathbf{ev_L}\delta\mathbf{n}$ is generated. If the numbers and frequencies are properly matched, this transverse current generates a scattered light wave with an amplitude δE. In turn, this scattered light wave interferes with the incident laser wave to produce a variation in the wave pressure: $\nabla(\mathbf{E^2}/8\pi) = \nabla(\mathbf{E_0} \cdot \delta\mathbf{E})/4\pi$. Variations in wave pressure act just like variations in the ordinary kinetic pressure i.e., plasma is pushed and density fluctuation is generated. Duo to this feed-back loop, an instability is possible. A small density fluctuation leads to a transverse current which generates a small scattered EM wave which can in turn reinforce the density fluctuation via a variation in the wave pressure.

1.3 Relativistic electromagnetic solitons

1.3.1 Solitary wave (soliton)

As is well-known, solitons are nonlinear waves. As a preliminary definition, a soliton is considered as solitary, traveling wave pulse solution of nonlinear partial differential equation (PDE), and this solution is spatially localized and keeps its form. The nonlinearity plays a significant role. For most dispersive evolution equations these solitary waves would scatter inelastically and lose 'energy' due to the radiation. Apart from the nonlinearity, the stability also plays an important role in soliton physics: after a fully nonlinear interaction, the solitary waves re-merge, retaining their identities with same speed and shape. This is of particular importance, it means specifically that solitons can exist only in conservative media.

Solitons, as a localized nonlinear objects, were first discovered by Scott Russell in 1834 on the surface of liquids [28, 29], for a long time, they remained of interest only for a small number of specialists in hydrodynamics and mathematics who tried to prove their

existence. In the late 50's of last century the soliton concept penetrated into plasma physics. Here due to work by Sagdeev [30], Gardner and Morikawa [31] and others, solitons were successfully used to construct the theory of a fine structure of shock waves under the conditions of rare collisions. Nowadays a great number of soliton types in plasma are known. They are widely used for various theoretical speculations, especially for the construction of different versions of strong turbulence theory. In order that these speculations should be real it is necessary for the considered solitons to be stable. Therefore the problem of soliton stability is of particular importance [32].

Solitons can be classified by two types, *the simple solitons and the oscillating solitons.* Simple solitons are solitary waves whose profile with stationary localized structure; while, for oscillating solitons, the different from that the simple solitons is, inside the oscillating solitons, there occur oscillations characterized by definite frequency and wavelength, such a soliton profile is, in the mean, stationary in some reference system [32].

It is well-known that a comparatively small number of mathematical models possessing a great degree of universality play a very important role in soliton theory. Such are, for example, the Korteweg-de-Vries (KdV) equation and the Kadomtsev-Petviashvili (KP) equation describing simple solitons, while, the nonlinear Schrödinger (NLS) equation which is the simplest model for defining oscillating solitons [32]. The universal nonlinear models well-known nowadays are such as the KdV and the NLS equation [33, 34, 35, 36, 37, 38]. Their universality is explained by the fact that they describe a wide spectrum of phenomena in various nonlinear media.

1.3.2 KdV equation

The equation describing the (unidirectional) propagation of waves on the surface of a shallow channel was derived by Korteweg and de Vries in 1895. The KdV equation arises when describing weakly nonlinear waves in media with a dispersion law $\omega(k)$ which is close to the linear one, in the linear approximation in the amplitude, standard form of KdV equation is as follows:

$$u_t + u_{xxx} + 6uu_x = 0 \tag{1.8}$$

The second and third terms in equation (1.8) stand for the dispersion effect and the nonlinear effect of wave, respectively. A solution of stationary solitary wave (soliton), $u = 2\kappa^2/cosh^2\kappa(x - 4\kappa^2 t - x_0)$, is the simplest solution of the KdV equation [32]. It plays a fundamental role in the evolution problem for an arbitrary initial distribution. The KdV equation can admit also a multi-soliton solution.

In multi-dimensional cases the well-known Kadomtsev-Petviashvili (KP) equation [39] is a natural generalization of the KdV equation. The KP equation can be obtained if a characteristic transverse scale of (sound) disturbances is assumed to exceed significantly

to the longitudinal size and it has the following standard form.

$$\frac{\partial}{\partial x}(u_t + u_{xxx} + 6uu_x) = -3\beta^2(\frac{\partial^2 u}{\partial y^2} + \frac{\partial^2 u}{\partial z^2}) \tag{1.9}$$

For ion-acoustic wave cases, in the linear approximation in the amplitude, $c_s(u) = c_s(1 + \beta u)$, βu is small as compared to unity. All changes in comparison with the KdV equation are connected only with an additional term on the right-hand side, which describes the acoustic wave diffraction in the transverse direction.

1.3.3 Nonlinear Schrödinger (NLS) equation

The nonlinear Shrödinger equation (NLS) is usually used for the description of the propagation of wavepackets with a small amplitude, i.e., when the field weakly from a harmonic one and nonlinear effects are small. This gives an opportunity to take into account dispersion and nonlinear effects separately for the derivation of the equation. The standard form of NLS equation [40] is as follows:

$$i\psi_t + \nabla^2\psi + f(|\psi|)\psi = 0 \tag{1.10}$$

With rather general nonlinearity $f(|\psi|)$. The second term stands for the dispersion effect of media. Here $\psi(\mathbf{x}, t)$ is a slowly varying envelope of the electric field, and $\mathbf{x}$ and t have different meanings depending on the physical context.

In all cases the function $f(|\psi|)$ characterizes nonlinearity, e.g., the nonlinear correction to the refractive index of media. For many physical problems this function can be approximated by a power-law dependence, $f(|\psi|) \sim |\psi|^{2p}$, and for the particular case of the Kerr nonlinearity $p = 1$ [40].

This NLS equation has a solution in the form $\psi(\mathbf{x}, t) = exp(i\lambda^2 t)g(\mathbf{x})$ with the function g is determined by the following equation:

$$-\lambda^2 g + \bigtriangledown^2 g + g^3 = 0$$

Such a type of solution with the multiplier oscillating in time is natural, because the interaction leads to a nonlinear frequency shift λ^2 general for all harmonics. The dynamics of solitons of NLS equation in the uniform media has been studied in detail [33, 41, 42].

The KdV equation, KP equation and NLS equation have been extensively used to investigate the existence of soliton, soliton stability against perturbations and the temporal evolution of soliton solution [32].

It is should be noted here, the research on these problem has been extended our attentions, our interests are concentrated on relativistic EM soliton induced in intense laser-plasma interaction.

1.3.4 Relativistic EM solitons in laser-plasma interaction

High-intensity laser propagating in an underdense plasma, in addition to the instabilities, causes rich and diverse nonlinear phenomena, which enrich our physics and make it more colorful.

When a relativistically intense laser propagates inside underdense plasma, first, dispersion effects plays an important role due to the plasma particle mass relativistic increase by responding to the intense laser EM field; second, the nonlinearity appears due to the plasma density redistribution under the action of the ponderomotive force of the intense laser EM field, that pushes the plasma particles away from the region of the maximum EM field [43]. These effects can lead to well-known nonlinear phenomena, such as, relativistic self-focusing [26, 44, 45, 46, 47, 48, 49], relativistic transparency of an overdense plasma [50, 51], and the generation of relativistic EM soliton [52, 53].

High-intensity laser EM wave can cause a relativistic increase of plasma electron mass $m_e \rightarrow \gamma m_e$, which reduces the critical density from n_{cr} to $n_{cr}/\gamma^{1/2}$. This results in the relativistic transparency of intense laser in overdense plasma, i.e., intense laser can also propagate in overdense plasma density region between n_{cr} and $n_{cr}/\gamma^{1/2}$ [50, 51].

The power threshold for relativistic self-focusing of the laser beam is given by [26]

$$P = \frac{2m^2c^5\omega_0^2}{e^2\omega_{pe}^2} \approx 17\frac{\omega_0^2}{\omega_{pe}^2}GW \tag{1.11}$$

The simulation results have shown that the relativistic self-focusing can enhance the laser intensity ten-fold [27]. When the laser intensity exceeds the power threshold significantly, the laser beam can split into filaments [54].

Among nonlinear modes, solitons are of fundamental importance for basic nonlinear science [34, 55]. EM solitons with relativistic amplitude were first investigated by V. A. Kozlov, A. G. Litvak and E. V. Suvorov [56]. Solitons were predicted to occur in laser produced plasmas and were found by PIC simulations. The relativistic solitons are self-trapped, finite size, EM wave that propagates inside plasma without diffraction spreading. Self-trapping appears because EM wave modifies the local refractive index through the relativistic plasma particle mass increase and the plasma density redistribution [57, 58, 59]. These solitons are generated behind the front of the laser pulse and are made of nonlinear, spatially localized low-frequency EM fields with a close to zero group velocity. It was shown that the soliton formation is a significant channel of laser pulse energy transformation [60]. A fairly large part of the laser pulse energy can be transformed into solitons. Nearly $30 \sim 40\%$ of the laser energy can be trapped in the solitons [52, 53]. This fairly high efficiency of EM energy transformation indicates that solitons which are an essential component of turbulence in plasmas together with the vortices [61, 62, 63] can play an important role in the development of the interaction between the laser pulse and the plasma. The research on EM soliton is active and important topic in

laser plasma interaction. Recently the research on solitons has received much attention because they are of fundamental importance in nonlinear science [55] and are considered to be essential components of turbulence in a plasma [58, 18].

The mechanism of relativistic EM soliton formation and its structure were analytically investigated and observed by particle simulation in the interaction of ultra-intense laser radiation with underdense [64, 65, 66, 67] and overdense plasmas [68, 52, 69].

The analytical theory of relativistic EM soliton has been developed mainly within the framework of immovable ions and including some other approximations. For example, Lj. Hadžievshi, M. S. Jovanović, M. M. Škorić and K. Mima, by considering a weakly relativistic limit, cold plasma condition and neglecting ion dynamics, they obtained an nonlinear Schrödinger (NLS) equation with two nonlocal (derivative) nonlinear terms [58]. By using this nonlinear Schrödinger equation, the existence and stability of 1D EM solitons formed in a relativistic interaction of a linearly polarized laser light with an underdense cold plasma are discussed, and the standing EM soliton solutions with maximum amplitude $\mathbf{A}_s \approx 2.7$ and frequency $\omega_s \approx 0.73\omega_0$, are analytically shown to be stable in agreement with the model simulation.

An exact analytical solution of the electron Fluid-Maxwell equations representing one-dimensional (1D) circularly polarized relativistic EM subcycle soliton obtained in Ref. [70] is in perfect agreement with 1D-PIC simulations. When the ion dynamics is taken into account, solitons have been found to exist by analytically research [57, 71] and by particle simulation [72, 73].

As shown in the figure 1.1, *the sketch for the plasma density n/n_0 and the energy density of EM field $E^2 + B^2$ plots.* The solitons found in 1D and 2D particle simulations consist of slowly or non-propagating electron density cavities inside which an EM field is trapped and oscillates coherently with a frequency below the unperturbed electron plasma frequency and with spatial structure corresponding to half a cycle (subcycle soliton) [70, 72]. This is the main characteristics of the relativistic EM soliton. The interaction of two 2D solitons leads to their merging and the resulting soliton obtains the total energy of the two merged solitons [62]. When ion dynamics is considered, 2D soliton evolves into a postsoliton on the ion time-scale due to the ion acceleration caused by the ES field inside the soliton. As a result, a substantial part of the laser pulse energy can be converted into solitons which afterwords evolve into postsolitons [43, 72].

1.3.5 The acceleration of relativistic electromagnetic solitons

It is reported that solitons have been found to exist for a long time close to the regions where they are generated in a homogeneous plasma, and with time goes on, eventually decay due to their interaction with fast particles. In this process, the energy of solitons is transfered to the fast particles. Since a real plasma is usually inhomogeneous, solitons

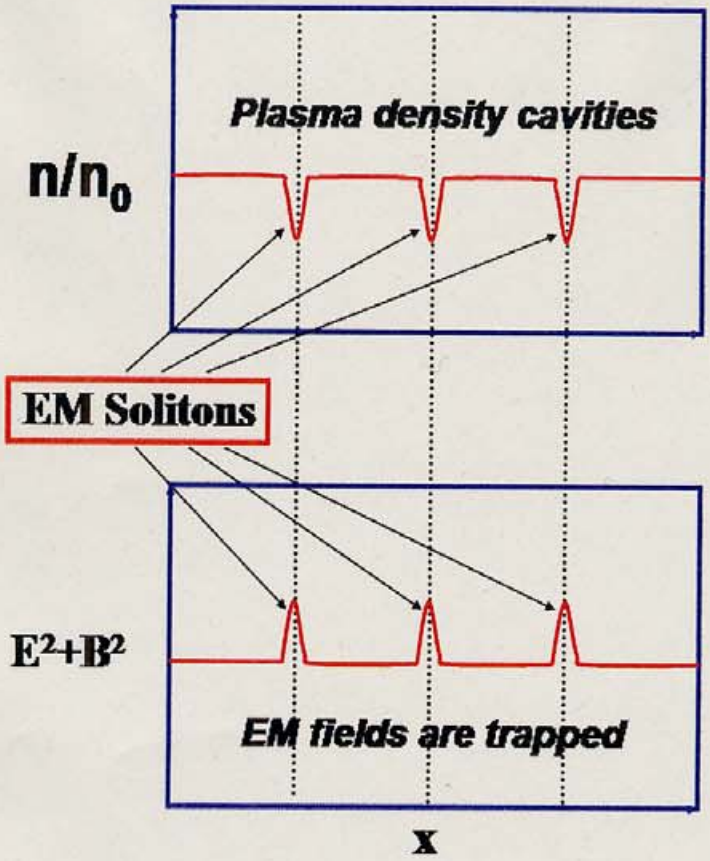

Figure 1.1: The sketch for the plasma density n/n_0 and the energy density of EM field $\mathbf{E^2} + \mathbf{B^2}$ plots, respectively.

are accelerated with the acceleration proportional to the gradient of the plasma density towards the low density side. When a soliton reaches some critical plasma region, for example, the plasma-vacuum interface, it radiates away its energy in the form of a short burst of low-frequency EM radiation [62, 74].

In a nonuniform dispersive medium, a wavepacket moves according to the well-known equations of geometric optics equations.

$$\frac{dx_i}{dt} = \frac{\partial H}{\partial k_i} \quad and \quad \frac{dk_i}{dt} = -\frac{\partial H}{\partial x_i} \tag{1.12}$$

The equations have a Hamiltonian form, which is the wave frequency $H(x_i, k_i) = \omega$. From these equations, it is found that the acceleration of the wavepacket is equal to [62].

$$\frac{d^2x_i}{dt^2} = -\frac{\partial^2 H}{\partial k_i \partial k_j}\frac{\partial^2 H}{\partial x_j} + \frac{\partial^2 H}{\partial k_i \partial x_j}\frac{\partial^2 H}{\partial k_j} \tag{1.13}$$

For the EM wave in a plasma, $H(x_i, k_i) = (k^2c^2 + \omega_{pe}^2)^{1/2}$. For example, in the case of the plasma density given by $n(x, y) = n_0(1 + x/L_x + y^2/2L_y^2)$, it is easily to obtain

the acceleration of soliton $\ddot{x}= -c^2/2L_x$ and $\ddot{y}= -c^2y/L_y^2$. Therefore, the wavepacket is accelerated along the x axis from the high density side toward low density side, and at the same time, it oscillates in the transverse direction with frequency c/L_y [62, 74].

In fact, the motion of relativistic EM soliton depends upon the motion of the particle (electrons or ions) in the soliton. In the nonlinear relativistic case, basically, the longitudinal particle motion is determined by the balance of the ES field and the ponderomotive force terms [58, 18], in the normalized units,

$$\partial p_x/\partial t = -E_x - \partial\gamma/\partial x \tag{1.14}$$

Here, p_x, E_x and γ stand for the momentum, ES field and relativistic factor, respectively.

Which direction, *forward or backward*, the relativistic EM soliton can be accelerated, depends upon, which term, *ES field or ponderomotive force*, is prevailing inside soliton. It should be noted that the two terms are the averaged effect of all particles inside soliton.

1.3.6 Bright soliton and dark soliton

It is well-known that nonlinear downshifting of the wave frequency corresponds to the breakup of a homogeneous wave into bright solitons. On the other hand, nonlinear frequency upshifting manifests the possibility of dark soliton formation [71]. There, namely, are two distinct types of localized solitons, *bright soliton or dark soliton.* These two types of solitons are in fact very different. They have completely different nature and result from quite different physics [76]. Both bright soliton and dark soliton have a minimum of the plasma density. The difference is followings; the bright soliton has a maximum of the EM energy density, while the dark soliton has a minimum of the EM energy density [71]. Dark solitons are known to exist in optical system [76] and they were also observed in the Bose-Einstein condensation [77].

In this thesis, we are only concentrated on bright ones, because of their resilient and robust behaviors and their importance in the research of intense laser-plasma interaction.

1.4 Particle acceleration by laser-plasma interaction

Particle acceleration by intense laser EM fields propagating in plasmas has recently become a very attractive research topic after the advent of short-pulse and high intensity lasers due to their many potential applications. Various concepts of laser accelerators in a plasma, such as, beat-wave accelerator [78, 79], laser wakefield accelerator [80, 81, 82], electron beam wakefield accelerator [83, 84] and plasma accelerator of photon beams [85, 86], are presently under discussion and investigation as possible approaches to accelerate to ultra-high energies.

High-energy particles and high-quality, well-collimated particle beams have wide potential applications, in the concept of fast ignition in ICF research [88], laser induced nuclear reaction [89], medical treatment, radiography and so on. Stochastic heating and acceleration of electrons by two counter-propagating laser pulses have been also studied by some authors [90, 91, 92, 93].

In recent years, much attention on particle acceleration has been paid by theoretical analysis, particle simulation and experiment.

When an intense laser propagates in an underdense plasma, by B-SRS/F-SRS and other nonlinear laser-plasma interaction processes, e.g., the ponderomotive force of an intense laser EM field, a large amplitude EPW can be excited behind the front of the laser pulse. Such relativistic electron plasma waves (EPWs) are also generated by a beat-wave scheme, which requires two laser beams and a plasma frequency precisely tuned to their frequency difference. This large amplitude EPW has a very high phase velocity close to the group velocity of the laser pulse and can be used to accelerate electrons, protons or ions to high energies. In underdense plasma, fast electron distributions peaked in the direction of laser propagation with the thermal energy spectra are observed. One finds two populations with two distinct temperatures. At present, there exists no clear understanding of above phenomenon in the literature.

Ion acceleration by soliton also has been studied. This is caused by the energy gain during the ion interaction with the EM field and/or ES field trapped inside soliton. Soliton propagating with high velocity provides the wakeless regions with regular electric and magnetic fields, with which the particle can interact and gain the energy, and the soliton energy transforms into the energy of the fast particles [57]. Ion acceleration in a soliton produced by shock-wave decay in a plasma slab irradiated by an intense laser pulse has been studied via PIC simulation [111].

1.5 Particle-in-cell (PIC) simulation

1.5.1 Computer simulation

The investigation of phenomena by computer simulation is now an established and rapidly growing practice in scientific research and engineering design. Computer simulation may be regarded as the theoretical exercise of numerically solving an initial-value-boundary-value problem [94]. By selecting the suitable mathematical models according to the behavior of complex system and by fixing the computational box with the selecting initial and boundary conditions, simulation then can be done to follow the temporal evolution of the configuration.

In order to understand complex plasma phenomena, computer simulation by using particle codes has been thought is a very direct and powerful approach, particularly for investigating kinetic and nonlinear effects. The approach is extremely simple, numerically follow the motion of a large collection of charges in their self-consistent electric and magnetic fields to simulate evolution for a plasma system by using mathematical equations that basically describe the system on an accepted physical level. Computer simulation enables us to set up a numerical plasma experiment with detailed diagnostics to investigate plasma complexity. Such numerical experiment can help us to understand the results from the real ones. Computer simulation also can be set-up for these experiments, which can not be performed in the laboratory either due to their size or due to the characteristic time scale of certain physical processes.

Although simulations have many advantages, they are still limited by computer capabilities and by our chosen simple initial and boundary conditions, they can not become the substitution for laboratory and space experiments and observations [9]. Nevertheless, computer simulations fill large gaps between theory and experiments. It is possible to obtain more detailed information of complex plasma processes by combining three approaches, i.e., theory, experiment and simulation.

Based on fluid or/and kinetic description of plasma system, various simulation schemes, such as, magneto-hydro-dynamics (MHD) code, hybrid code, etc., have been introduced and developed in plasma physics. MHD simulation code has been used to solve and investigate the fluid equations of plasma, while, the goal of Vlasov and PIC simulation codes are to illustrate the motion of charged particles, based on plasma kinetic (Vlasov) equation. The hybrid code is a combination of these two approaches: *fluid and kinetic descriptions.*

1.5.2 Particle-in-cell (PIC) simulation

Vlasov simulations and PIC simulations have been developed and extensively used in laser inertial confinement fusion (ICF) researches. The advantage of Vlasov simulation method is, it has lower noise level than PIC simulation. However Vlasov simulations are very expensive in the investigation of the interactions between high intensity wave and plasma due to the large phase space required for simulation. Now one prefers to use PIC simulations in laser-fusion researches. Relativistic EM PIC simulations are powerful tool in intense laser-plasma interaction [95, 96]. The approach is numerically follow the motion of a large collection of charges (*electrons and ions*) interacting through their mutual electric and magnetic fields ($\mathbf{E}$ and $\mathbf{B}$). The motion of the charge q is determined by Newton-Lorentz equation,

$$\frac{d(\gamma \mathbf{v})}{dt} = \mathbf{F} = q(\mathbf{E} + \mathbf{v} \times \mathbf{B}) \tag{1.15}$$

where γ, $\mathbf{v}$ and $\mathbf{F}$ are the relativistic factor, velocity and Lorentz force of charged particle, respectively. The fields are related to the charge density ρ and current density $\mathbf{j}$ by Maxwell's equation, with the following vacuum form:

$$\nabla \cdot \mathbf{E} = \frac{\rho}{\epsilon_0} \tag{1.16}$$

$$\nabla \cdot \mathbf{B} = 0 \tag{1.17}$$

$$\nabla \times \mathbf{E} = -\frac{\partial \mathbf{B}}{\partial t} \tag{1.18}$$

$$\nabla \times \mathbf{B} = \mu_0 \mathbf{j} + \frac{1}{c^2}\frac{\partial \mathbf{E}}{\partial t} \tag{1.19}$$

Where ϵ_0 and μ_0 are the electric permittivity and magnetic permeability, $c = (\epsilon_0 \mu_0)^{-1/2}$ is the speed of light in vacuum, respectively.

In PIC simulation, the plasma is represented by a large number of quasi-particles, by using quasi-particles to simulate the action of a large number of physical particles. In the simulation, the particle coordinates and particle velocities remain continuous quantities, while, the electric fields, magnetic fields, charge densities and current densities are discretized on a spatial grid. The choice of the appropriate initial and boundary conditions in simulation are based on the physical problem which is under the investigation, the simulation can be started with chosen initial conditions, i.e., the particle positions, particle velocities and external fields, etc.

The basic simulation cycle is illustrated in figure 1.2. From the particle positions and velocities $(\mathbf{x}, \mathbf{v})$ at every given time step, to compute the charge and current densities

$(\rho, \mathbf{j})$ on a spatial grid sufficiently fine to resolve the collective behaviors. Then, using the charge and current densities to compute the self-consistent electric and magnetic fields $(\mathbf{E}, \mathbf{B})$ via Maxwell's equations. Next, by using these fields to calculate the Lorentz force $\mathbf{F}$, after that, by using Newton-Lorentz equation to advance the positions and velocities of the charges. Finally, by continuing to run around this basic cycle with a time step sufficiently small, to resolve the physical problem with a accepted level.

$$\begin{array}{ccc} (\mathbf{x}, \mathbf{v}) & \Longrightarrow & (\rho, \ \mathbf{j}) \\ \Uparrow & \textit{cycle} & \Downarrow \\ \mathbf{F} & \Longleftarrow & (\mathbf{E}, \mathbf{B}) \end{array}$$

Figure 1.2. *The basic cycle of particle-in-cell (PIC) simulation code.*

At each time step, for the charge density and current density, some weighting schemes are needed to assign particle charge to neighboring grid points and to calculate the current density associated with the motion of particles. The choices of code characteristics, i.e., time step and grid length, depend upon the physical problem. These choices should both guarantee the needs of computational accuracy and stability and reduce computational cost. The time step Δt should be small enough to resolve the highest frequency in the problem. The choice of grid length should be fine enough to resolve Debye length $\lambda_{De} = v_{the}/\omega_{pe}$. For example, if we solve the plasma oscillation of electrons, then the following critical condition is required, because of typical length of the plasma oscillation is $\pi\lambda_{De}$.

$$\Delta x < \pi\lambda_{De} \tag{1.20}$$

Furthermore, to avoid non-physical results due to the finite difference approximation used to solve Newton-Lorentz and Maxwell's equations, the time step Δt and grid spacing Δx have to satisfy the following inequality, the so-called Courant-Friedrichs-Levy (CFL) condition.

For one-dimensional (1D) case, CFL condition is,

$$\Delta x > c\Delta t \tag{1.21}$$

For three-dimensional (3D) case, CFL condition is as follows:

$$(c\Delta t)^2(\frac{1}{\Delta x^2} + \frac{1}{\Delta y^2} + \frac{1}{\Delta z^2}) < 1 \tag{1.22}$$

Thus, the time step and the grid spacing should be chosen in such a way that the particles during one time step cannot cross a distance large that the size of the cell.

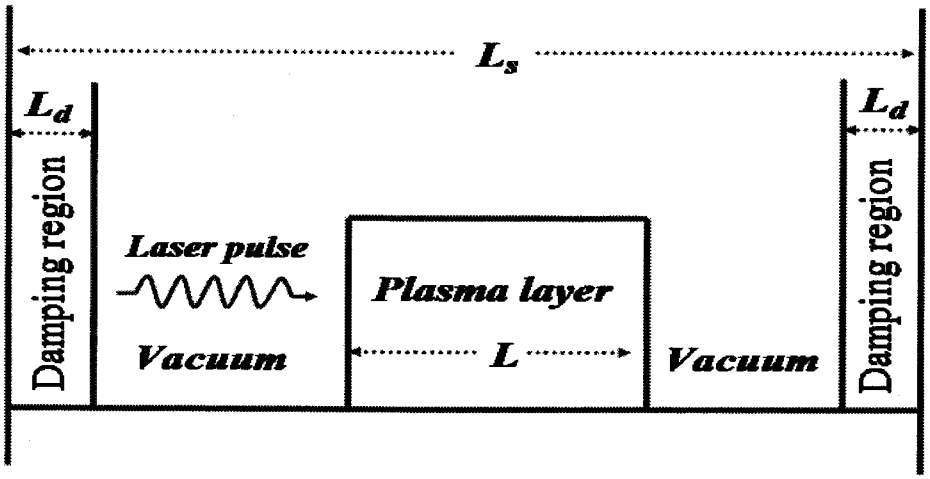

Sketch 1.1. The geometry of 1D3V PIC simulation.

In Sketch 1.1, the sketch of our 1D-PIC simulation is shown. The plasma layer is initially placed at the middle of the simulation system. When incident laser EM wave propagating in plasma, plasma particles which enter vacuum region build a potential both in the front and rear sides of plasma layer that prevents more particles of leaving the plasma layer. For these particles as well as for outgoing EM waves, two additional numerical damping regions are used at system ends.

If the length of the simulation system is taken as L_s and the additional damping regions used in both boundaries are taken as L_d, for both the particle momenta $\mathbf{p}(i)$ at position $\mathbf{x}(i)$ (i stands for the i^{th} particle) and the EM field $(\mathbf{E}, \mathbf{M})$ at position $\mathbf{X}$, the following damping conditions;

for left additional numerical damping region,

$$\mathbf{p}(i) = \frac{1}{2}\mathbf{p}(i)\left(1 + cos\frac{\pi(L_d - \mathbf{x}(i))}{L_d}\right) \tag{1.23}$$

$$\mathbf{E}(\mathbf{X}) = \frac{1}{2}\mathbf{E}(\mathbf{X})\left(1 + cos\frac{\pi(L_d - \mathbf{X})}{L_d}\right) \tag{1.24}$$

$$\mathbf{B}(\mathbf{X}) = \frac{1}{2}\mathbf{B}(\mathbf{X})\left(1 + cos\frac{\pi(L_d - \mathbf{X})}{L_d}\right) \tag{1.25}$$

for right additional numerical damping region,

$$\mathbf{p}(i) = \frac{1}{2}\mathbf{p}(i)\left(1 + cos\frac{\pi(\mathbf{x}(i) + L_d - L_s)}{L_d}\right) \tag{1.26}$$

$$\mathbf{E}(\mathbf{X}) = \frac{1}{2}\mathbf{E}(\mathbf{X})\left(1 + cos\frac{\pi(\mathbf{X} + L_d - L_s)}{L_d}\right) \tag{1.27}$$

$$\mathbf{B}(\mathbf{X}) = \frac{1}{2}\mathbf{B}(\mathbf{X})\left(1 + cos\frac{\pi(\mathbf{X} + L_d - L_s)}{L_d}\right) \tag{1.28}$$

are used in our 1D-PIC simulations, respectively.

Leap-frog method is implemented in our simulation to solve both Newton-Lorentz equation and Maxwell's equations.

Chapter 2

Accelerated large amplitude relativistic electromagnetic solitons

2.1 Stimulated Raman scattering and Raman cascade-into-condensation

When an intense laser propagates in an underdense plasma, a variety of instabilities can be excited by these resonant coupling processes of the incident laser EM wave with the scattered EM waves and the plasma ES waves. Among these instabilities, the stimulated Raman scattering (SRS) is the most important one. It can be simply characterized as the resonant decay of an incident laser EM wave (ω_0, k_0) into a scattered Stokes EM wave (ω_s, k_s) plus an electron plasma wave (EPW) (ω_{epw}, k_{epw}) (Langmuir wave). This process satisfy the following matching conditions for frequencies and wave numbers,

$$\omega_0 = \omega_s + \omega_{epw}, \quad k_0 = \pm k_s + k_{epw} \tag{2.1}$$

Here, + and − in $\pm k_s$ denote stimulated forward and backward Raman scattering (F-SRS/B-SRS), respectively.

An EM wave propagating in a plasma has dispersion relation $\omega_0^2 = \omega_{pe}^2 + k_0^2 c^2$, where c is the speed of light. Therefore, the minimum frequency for EM wave propagating inside plasma is the electron plasma frequency ω_{pe}, so it is clear that the SRS instability requires that

$$\omega_0 \geq 2\omega_{pe} \implies n \leq \gamma n_{cr}/4 \tag{2.2}$$

where n and n_{cr} are the plasma density and the critical density of laser pulse, γ is the relativistic Lorentz factor, respectively.

By SRS instability process, ω_s/ω_0 part of the incident laser energy is scattered and ω_{epw}/ω_0 part is deposited into the EPW. When EPW damps, this portion of the energy

heat the plasma. SRS instability is particularly significant concern because the EPW has a very high phase velocity of the order of the light velocity, it can produce very energetic electrons, such electrons can preheat the fuel in laser fusion applications.

In addition to the above wave triplet described (2.1) for SRS, usually, another weaker resonant three-wave coupling process with the first anti-Stokes scattered EM wave can be observed in experiment and simulation,

$$\omega_s = \omega_0 + \omega_{epw}, \quad \mathbf{k_s} = \mathbf{k_0} + \mathbf{k_{epw}}. \tag{2.3}$$

By this three-wave coupling, one can obtain an upshifted frequency by the electron plasma wave frequency ω_{epw}.

When these scattered EM waves, *including Stokes and anti-Stokes modes*, propagating in a plasma in the backward or forward directions, and their intensities exceed the corresponding thresholds of three-wave coupling processes, *like the incident laser EM wave*, they become new pumps and new instabilities, thereby, can be excited. Further, the new excited scattered EM waves excite new instabilities if the corresponding thresholds are still exceeded. Successively, a stimulated Raman cascade process with the following frequency and wave number matching conditions,

$$\omega_{s,j} = \omega_0 \pm j\omega_{epw} \;\; ; \;\; \pm k_{s,j} = k_0 \pm jk_{epw} \quad (j = \pm 1, \pm 2, \pm 3, ...) \tag{2.4}$$

then therefore takes place in intense laser-plasma interaction. The scattered EM waves include, not only the first-, second-, $\cdots$, high-order Stokes modes ($j = -1, -2, \cdots$), but also the first-, second-, $\cdots$, high-order anti-Stokes modes ($j = 1, 2, \cdots$), respectively.

When a relativistic laser propagates in an underdense plasma, B-SRS and F-SRS can develop, they do not appear isolated but are often interconnected. A nonlinear interplay between B-SRS and F-SRS produces a strong spatial modulation of the laser pulse and stimulated Raman cascade in its frequency spectra both for forward and backward scattered EM waves. The continuing instability growth through stimulated Raman cascade downshifts the power maximum from the fundamental to the bottom of the EM wave spectra. It gets saturated by the photon condensation mechanism, related to strong depletion and possible break-up of the laser beam. In the final stage of the cascade-into-condensation mechanism, the depleted downshifted laser pulse gradually transforms into a train of ultra-short relativistic EM solitons [18, 19].

In this chapter, we present and discuss the fully relativistic EM one-dimensional particle-in-cell (1D-PIC) simulation results on the SRS, the stimulated Raman cascade-into-condensation and the large amplitude relativistic EM solitons, induced by linearly-polarized intense laser interacting with underdense homogeneous plasma.

Our results clearly show the SRS process and can reveal the clear physics picture on stimulated Raman cascade and cascade-into-condensation processes. As a new result, we found that, in addition to the inhomogeneity of plasma density, the acceleration of large

amplitude relativistic EM soliton depends upon, not only the incident laser amplitude, but also upon the plasma length. The electric field inside the soliton region has the half-cycle structure in space, while the magnetic field and corresponding electrostatic (ES) field have the one-cycle structure in space. Only from the point of view of the frequency, during the soliton existence, it seems that this phenomenon can be explained roughly as a 3-wave resonant coupling process.

In order to study the wave characteristics and the growth of instabilities in laser-plasma interaction, as one of the most effective tools, it is very convenient to measure and analyze reflectivity (R) and transmissivity (T) of EM waves in vacuum regions.

$$R = \left|\frac{\langle S_r \rangle}{\langle S_i \rangle}\right| \quad ; \quad T = \left|\frac{\langle S_t \rangle}{\langle S_i \rangle}\right| \tag{2.5}$$

where the mark $\langle\rangle$ denotes time-averaged value. The S_i, S_r and S_t stand for the longitudinal components of the Poynting vector for incident EM wave, reflected EM wave and transmitted EM wave, respectively. They can be easily calculated from simulation data for EM fields as follows;

$$S_i = \frac{1}{\mu_0}(E_y B_z - E_z B_y) = S_r + S_t \tag{2.6}$$

where

$$S_r = -\frac{1}{4\mu_0 c}[(E_y - cB_z)^2 + (E_z + cB_y)^2]$$

$$S_t = \frac{1}{4\mu_0 c}[(E_y + cB_z)^2 + (E_z - cB_y)^2]$$

By analyzing the reflectivity (R) and transimissivity (T), one can get clear information to study and investigate the process of laser-plasma interaction.

2.1.1 Simulation model

One-dimensional fully relativistic EM particle-in-cell (1d3v-PIC) code is used (all quantities depend on x-coordinate and the particle momenta have three components). The geometry of simulation is shown in Sketch 2.1. The total length of simulation system is 2700 c/ω_0, where c and ω_0 are the speed of light and the laser EM frequency in vacuum, respectively. The plasma is 900 c/ω_0 long, it begins at x=0 and ends at $900c/\omega_0$. In the front and rear side of the plasma layer, there are two $900c/\omega_0$ long vacuum regions. The plasma density and temperature are $n = 0.032 n_{cr}$ and $T_e = 350eV$, where $n_{cr} = \omega_0^2 m_e / 4\pi e^2$ is the critical density for incident laser propagating in a plasma. Ions are initially placed as a neutralizing background and are kept immobile. The number of cells is 10 per 1 c/ω_0 and 80 particles are put in each cell. The incident laser is linearly-polarized with the electric field E_0 along the y-direction and the normalized amplitude

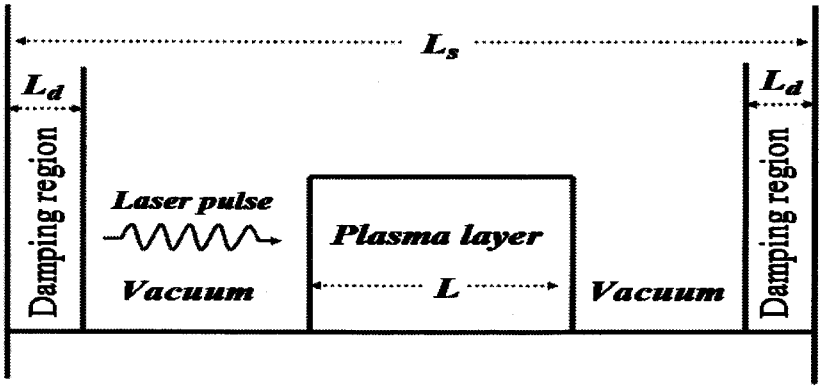

Sketch 2.1. The geometry of 1D3V PIC simulation.

$a = eE_0/m_e\omega_0 c$, it is launched at the left position where $500c/\omega_0$ long distance before plasma, where e and m_e are the electron mass and charge, respectively. By taking the EM field at the left position and the EM field at the right position both are $100c/\omega_0$ long distance away from plasma, the reflectivity and transmissivity are calculated, respectively. The electrons which enter vacuum region build a potential barrier that prevents electrons of leaving the plasma. For these electrons as well as for outgoing EM waves, two $100c/\omega_0$ long additional numerical damping regions are used at system ends.

It should be noted, in the following parts of this thesis, the time, electric field and magnetic field are normalized to the laser period $2\pi/\omega_0$, $m\omega_0 c/e$ and $m\omega_0/e$, respectively; the time is taken zero, $t = 0$, when the laser arrives at the left vacuum-plasma boundary.

2.1.2 Simulation results

The plasma is initially uniform in density and the intense laser pulse is radiated continuously in our simulations. There is enough time for the growth of instabilities and rich interplay between many relativistic electronic parametric instabilities, such as F-SRS, B-SRS and relativistic modulational instability (RMI) [18]. When an intense laser propagates in underdense plasma, SRS can be first excited by the intense laser EM wave coupling into a scattered EM wave plus an EPW. In such a low plasma density $n = 0.032n_{cr}$, B-SRS has shorter growth time than that of the F-SRS, it gets saturated efficiently at a very early stage of evolution due to plasma heating or particle trapping. However, with time goes on, F-SRS and RMI can get close and merge to unique F-SRS/RMI instability, after that, which can compete with the B-SRS instability.

For the processes dominated by B-SRS or F-SRS, they can be well-explained by three-wave resonant coupling decay with the corresponding matching conditions for frequency $\omega_0 = \omega_s + \omega_{epw}$ and for wave number $\mathbf{k}_0 = \mathbf{k}_s + \mathbf{k}_{epw}$. The dispersion relation for EM wave is $\omega_{0,s}^2 = \omega_{pe}^2 + k_{0,s}^2 c^2$ and for EPW is $\omega_{epw}^2 = \omega_{pe}^2 + 3k_{epw}^2 v_{the}^2$, respectively; where, the $v_{the} = (T_e/m_e)^{1/2}$ is electron thermal velocity.

In the case of laser amplitude $a = 0.3$, the frequency spectra and wave numbers for

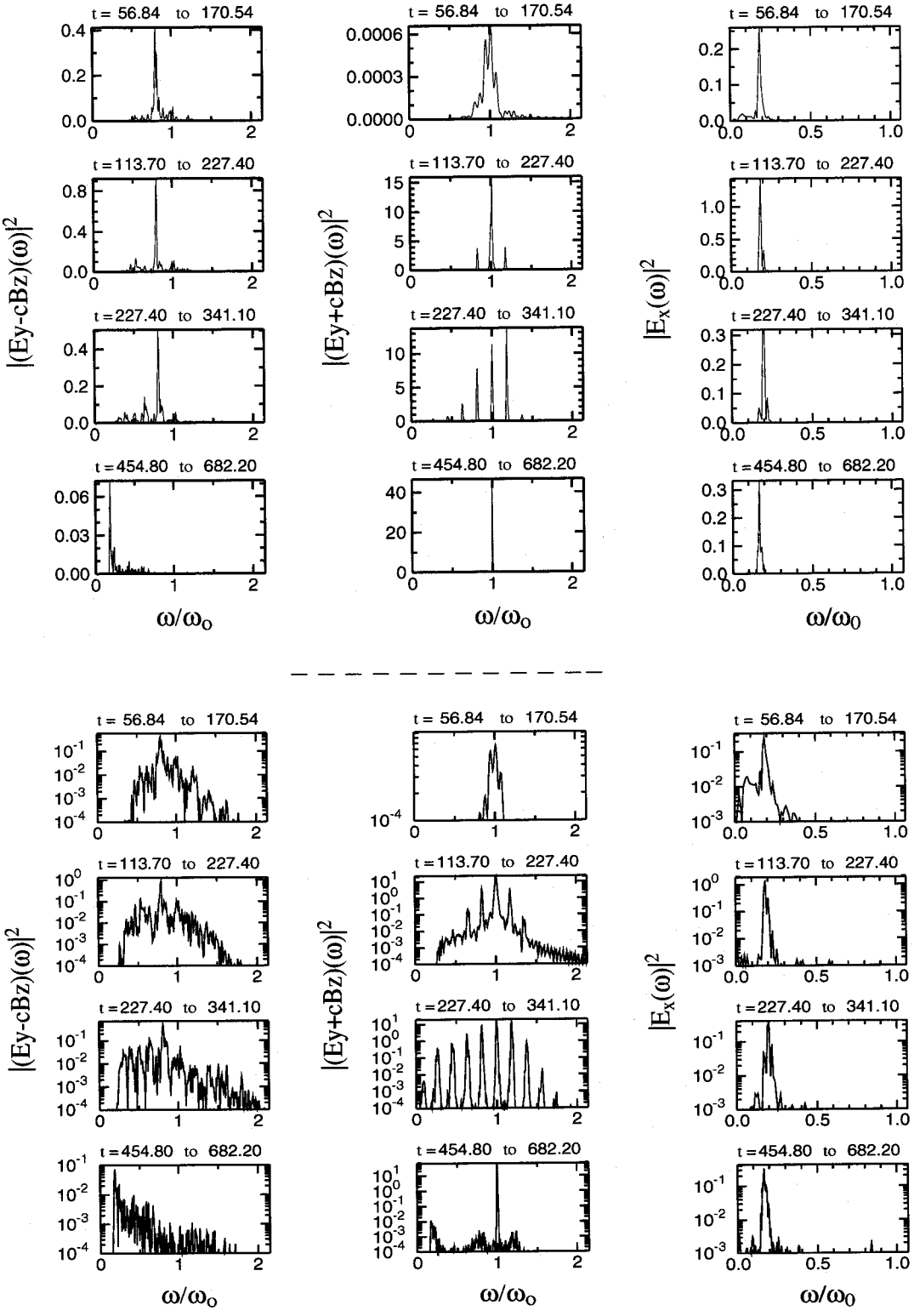

Figure 2.1: The frequency spectra for reflected and transmitted EM waves both measured in vacuum regions, and the spectrum for ES wave measured inside plasma in the case of plasma $n = 0.032n_{cr}$, $L = 900c/\omega_0$ and laser amplitude $a = 0.3$. The corresponding logarithmic plots are shown in the bottom figures.

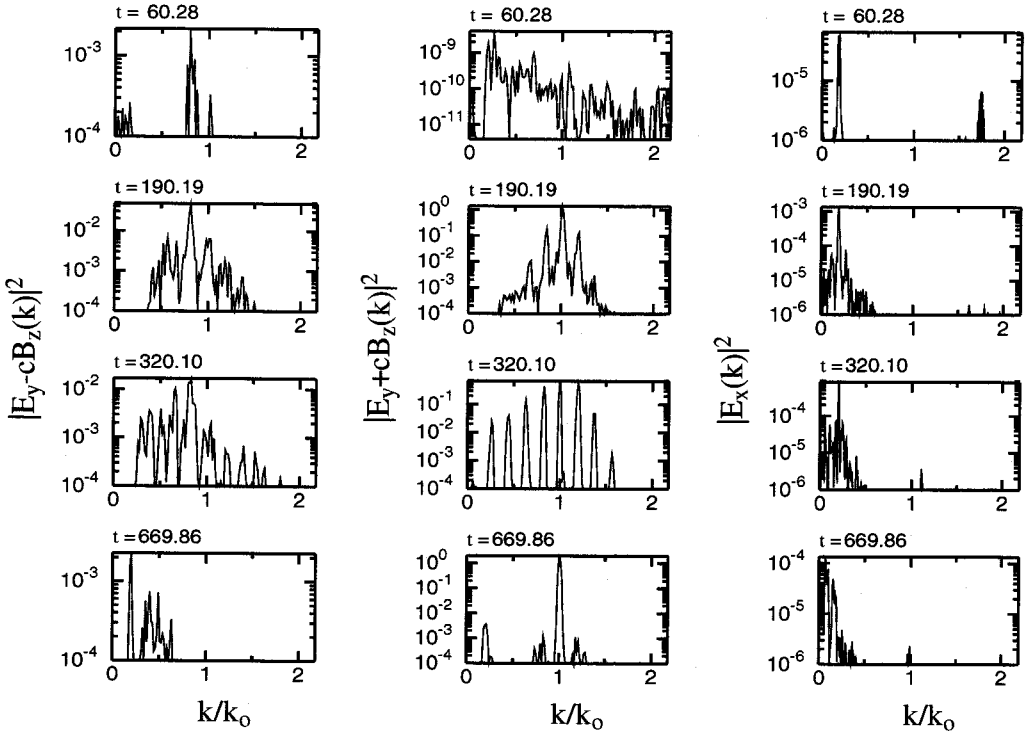

Figure 2.2: The wave number plots for reflected and transmitted EM wave both measured in vacuum regions, and for ES wave measured inside plasma in the case of plasma $n = 0.032n_{cr}$, $L = 900c/\omega_0$ and laser amplitude $a = 0.3$, respectively.

reflected EM wave and transmitted EM wave both measured in vacuums, and ES wave measured inside plasma are plotted in figure 2.1 and figure 2.2. During SRS process, the excited dominant ES wave is EPW with frequency $\omega_{pe} \approx 0.18\omega_0$; the corresponding scattered Stokes wave has its frequency $\omega_s \approx 0.82\omega_0$. The corresponding wave numbers for both backward and forward scattered EM waves are $k_s \approx 0.82k_0$; the EPW have two dominant peaks, the first peak with $k_{epw} \approx 1.82k_0$ for B-SRS and the second peak with $k_{epw} \approx 0.18k_0$ for F-SRS, respectively.

Figure 2.3 shows the snapshots for the energy density of EM field. It demonstrates the spatial distribution of transverse EM wave energy density. B-SRS has shorter growth time than F-SRS, it gets saturated efficiently at a very early stage of evolution. From figure 2.3 (top), one can see, in its early stage, B-SRS radiates its EM energy through soliton-like structures, which corresponds to the peaks in the reflectivity plot of EM wave as shown in figure 2.4. As has been stated before, with time goes on, F-SRS and RMI can get close and merge to unique F-SRS/RMI instability, which can compete with the B-SRS instability. As a result, the strong spatial self-modulation of the order of $\lambda_{pe} = 2\pi c/\omega_{pe} \approx 5\lambda_0$ which comes from F-SRS/RMI instability and the depletion of the laser pulse are taken place and observed from figure 2.3.

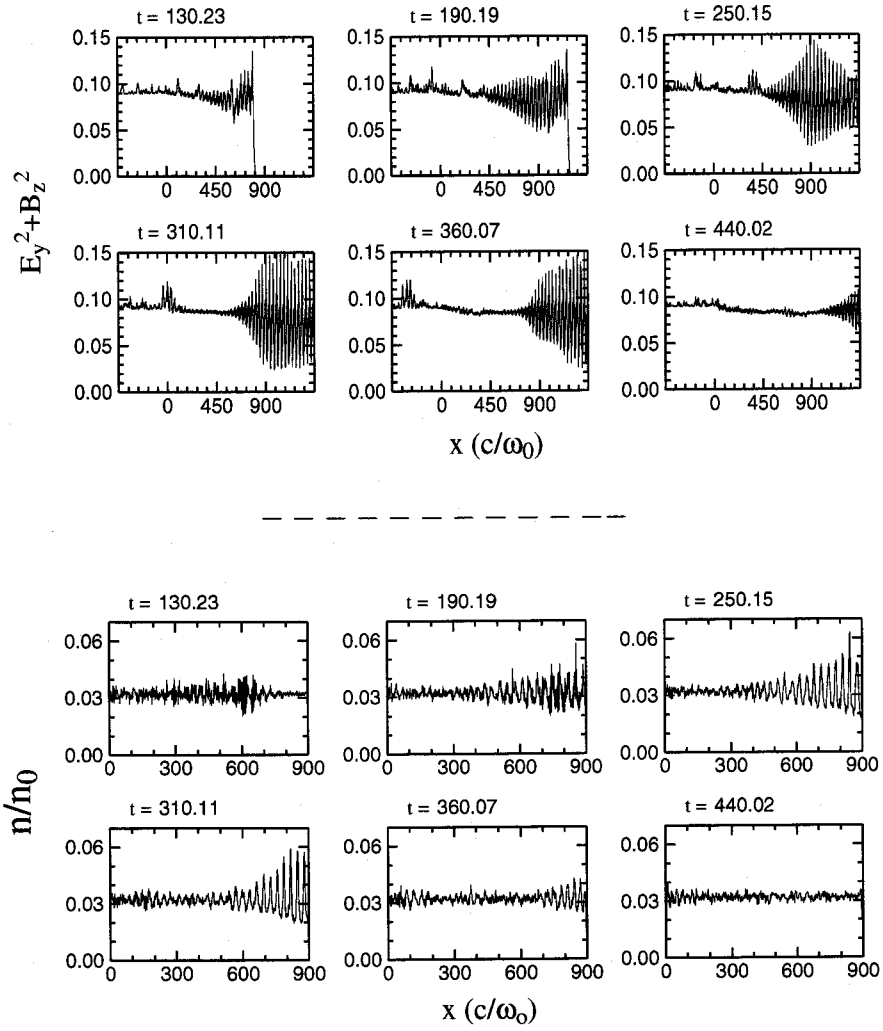

Figure 2.3: The snapshots for energy density of EM field $E_y^2 + B_z^2$ averaged over the laser period (top) and electron density (bottom) in the case of plasma $n = 0.032n_{cr}$, $L = 900c/\omega_0$ and laser amplitude $a = 0.3$, respectively.

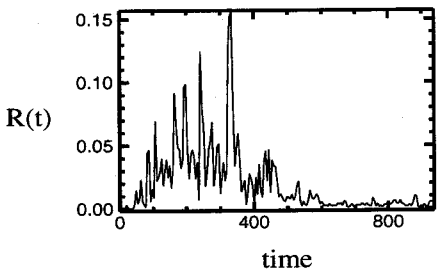

Figure 2.4: The reflectivity of EM wave measured in vacuum region in the case of plasma $n = 0.032n_{cr}$, $L = 900c/\omega_0$ and laser amplitude $a = 0.3$, respectively.

B-SRS and F-SRS with the Stokes wave components in frequency spectra are far dominant over the anti-Stokes components in a linear regime. There is a clear stimulated forward Raman cascade process as shown clearly in figure 2.1 and figure 2.2 for the frequency spectra and wave numbers for transmitted EM wave. The scattered Stokes EM waves include the first-, second-, third- and fourth-Stokes modes with their corresponding frequencies and wave numbers $(0.82\omega_0, 0.82k_0)$, $(0.64\omega_0, 0.64k_0)$, $(0.46\omega_0, 0.46k_0)$ and $(0.28\omega_0, 0.28k_0)$, respectively. In addition to Stokes modes, the first anti-Stokes mode with $(1.18\omega_0, 1.18k_0)$ can be also observed, from the logarithmic plots for transmitted EM wave, one even can observe the second anti-Stokes mode $(1.36\omega_0, 1.36k_0)$, the third anti-Stokes mode $(1.54\omega_0, 1.54k_0)$ and the fourth anti-Stokes mode $(1.72\omega_0, 1.72k_0)$. Both for Stokes and anti-Stokes modes, from the lower-order to higher-order mode, the intensity of scattered EM wave become weaker and weaker. The stimulated forward Raman cascade is eventually halted near the electron plasma frequency $0.18\omega_0$. It should be noted here, sometimes, the stimulated forward Raman cascade is dominated by the first anti-Stokes mode with its power peaks for frequency and wave number even larger than that of the laser mode. From frequency spectra and wave numbers of backscattered EM wave, stimulated backward Raman cascade still can be observed, which include both Stokes and anti-Stokes EM modes, however, it does not reveal a clear Raman cascade process as shown in stimulated forward Raman cascade process. The another interesting feature is that, there is the broadening of the backscattered EM spectra, from laser frequency to electron plasma frequency. In the meantime, the reflectivity exhibits a spiky behavior, as shown in figure 2.4, which is a result of condensation and modulational instability generating spiky turbulence [18].

In the later time, for both forward and backward EM wave spectra, one can find that continuing instability growth through stimulated Raman cascade downshifts a power maximum from the fundamental to the bottom of the EM wave spectra. They clearly reveal a tendency of a transition from the Raman cascade regime to the regime of energy accumulation at about the electron plasma frequency which is the cutoff frequency for EM wave propagating in a plasma, the so-called photon condensation. The cascade-into-condensation transition becomes more pronounced with increasing laser intensity or increasing electron plasma density [18].

By above processes, a large amplitude EPW can be excited. Large part of the incident laser energy is deposited into EPW. The excited EPW has a very high phase velocity of the order of the light velocity. When the EPW damps, its energy can heat bulk plasma and also produce very energetic electrons. *In figure 2.5, the electron phase-space $x - p_x$ snapshots and electron energy distribution $f(\gamma)$ snapshots are plotted.* We can see that, with the laser EM wave penetrating into and propagating in the plasma, first an EPW will be excited, and then, it grows and saturates with time. After these process, due to its breaking, electrons are trapped and accelerated to high momentum or energy by

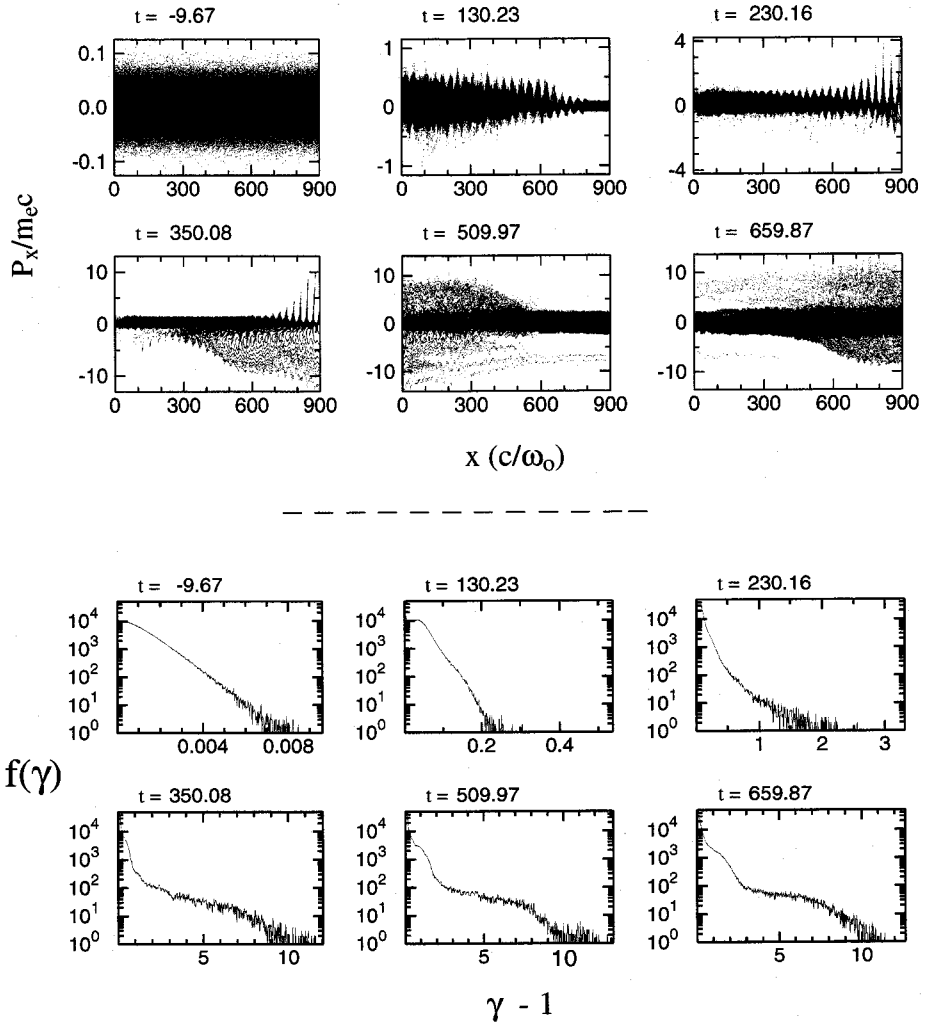

Figure 2.5: The snapshots for electron phase-space $x - p_x$ (top) and the snapshots for energy distribution $f(\gamma) - \gamma$ (bottom) from 1D-PIC simulation in the case of plasma $n = 0.032 n_{cr}$, $L = 900c/\omega_0$ and laser amplitude $a = 0.3$, respectively.

obtaining energy from EPW. From the data of the figure 2.5, one can get the maximum electron momentum and energy of $p_e^{max}/m_e c \approx 15$ and $E_e^{max} \approx 8MeV$, respectively.

2.2 Large amplitude relativistic EM soliton

When an intense laser propagates in a underdense plasma, first, dispersion effects play an important role because plasma particle masses relativistically increase by their responding to the intense laser EM field; second, the nonlinearity appears due to the plasma density redistribution under the action of the ponderomotive force of intense laser EM field, which pushes the plasma particles away from the region of the maximum

EM field [43]. Therefore, in addition to the various instabilities, these effects can lead to well-known nonlinear phenomena, such as, relativistic self-focusing [44, 45], relativistic transparency of an overdense plasma [50, 51], and the generation of relativistic EM soliton [52, 53]. Diverse nonlinear phenomena enrich the process of the laser-plasma interaction and therefore make it more complicated.

It is reported that, in a homogeneous plasma condition, solitons have been found to exist for a long time, close to the regions where they were generated; while, in inhomogeneous plasmas, solitons are accelerated with the acceleration proportional to the gradient of the plasma density towards the low density side. When a soliton reaches some critical plasma region, for example, the plasma-vacuum interface, it radiates away its energy in the form of a short burst of low-frequency EM radiation [62, 74].

Recently, we have put some attention into the research on the relativistic EM solitons. As a new point on the acceleration of soliton, we found that, in addition to the inhomogeneity of plasma density, the acceleration of relativistic EM solitons can depend upon, not only the incident laser amplitude, but also upon the plasma length [75].

In following sections, we will concentrate on the large amplitude relativistic EM solitons, which are generated after SRS and Raman cascade-into-condensation processes.

2.2.1 Large amplitude standing relativistic EM soliton

For the laser amplitude $a = 0.3$ case, the first stage is dominated by the SRS interactions which evolve into a complex nonlinear dynamical phenomenon. Parametric down-cascade of the laser pulse into the higher-order SRS harmonics saturates into the Photon Condensate at the bottom of the light spectrum, followed by strong electron heating. As the time goes on, as in figure 2.6 for the electron density n/n_0 and the energy density of EM field $E_y^2 + B_z^2$ snapshots; a spatially localized, non-propagating inside plasma, a spatially localized, non-propagating electron density cavity is created. Inside the density cavity, an EM field is trapped and oscillates coherently, that is, a large amplitude localized standing relativistic EM soliton forms.

In figure 2.7 (top), the frequency spectra $|E_y(\omega)|^2$ for EM wave and $|E_x(\omega)|^2$ for ES wave which trapped inside the soliton are plotted. In addition to the laser fundamental and the excited perturbed EPW, the EM component with the frequency close to $0.13\omega_0$ and the ES component with the frequency near to $0.87\omega_0$ are observed. Only from the point of view of the frequency, it seems that, one can explain this phenomenon roughly by a 3-wave resonant coupling process during the existence of EM soliton. The size of the soliton is about $5\lambda_0$ (λ_0 is laser wavelength in vacuum), close to the electron plasma wavelength $\lambda_{epw} = 2\pi c/\omega_{epw}$. Figure 2.7 (bottom) shows the structures of the EM and ES fields inside plasma, we can see that, the ES field E_x which trapped inside soliton has one-cycle structure, the corresponding transverse electric field E_y is the half-cycle

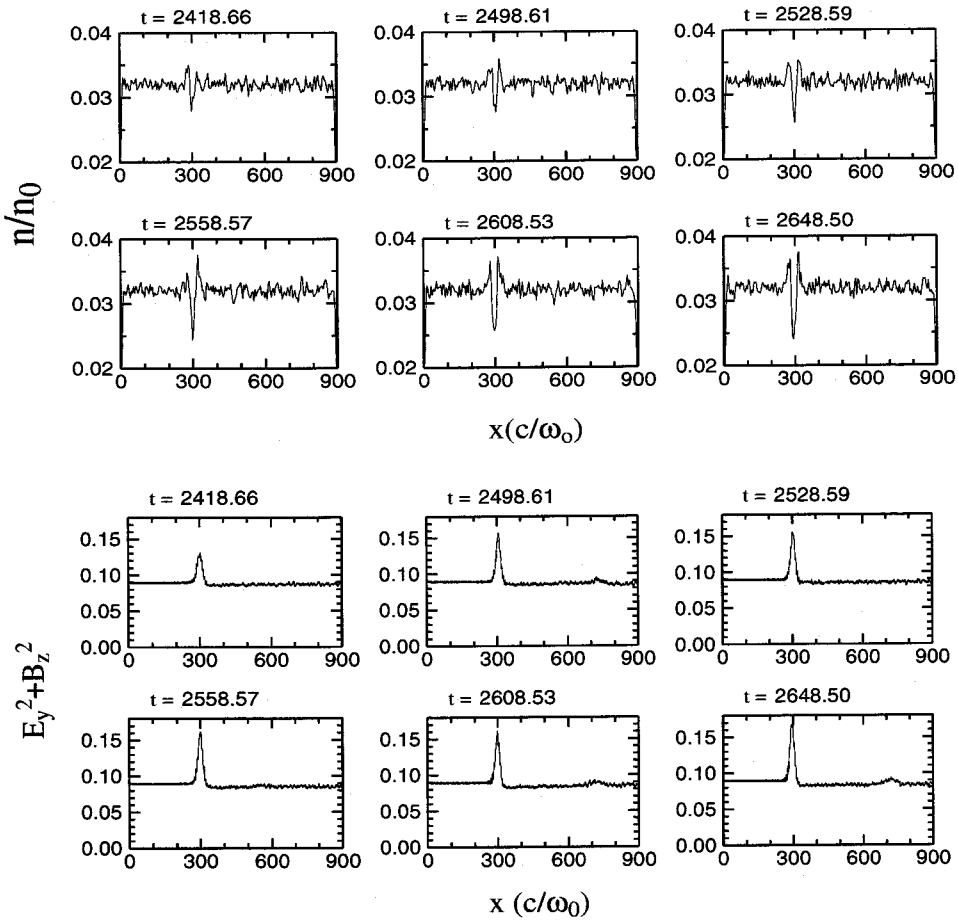

Figure 2.6: The snapshots for electron density n_e/n_0 (top) and for energy density of EM field $E_y^2 + B_z^2$ averaged over the laser period (bottom) in the case of plasma length $n = 0.032n_{cr}$, $L = 900c/\omega_0$ and laser amplitude $a = 0.3$, respectively.

structure and the magnetic field B_z is the one-cycle structure in space, respectively. And the spatial EM field structure is oscillatory in time, while the ES field structure is not. The explanation comes directly from Maxwell's equations. The Faraday law gives $B_z \sim \partial E_y/\partial x$; indeed, the x-derivative of the Gaussian soliton profile E_y gives B_z in figure 2.7. Similarly, from the Poisson equation, integration over x of the Gaussian density cavity (figure 2.6) leads to the ES field E_x in figure 2.7. Moreover, PIC data and analytics, e.g., equations (4-7) of [58], show that zero-harmonic term dominates the electron density perturbation (ponderomotive term). Therefore, the Poisson equation gives the corresponding non-oscillatory ES field structure, like E_x in figure 2.7.

It should be stated that the the frequency of EM component inside soliton $0.13\omega_0$ is smaller than the unperturbed electron plasma frequency $\omega_{pe} \sim 0.18\omega_0$. Electron acceleration causes relativistic electron effective mass increase from m_e to γm_e. This, thereby, reduces the electron plasma frequency from ω_{pe} to $\omega_{pe}/\gamma^{1/2}$. Therefore, the EM

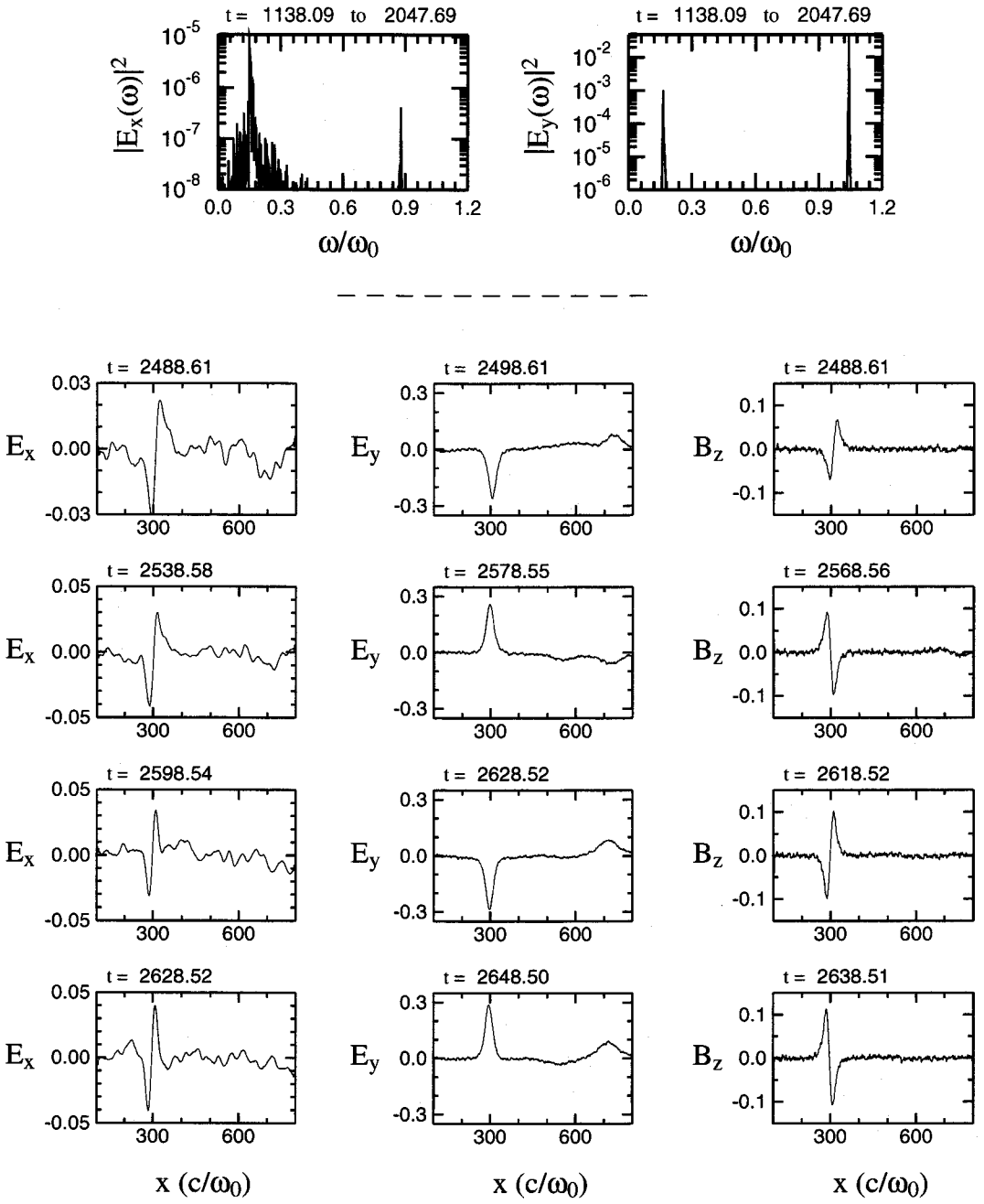

Figure 2.7: The frequency spectra of EM field and ES field inside soliton region (top); and the snapshots for EM field structure (averaged over the laser wavelength λ_0) and ES field structure (averaged over the EPW wavelength λ_{epw}) in the case of plasma $n = 0.032n_{cr}$, $L = 900c/\omega_0$ and laser amplitude $a = 0.3$, respectively.

waves, which have frequencies smaller than the unperturbed electron plasma frequency ω_{pe}, can exist and propagate inside plasma.

This large amplitude relativistic EM soliton is a standing one. After its formation, it exists within our simulation time, close to the regions where it was generated. It can be explained by [62, 74], namely, the acceleration of EM soliton depends upon the inhomogeneity of plasma density and in the case of homogeneous plasma, the EM soliton belongs to the standing one.

From the characteristics of the relativistic EM soliton what we stated before and will show in the following parts in this chapter, they are similar to that of the results in the Ref. [58]. In Ref. [58], *Lj. Hadžievshi, M.S. Jovanović, M.M. Škorić and K. Mima,* by considering a weakly relativistic limit, cold plasma condition and neglecting ion dynamics, they obtained an nonlinear Schrödinger equation with two nonlocal (derivative) nonlinear terms [58]. By using this nonlinear Schrödinger equation, the existence and stability of 1D EM solitons formed in a relativistic interaction of a linearly polarized laser light with an underdense cold plasma are discussed, and the standing EM soliton solutions with maximum amplitude $\mathbf{A}_s \approx 2.7$ and frequency $\omega_s \approx 0.73\omega_0$ are analytically shown to be stable in agreement with the model simulation.

From this point of view, perhaps, we can subsume our large amplitude relativistic EM solitons in the class of the "nonlinear Schrödinger soliton", at least, they belong to the type of "nonlinear Schrödinger soliton-like".

However, if we keep all the simulation parameters as used before in the case of laser amplitude $a = 0.3$, only by increasing laser amplitude, from the new simulations, we found that, the scenarios about the acceleration of soliton appears different from the standing case, not only the backward-accelerated EM solitons but also the forward-accelerated EM solitons are observed in our simulations.

2.2.2 Large amplitude backward-accelerated EM soliton

By increasing the laser amplitude to $a = 0.4$ and $a = 0.5$, the soliton dynamics appear different to that for a weak pump, e.g. $a = 0.3$, which is the standing soliton case. In two higher amplitude cases, observed large localized solitons are accelerated in backward direction towards the plasma-vacuum interface.

As shown in figure 2.8 for the electron plasma density n/n_0 and the energy density of EM field $E_y^2 + B_z^2$ snapshots for the laser amplitude $a = 0.4$ case; the soliton dynamics appears different to that in the standing soliton, i.e., laser amplitude $a = 0.3$ case. The observed large amplitude localized relativistic EM soliton is accelerated in the backward direction towards the plasma-vacuum interface. As the EM soliton approaches the plasma-vacuum interface it starts to radiate its energy away in the form of low-frequency intense EM burst, due to a non-adiabatic interaction with the plasma-vacuum boundary.

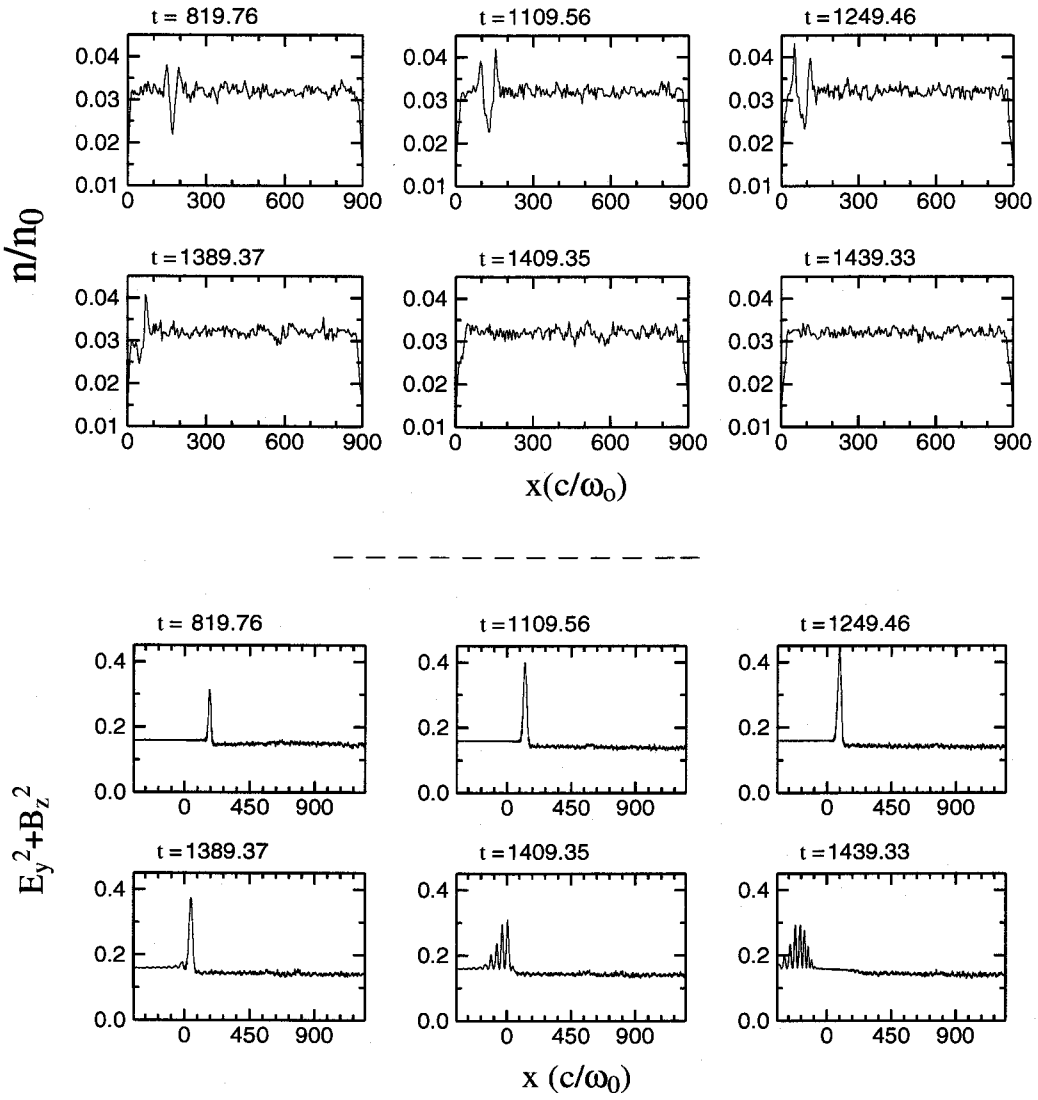

Figure 2.8: The snapshots for electron density n_e/n_0 (top) and for energy density of EM field $E_y^2 + B_z^2$ averaged over the laser period (bottom) in the case of plasma $n = 0.032 n_{cr}$, $L = 900c/\omega_0$ and laser amplitude $a = 0.4$, respectively.

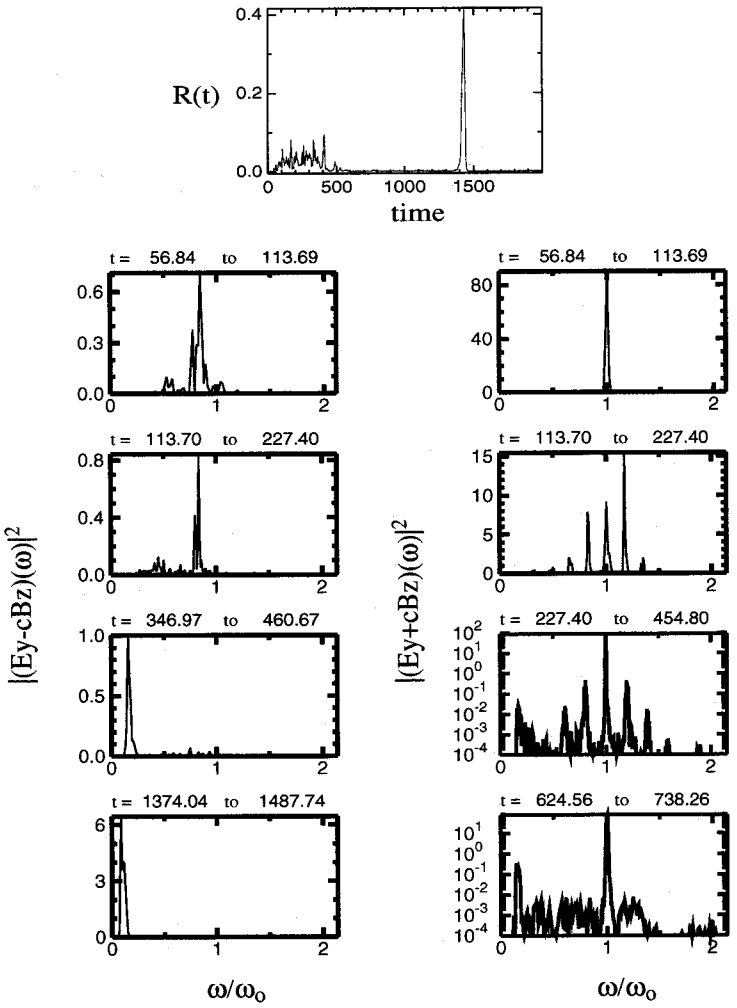

Figure 2.9: The reflectivity plot for EM wave (top) and the spectra for reflected EM wave and transmitted EM wave measured in vacuum regions (bottom) in the case of plasma $n = 0.032n_{cr}$, $L = 900c/\omega_0$ and laser amplitude $a = 0.4$, respectively.

As a result, one can observes a very high transient reflectivity, much larger than in the SRS backscattering process.

In figure 2.9, the reflectivity of EM wave and frequency spectra both for backward and forward EM waves are shown. After its radiation, by analyzing the frequency spectra of the backward-scattered EM wave in the vacuum regions, we found that, *see the last plot " $t = 1374.04$ to 1487.74" in figure 2.9*, the EM soliton has its EM frequency in vacuum regions is nearly $0.5\omega_{pe}$, i.e., about half of the electron plasma frequency. As we have stated before, because of strong relativistic effect, it is possible that a relativistic EM soliton with its EM frequency smaller than unperturbed electron plasma frequency ω_{pe} to form and propagate inside plasma; and after this backward-accelerated EM soliton arrives at the plasma-vacuum interface and there it radiates its energy away in the form

of intense EM burst, one can obtain the EM frequency of soliton which smaller than unperturbed electron plasma frequency ω_{pe} in vacuum regions.

Before the formation of the EM soliton, as have been shown in the laser amplitude $a = 0.3$ case, from figure 2.9, we also can observe the SRS process, which then evolves into stimulated Raman cascade and cascade-into-condensation. Parametric down-cascade of the laser pulse into the higher-order SRS harmonics (backward and forward) saturates into the photon condensation at the bottom of the light spectrum, followed by strong electron heating. However, in the case of laser amplitude $a = 0.4$, high laser intensity make all above processes more shorter than that in the case of laser amplitude $a = 0.3$, although we can still discern the peaks in the positions of Stokes and anti-Stokes modes, it is difficult to get clear spectra for both frequency and wave number as shown in the laser amplitude $a = 0.3$ case. A fact can be obtained that, with increasing laser amplitude, the Raman cascade-into-condensation transition becomes more pronounced; this phenomenon can be seen clearly from the frequency spectra of reflected and transmitted EM waves, there, one clear frequency peak can be observed nearly $0.5\omega_{pe}$.

In the higher laser amplitude $a = 0.5$ case, as shown in figure 2.10, the story is the same as for the laser amplitude $a = 0.4$ case; a backward-accelerated large amplitude relativistic EM soliton begins to form, followed that SRS, Raman cascade-into-condensation and electron acceleration. However, due to the larger acceleration, the "lifetime" of EM soliton in a plasma is shorter than that in laser amplitude $a = 0.4$ case. This result can be seen directly from figure 2.11, the plot for the EM soliton position $x(t)$ for laser amplitude $a = 0.4$ and 0.5 cases. Actually, in the unit normalized with the appropriate soliton (low-) frequency, the soliton amplitude greatly exceeds the laser pump (more than ω_0/ω_p times) and corresponds to a type of ultra-relativistic EM solitons [18, 58]. Similar to that laser amplitude $a = 0.4$ case, after this backward-accelerated EM soliton arrives at the plasma-vacuum interface, where radiating its energy away in the form of intense EM burst, as a result, a very high transient reflectivity larger than that in B-SRS, can be observed during its radiation. We also can obtain the EM frequency of soliton is about $0.5\omega_{pe}$ in vacuum regions. However, for laser amplitude $a = 0.5$ case, as shown in figure 2.12, the transition from Raman cascade to photon condensation becomes more pronounced than that in the case of laser amplitude $a = 0.4$; clear peaks around $0.5\omega_{pe}$ in frequency spectra for both the reflected and the transmitted EM waves.

In the backward-accelerated EM soliton cases, the EM and ES field structures inside soliton are the same as that of the standing soliton, i.e., in the case of laser amplitude $a = 0.3$. As shown in figure 2.13, both for laser amplitude $a = 0.4$ (top) and $a = 0.5$ (bottom), respectively, the ES field E_x trapped inside soliton has one-cycle structure, and the corresponding transverse electric field E_y is the half-cycle and the magnetic field B_z is the one-cycle structure, respectively. And the spatial EM field structure is oscillatory in time, but the ES field structure is not. The size of the soliton is about $5\lambda_0$,

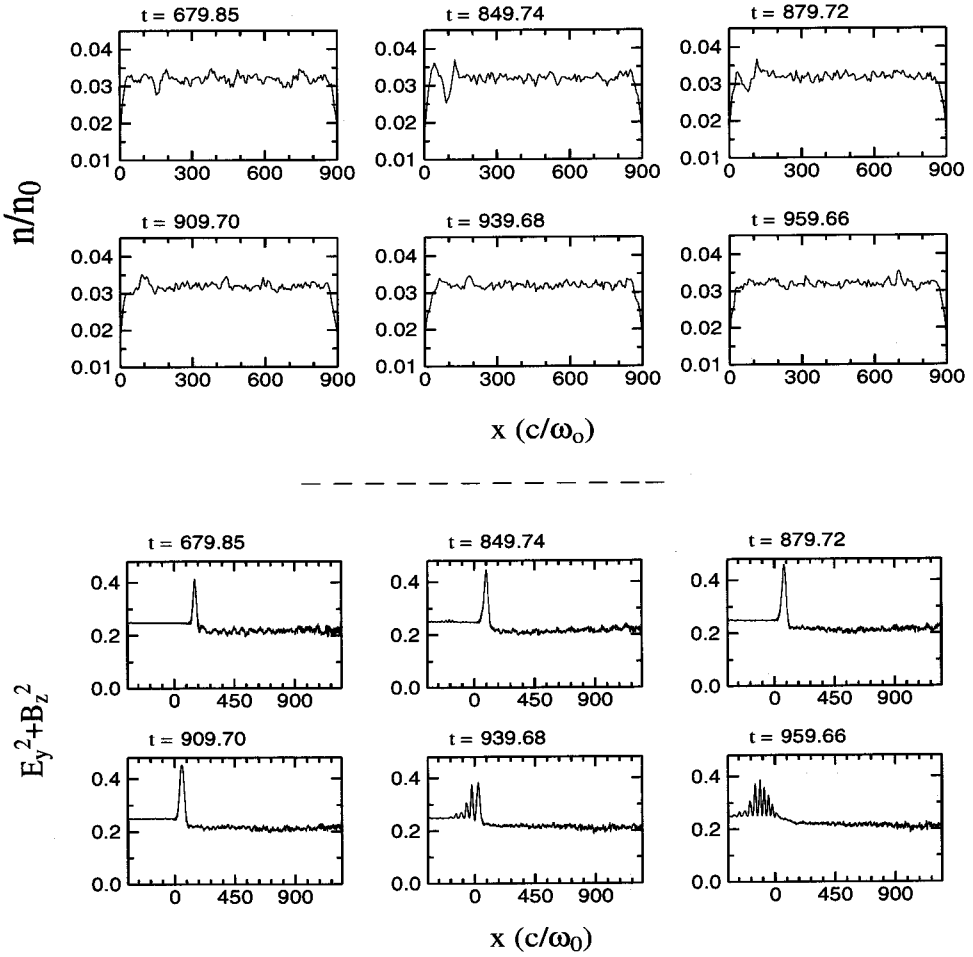

Figure 2.10: The snapshots for electron density n_e/n_0 (top) and for energy density of EM field $E_y^2 + B_z^2$ averaged over the laser period (bottom) in the case of plasma $n = 0.032 n_{cr}$, $L = 900c/\omega_0$ and laser amplitude $a = 0.5$, respectively.

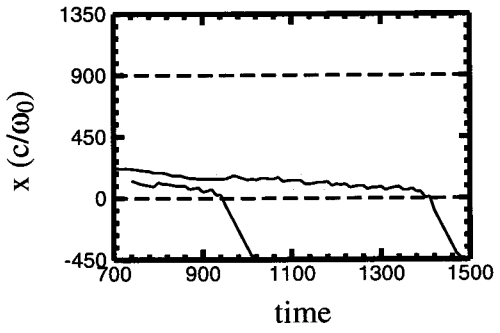

Figure 2.11: The plots for soliton orbits, red line for the case of laser amplitude $a = 0.4$ and blue line for the case of laser amplitude $a = 0.5$, respectively.

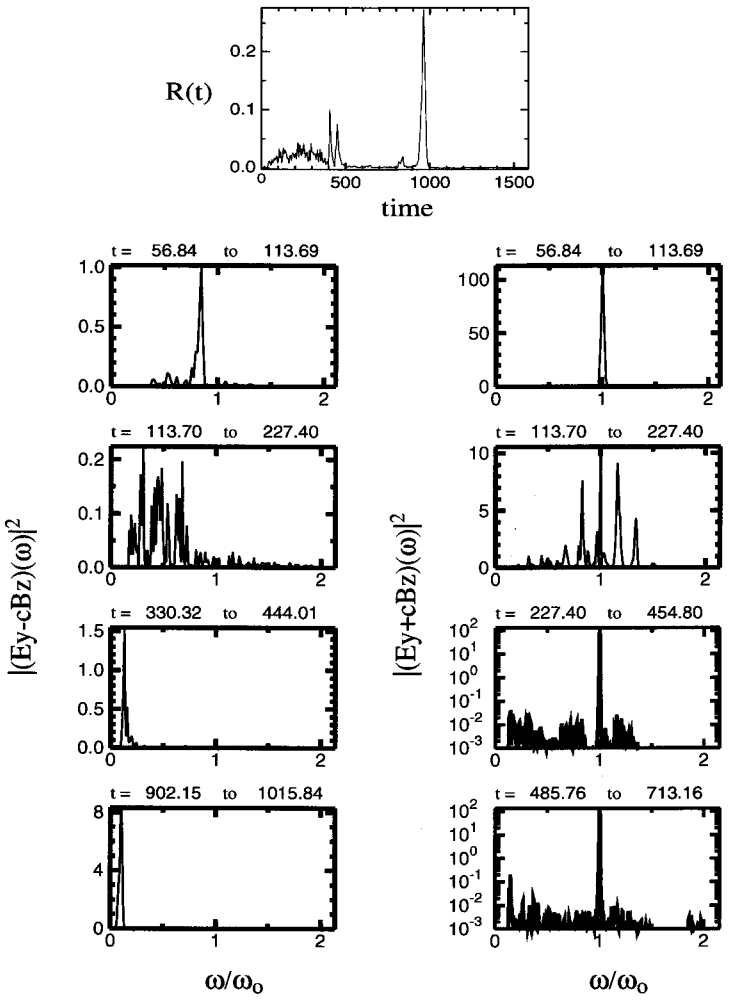

Figure 2.12: The reflectivity plot for EM wave (top) and the spectra for reflected EM wave and transmitted EM wave measured in vacuum regions (bottom) in the case of plasma $n = 0.032n_{cr}$, $L = 900c/\omega_0$ and laser amplitude $a = 0.5$, respectively.

close to the electron plasma wavelength λ_{epw}. It is difficult to analyze the ES frequency spectra of the solitons due to their acceleration inside plasma. However, the frequency spectra for ES field by taking the ES field at the position, where is close to the soliton region during our analyzing time inside plasma, are still given in figure 2.14. In the two cases, one can find the peaks with ES frequencies are about $0.85 \sim 0.9\omega_0$, together with their EM frequencies $0.5\omega_{pe} \approx 0.1\omega_0$ what detected in vacuum regions, it seems that, we can still explain this phenomenon roughly by a 3-wave resonant coupling process.

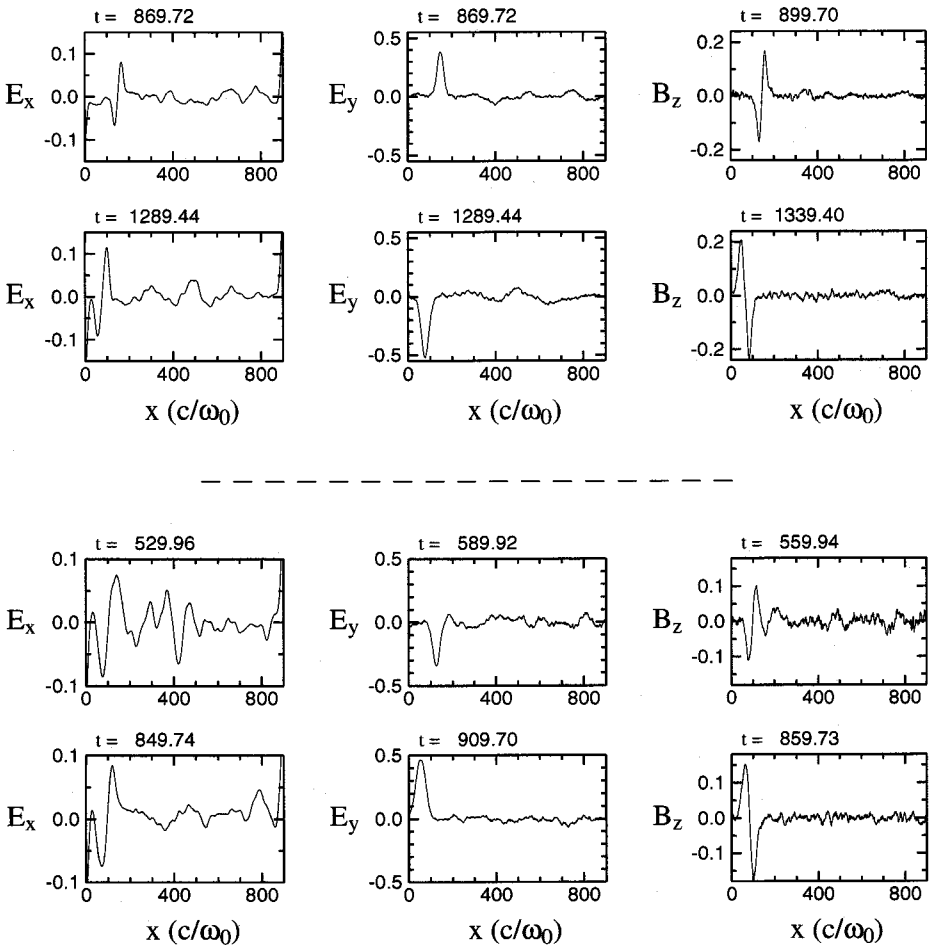

Figure 2.13: The snapshots for EM field structure averaged over laser wavelength λ_0 and the snapshots for ES field structure averaged over EPW wavelength λ_{epw}. The **top plots** for laser amplitude $a = 0.4$ case and **the bottom plots** for laser amplitude $a = 0.5$ case, respectively.

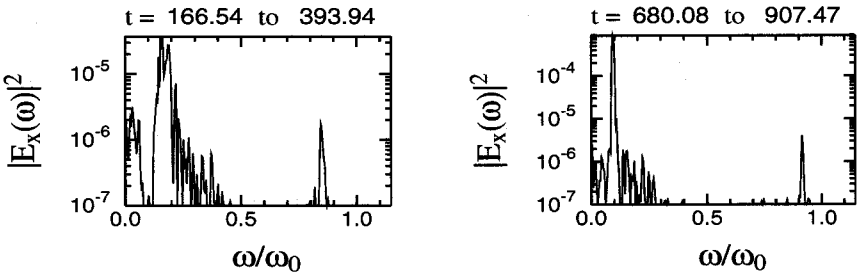

Figure 2.14: The frequency spectra of ES wave measured inside plasma. The **left plot** for laser amplitude $a = 0.4$ case and the **right plot** for laser amplitude $a = 0.5$ case, respectively.

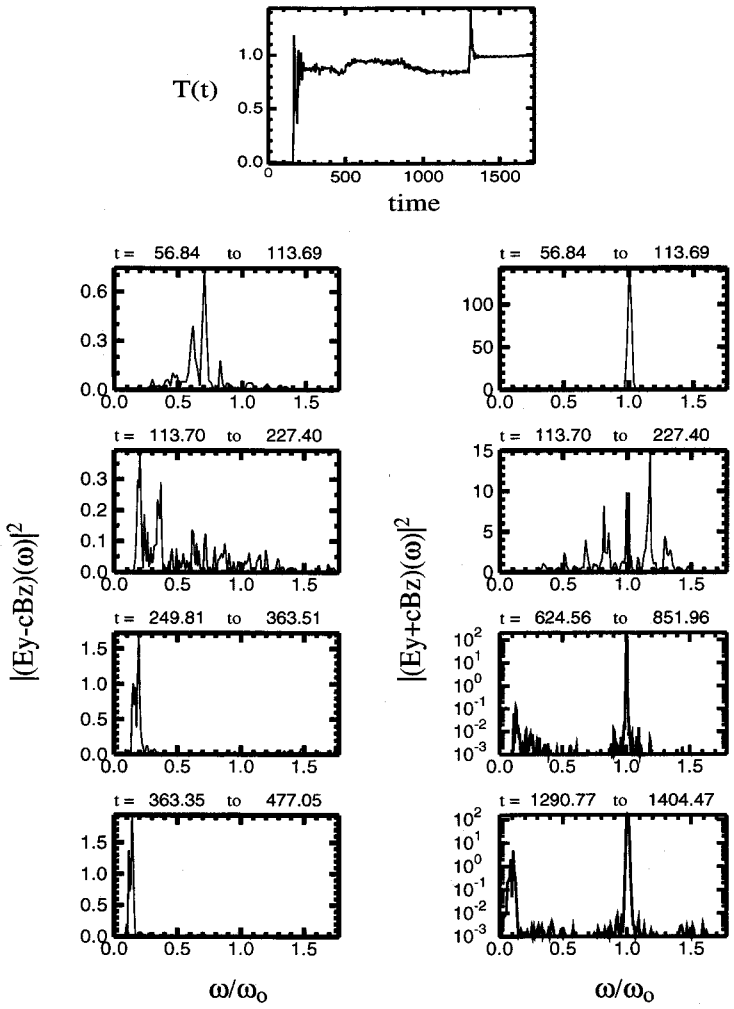

Figure 2.15: The transmissivity of EM wave (top) and the spectra for reflected EM wave and transmitted EM wave measured in vacuum regions (bottom), in case of plasma $n = 0.032n_{cr}$, $L = 900c/\omega_0$ and laser amplitude $a = 0.6$, respectively.

2.2.3 Large amplitude forward-accelerated EM soliton

If we still keep the same simulation parameters as used in the laser amplitude $a = 0.3$ case and continue to increase the laser amplitude to $a = 0.6$ and $a = 0.7$, the most interesting phenomenon is that, in the two cases, the observed large amplitude relativistic EM solitons are neither the standing ones nor the backward-accelerated ones, the large amplitude relativistic EM solitons are accelerated forward.

The stories before the formation of EM solitons are the same as the above cases. As the transmissivity and frequency spectra plots in figure 2.15 for laser amplitude $a = 0.6$ case and in figure 2.16 for laser amplitude $a = 0.7$ case shown us, followed that SRS, Raman cascade-into-condensation and electron acceleration, the forward-accelerated large

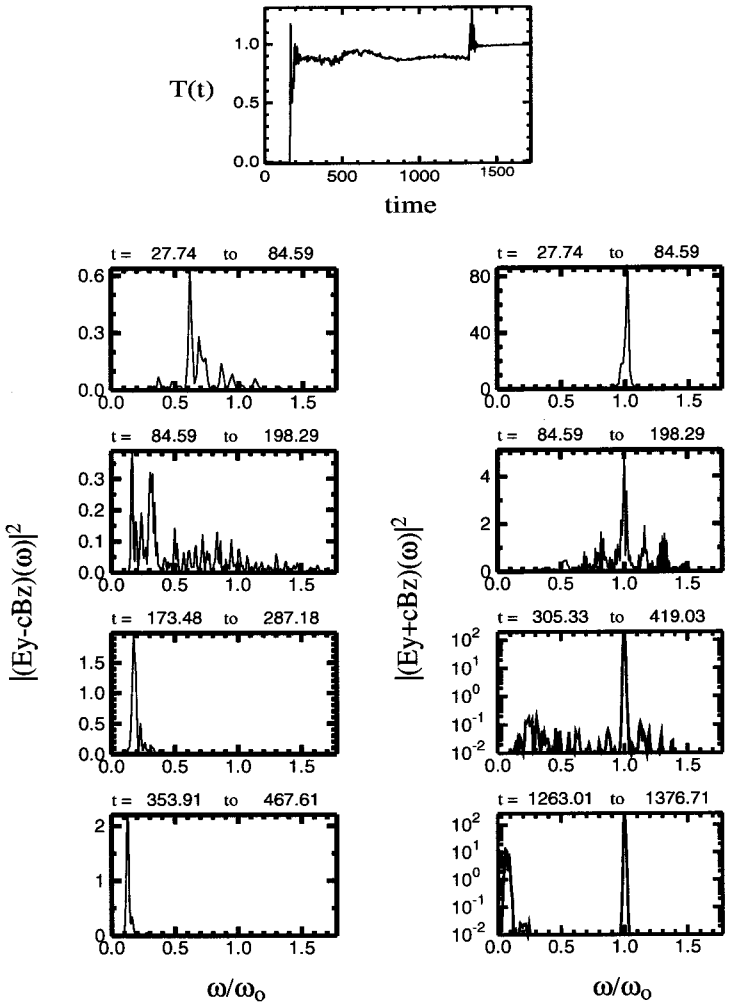

Figure 2.16: The transmissivity of EM wave (top) and the spectra for reflected EM wave and transmitted EM wave measured in vacuum regions (bottom), in case of plasma $n = 0.032n_{cr}$, $L = 900c/\omega_0$ and laser amplitude $a = 0.7$, respectively.

amplitude relativistic EM solitons then begin to form inside plasma. Similarly, in the two cases, with the laser amplitude increasing, the transition from Raman cascade to photon condensation becomes more pronounced; more noticeable peaks around $0.5\omega_{pe}$ in frequency spectra for both reflected and transmitted EM waves can be observed.

As shown in figure 2.17 the electron plasma density n/n_0 and the energy density of EM field $E_y^2 + B_z^2$ snapshots for laser amplitude $a = 0.6$ case; very large amplitude localized EM soliton can be still detected. However, the interesting feature is that the observed soliton are now accelerated in the forward direction. Again, the soliton at the plasma-vacuum (rear) interface radiates its energy away in the form of low-frequency EM waves. As expected, very high transient transmissivity during the soliton radiation can be detected (see figure 2.15). The trajectory $x(t)$ of the EM soliton for the case of

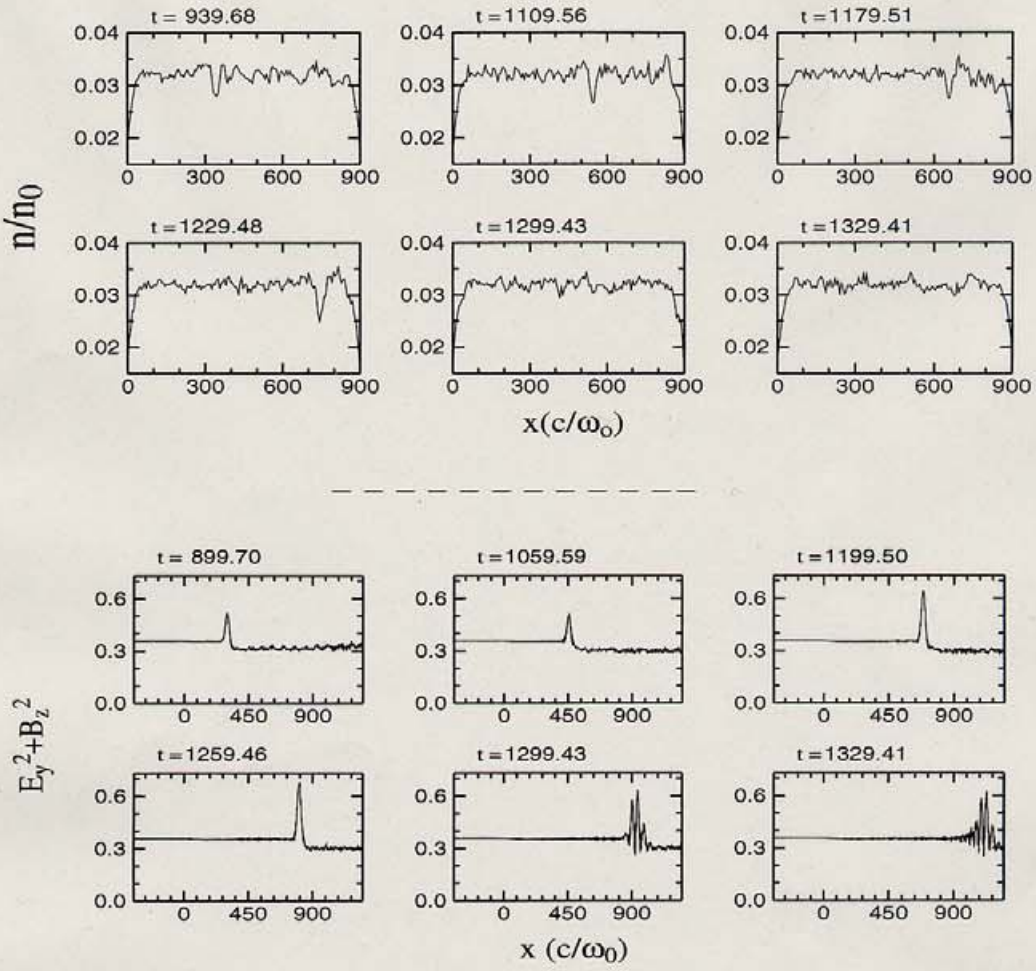

Figure 2.17: The snapshots for electron density n_e/n_0 (top) and for energy density of EM field $E_y^2 + B_z^2$ averaged over the laser period (bottom) in the case of plasma $n = 0.032 n_{cr}$, $L = 900c/\omega_0$ and laser amplitude $a = 0.6$, respectively.

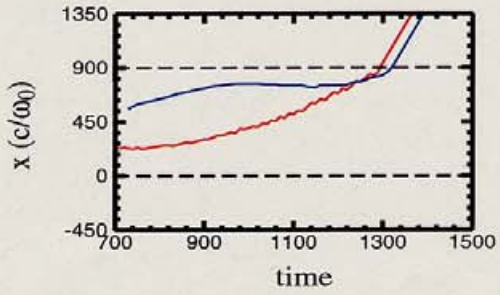

Figure 2.18: The plots for EM soliton orbits, the **red line** for the case of laser amplitude $a = 0.6$ and the **blue line** for the case of laser amplitude $a = 0.7$, respectively.

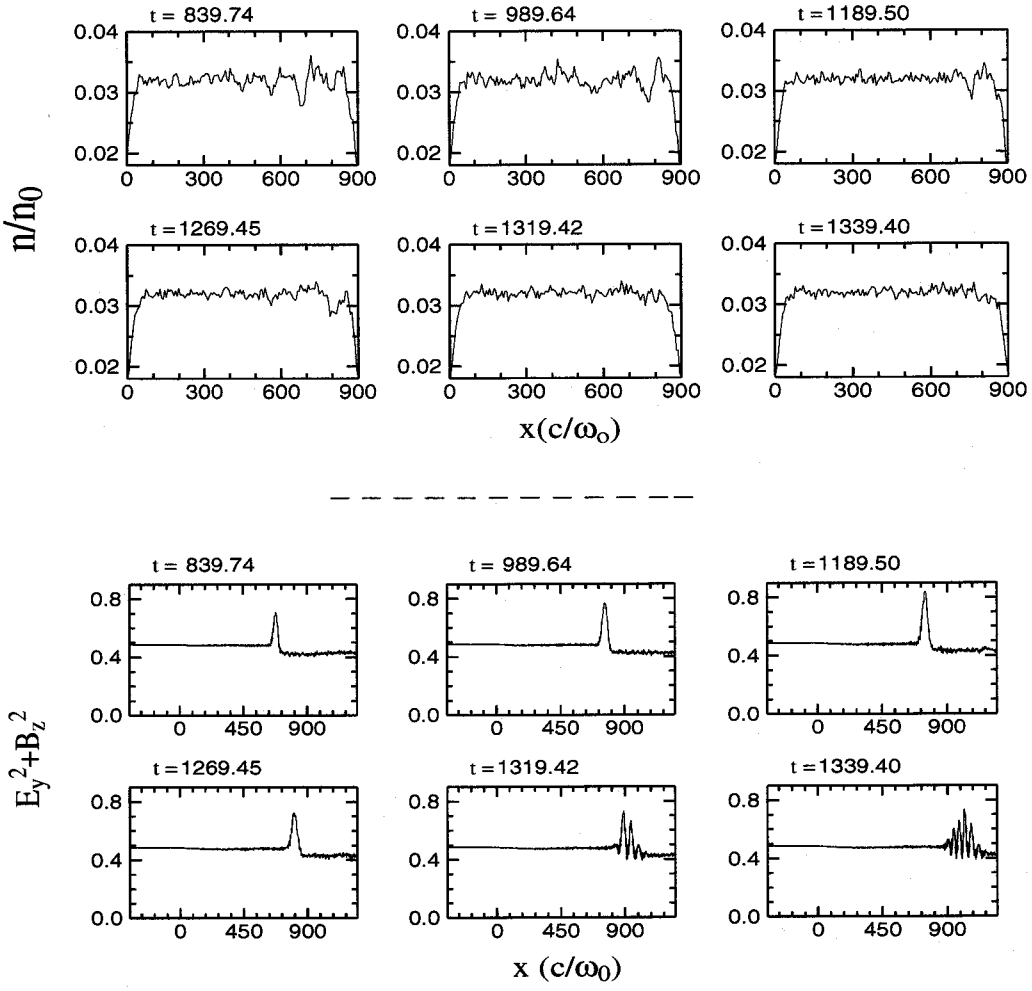

Figure 2.19: The snapshots for electron density n_e/n_0 (top) and for energy density of EM field $E_y^2 + B_z^2$ averaged over the laser period (bottom) in the case of plasma $n = 0.032n_{cr}$, $L = 900c/\omega_0$ and laser amplitude $a = 0.7$, respectively.

laser amplitude $a = 0.6$ is given in figure 2.18 (red line).

Like in the backward-accelerated EM soliton cases, the story for laser amplitude $a = 0.7$ case is the same as that for laser amplitude $a = 0.6$ case, as the plasma density snapshots n/n_0 and the energy density of EM field $E_y^2 + B_z^2$ snapshots in figure 2.19 and the trajectory $x(t)$ of the EM soliton in figure 18 (blue line) for plasma $n = 0.032n_{cr}$, $L = 900c/\omega_0$ and laser amplitude $a = 0.7$ case shown.

After the forward-accelerated EM solitons arrive at the plasma-vacuum interface, they radiate their energy away in the form of intense EM burst. By analyzing the frequency spectra of the forward-scattered EM waves in the vacuum regions (*see the last frequency spectra plots for transmitted EM waves, "t = 1290.77 to 1404.47" in figure 2.15 and " t = 1263.01 to 1376.71" in figure 2.16*), similarly, we again obtained the EM frequency

of the forward-accelerated EM solitons in vacuum regions are nearly $0.5\omega_{pe}$, which are the same as the backward-accelerated soliton ones.

Similarly, in the forward-accelerated soliton cases, they have the same EM and ES field structures as that in the standing and the backward-accelerated ones. As shown in figure 2.20, both for laser amplitude $a = 0.6$ (top) and $a = 0.7$ (bottom), respectively, the ES field E_x trapped inside soliton has one-cycle structure, and the corresponding transverse electric field E_y is the half-cycle structure and the magnetic field B_z is the one-cycle structure, respectively. The spatial EM field structure is oscillatory in time, but the ES field structure is not. The size of the soliton is about $5\lambda_0$, close to the electron plasma wavelength λ_{epw}. For the same reason with the backward-accelerated ones, it is difficult to analyze the ES frequency spectra of solitons due to their acceleration inside plasma. However, here, the frequency spectra of the ES field by taking the field at the position where is close to soliton region during analyzing time inside plasma, are also given in figure 2.21. In the two cases of the forward-accelerated EM solitons, the peaks with ES frequencies about $0.9\omega_0$ still can be observed, together with their EM frequencies $0.5\omega_{pe} \approx 0.1\omega_0$ what detected in vacuum regions, perhaps, one also can explain this phenomenon roughly by a 3-wave resonant coupling process.

For both standing and accelerated solitons, the EM energy density profile shows a difference between the front and rear side of the soliton, the front value is always large; with the laser amplitude increasing, the difference becomes larger and larger. This is because in the large laser amplitude case, the amplitude of the observed EM soliton is larger than that in the lower laser amplitude case. The difference of EM energy density is mainly converted into the EM energy of the soliton. The steep EM energy density gradient in the short transition layer of the soliton length (c/ω_p – classical skin depth) corresponds to the ponderomotive force which acts on plasma electrons.

Furthermore, for same simulation parameters, by varying the laser amplitude, in the ranges of laser amplitude $a < 0.3$ or $a \geq 1.0$, this sort of large amplitude localized relativistic EM solitons are not observed in our 1D-PIC simulations.

2.3 Influence of plasma length on the acceleration of large amplitude EM soliton

Up to now, we are mainly concentrated ourselves on the SRS, Raman cascade-into-condensation and large amplitude relativistic EM solitons, induced by linearly-polarized intense laser pulse propagating inside underdense homogeneous plasma. In all above simulations, besides the laser amplitude is taken as one control parameter, other simulation parameters are kept same. Namely, in the case of plasma density $n = 0.032n_{cr}$ and length $L = 900c/\omega_0$, by changing laser amplitude, the standing-, backward-accelerated

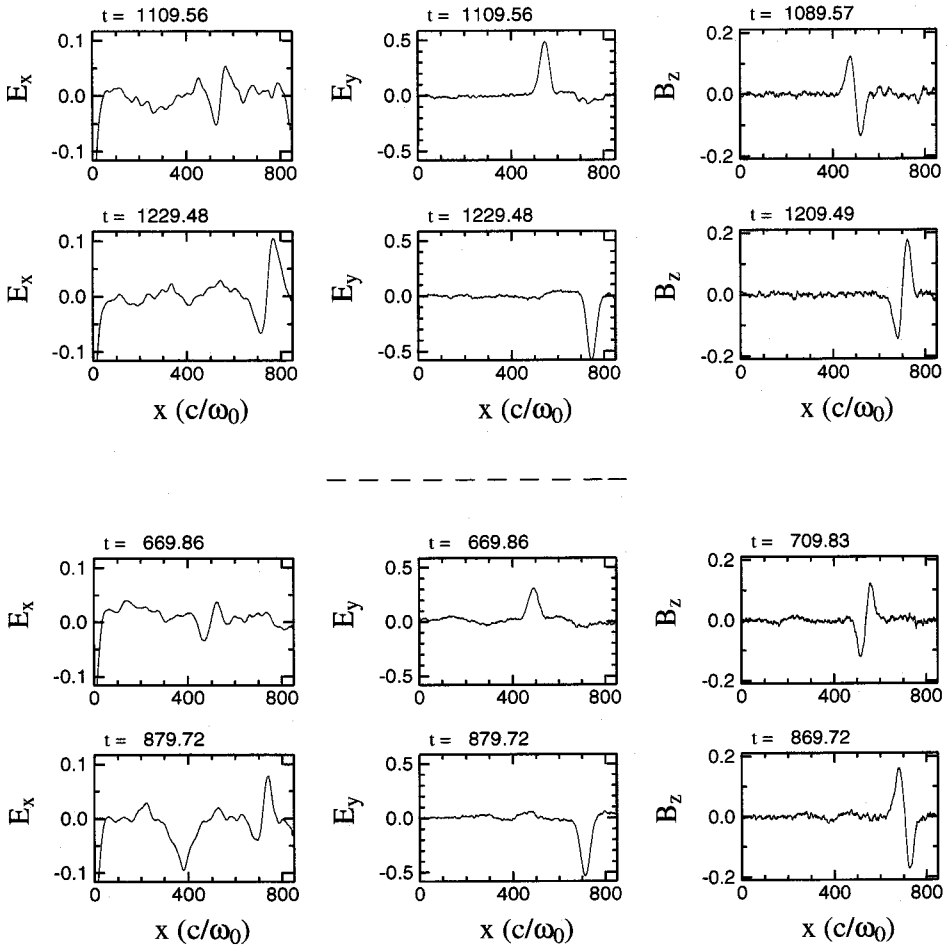

Figure 2.20: The snapshots for EM field structure (averaged over laser wavelength λ_0) and ES field structure (averaged over EPW wavelength λ_{epw}) in the case of plasma density $n = 0.032n_{cr}$ and length $L = 900c/\omega_0$. The top plots for the case of laser amplitude $a = 0.6$ and bottom plots for the case of laser amplitude $a = 0.7$, respectively.

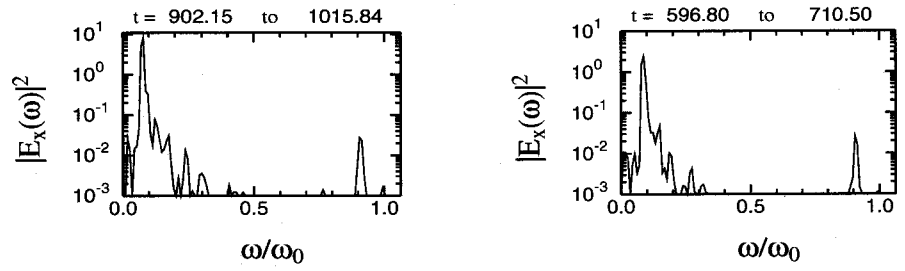

Figure 2.21: The plots for frequency spectra of ES wave measured inside plasma in the case of plasma $n = 0.032n_{cr}$ and $L = 900c/\omega_0$. The left one for the case of laser amplitude $a = 0.6$ and right one for the case of laser amplitude $a = 0.7$, respectively.

and forward-accelerated large amplitude relativistic EM solitons are observed.

One may ask, if we keep the laser amplitude unchangeable, only by changing plasma length, what kind of different results on the acceleration of the EM soliton can we obtain from PIC simulations? The following paragraph will answer this question by omitting the physics details before the formation of the EM soliton.

Besides two parameters, *the linearly-polarized laser amplitude a and plasma length L, are taken as two control parameters*, all the other simulation parameters are the same as used before. In the simulations, the simulation system length $3L(c/\omega_0)$, plasma length is L, it begins at $x = 0$ and ends at $x = L$, in the front and rear side of the plasma layer there are two vacuum regions with the same length L. Plasma length L changes from $400c/\omega_0$ to $1300c/\omega_0$ by taking the same length interval $100c/\omega_0$. Plasma density and temperature are $n = 0.032n_{cr}$ and $T_e = 350eV$, respectively. Still, ions are typically kept immobile as a neutralizing background.

The results on the acceleration of relativistic EM soliton for several different simulations are tabulated in Table 2.1. In the following sections, we will explain the simulation results by using the case of laser amplitude $a = 0.5$.

Table 2.1: The acceleration of EM soliton for different plasma length and laser amplitude, the other simulation parameters are the same as the above simulations.

$L(c/\omega_0)$	500	600	700	800	900	1000	1100	1200	1300	1400
$a = 0.3$	No	No	No	No	S	B	No	B+S*	B	B+B → B
$a = 0.5$	B	B	F	B+F	B+F*	B	F*+F*	B+F	F	F
$a = 0.7$	F	F	F*	F	F	No	No	F	No	F

*Here 'No', 'S', 'F' and 'B' stand for no, standing-, forward- and backward-accelerated EM solitons, respectively. The soliton with the mark * demonstrates the amplitude of the EM soliton is too weak to see. The total simulation time is* $\omega_0 t < 17000$.

2.3.1 Backward-accelerated large amplitude EM soliton

In the three cases for plasma length $L = 500c/\omega_0$, $600c/\omega_0$ and $1000c/\omega_0$, after the SRS, Raman cascade-into-condensation and electron acceleration, with time goes on, the spatially localized large amplitude backward-accelerated relativistic EM solitons eventually form. As the backward-accelerated EM solitons approach the plasma-vacuum interface, they start to radiate their energy away in the form of low-frequency EM wave due to a non-adiabatic interaction with the plasma-vacuum boundary, as a result, again one can observe very high transient reflectivity than that of the B-SRS. Here, the energy density

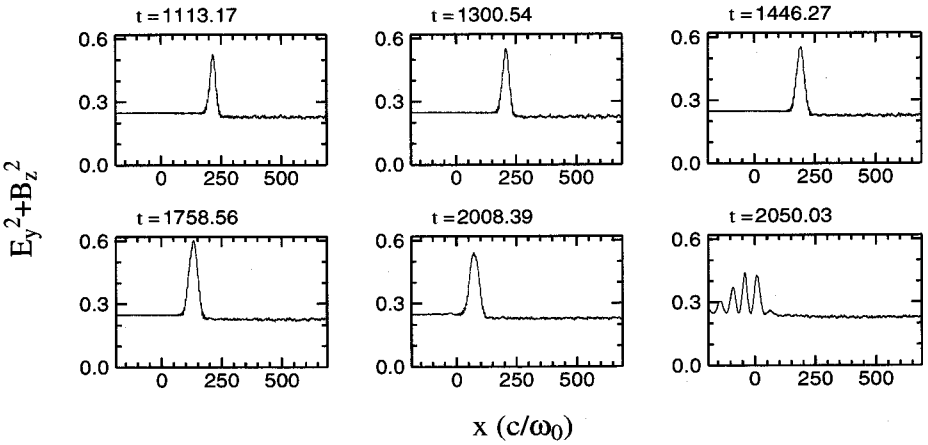

Figure 2.22: The snapshots for energy density of EM field $E_y^2 + B_z^2$ averaged over the laser period for the case of plasma density $n = 0.032n_{cr}$, length $L = 500c/\omega_0$ and laser amplitude $a = 0.5$, respectively.

of EM field $E_y^2 + B_z^2$ snapshots for the case of plasma length $L = 500c/\omega_0$ and laser amplitude $a = 0.5$ is shown in figure 2.22.

However, in the plasma length $L = 400c/\omega_0$ and laser amplitude $a = 0.5$ case, we did not observe this kind of the EM soliton within our simulation time.

2.3.2 Forward-accelerated large amplitude EM soliton

By performing simulations for the cases with plasma length $L = 700c/\omega_0$, $1300c/\omega_0$, $1400c/\omega_0$, as the energy density of EM field snapshots for the case with $L = 700c/\omega_0$ and $a = 0.5$ in figure 2.23 shown; the EM soliton dynamics appear different to that the backward-accelerated ones, i.e., for plasma length $L = 500c/\omega_0$, $600c/\omega_0$ and $1000c/\omega_0$ cases. In the three simulations, the observed EM solitons are now accelerated forward. Again, the EM soliton arrives at the plasma-vacuum (rear) interface radiates its energy away in the form of low-frequency EM wave. Similarly, one can expect to detect a very high transient transmissivity of EM field energy during the soliton radiation.

2.3.3 Coexistence of backward and forward accelerated EM solitons

In another three simulations for plasma length $L = 800c/\omega_0$, $900c/\omega_0$ and $1200c/\omega_0$ cases, we found that, both the backward-accelerated and the forward-accelerated large amplitude relativistic EM solitons are successively observed. The more details is that, one backward-accelerated EM soliton is first formed, after the backward-accelerated EM

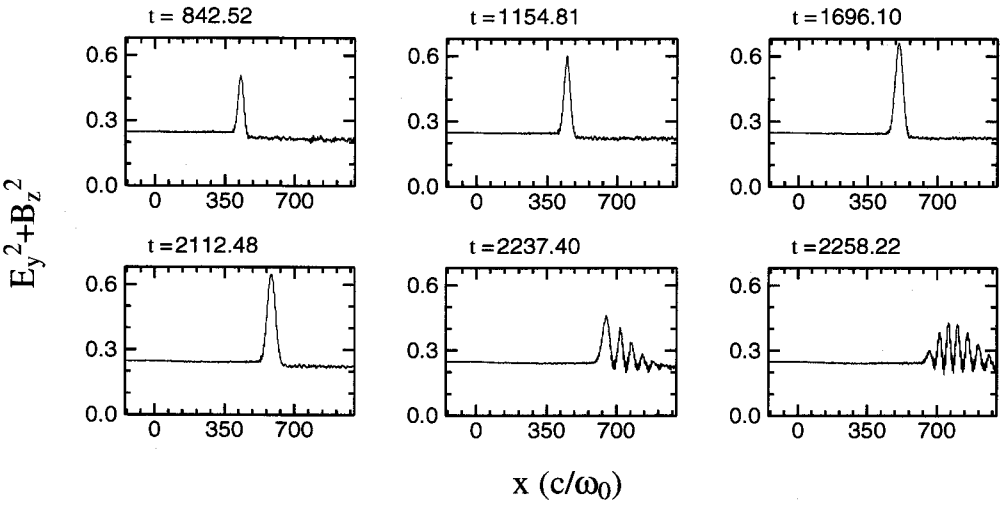

Figure 2.23: The snapshots for energy density of EM field $E_y^2 + B_z^2$ averaged over the laser period for the case of plasma density $n = 0.032n_{cr}$, length $L = 700c/\omega_0$ and laser amplitude $a = 0.5$, respectively.

soliton accelerate backward in plasma or it disappear in plasma-vacuum boundary, an another EM soliton then begins to emerge in plasma, after the new soliton formed, the difference to that first backward-accelerated one is, it is accelerated forward into the plasma-vacuum interface.

In order to understand the formation and acceleration of solitons, we have plotted the energy density of EM field snapshots for plasma length $L = 1200c/\omega_0$ in figure 2.24; the first three plots for backward-accelerated EM soliton and another three plots for forward-accelerated one. As a result, as shown in figure 2.25 the plots for the reflectivity and transmissivity of EM wave, after the backward-accelerated soliton arrived at left plasma-vacuum interface, one can observe a very high transient reflectivity, after that, a very high transient transmissivity can then be detected during the forward-accelerated soliton radiation at the right plasma-vacuum interface. However in the cases of $L = 800c/\omega_0$ and $900c/\omega_0$, the second forward-accelerated EM solitons have too weak amplitude compared with that of the first backward-accelerated ones.

In the all soltion cases, for the backward-, the forward- and the coexistent-accelerated EM solitons, the ES and EM field structure inside the soliton are the same as before, namely, the ES field structure E_x is the one-cycle structure in space, while the corresponding EM structure, for electric field E_y is the half-cycle structure and magnetic field B_z is the one-cycle structure in space, respectively. The spatial EM structure is oscillatory in time, but the ES structure is not. The size of the EM soliton is about $5 \sim 12\lambda_0$, which approximately equal to $1 \sim 2\lambda_{epw}$. Similarly, the EM frequency of the solitons in vacuum are measured nearly about $0.5\omega_{pe}$.

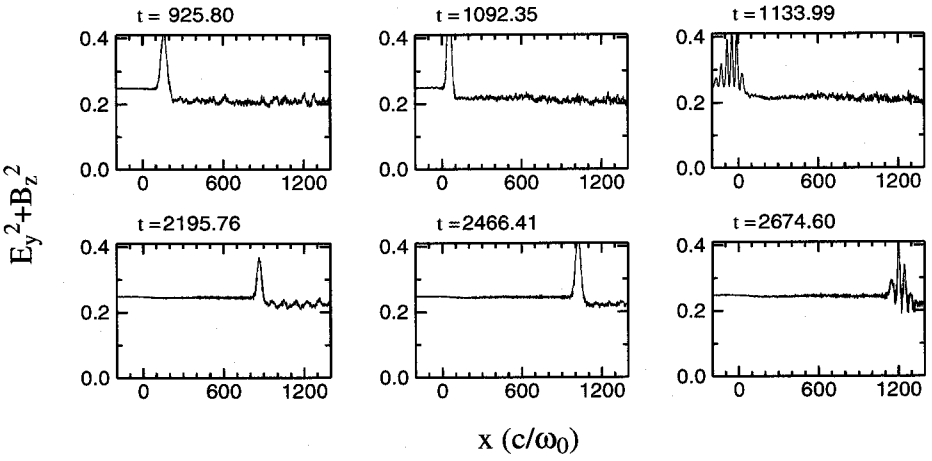

Figure 2.24: The snapshots for energy density of EM field $E_y^2 + B_z^2$ averaged over the laser period in the case of plasma density $n = 0.032n_{cr}$, length $L = 1200c/\omega_0$ and laser amplitude $a = 0.5$, respectively.

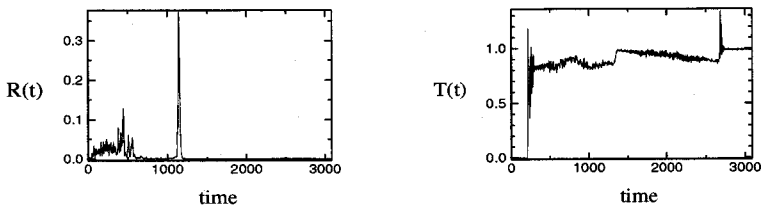

Figure 2.25: The reflectivity and transmissivity of EM wave plots for the case of plasma $n = 0.032n_{cr}$, $L = 1200c/\omega_0$ and laser amplitude $a = 0.5$, respectively. To calculate the reflectivity and transmissivity, the EM fields at the left position and at right position both are $100c/\omega_0$ long distance away from plasma is used in the simulation.

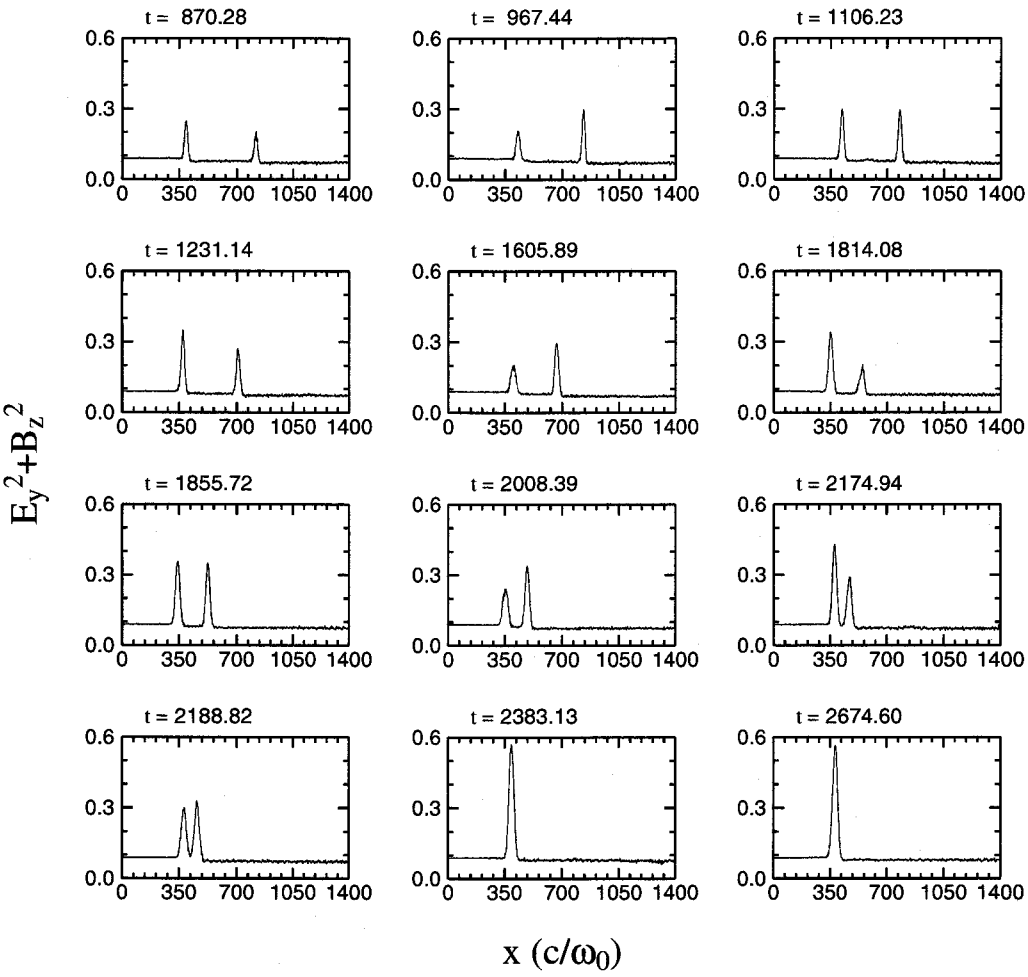

Figure 2.26: The snapshots for energy density of EM field $E_y^2 + B_z^2$ averaged over the laser period from 1D-PIC simulation in the case of plasma density $n = 0.032n_{cr}$, length $L = 1400c/\omega_0$ and laser amplitude $a = 0.3$, respectively.

2.4 The merging of two large amplitude EM solitons

By performing many simulations, we also found that, in the case of plasma length $L = 1400c/\omega_{pe}$ and laser amplitude $a = 0.3$, as shown in figure 2.26, two large amplitude relativistic EM solitons emerge and co-exist inside plasma. After their formation, the two EM solitons both are accelerated backward with different accelerations, with time goes on, the back one can overtake the front one; after that, the two EM solitons then merge together to form a new EM soliton with the large amplitude nearly equals to the sum of two EM solitons. This new formed large amplitude EM soliton exists and does not separate again within our simulation time.

2.5 Discussion on the acceleration of large amplitude relativistic EM solitons

In this section, we will briefly discuss the mechanism of the acceleration of relativistic EM solitons, electron acceleration by large amplitude relativistic EM solitons, and the influences of plasma temperature and ion dynamics on the formation of the EM solitons.

2.5.1 The acceleration of large amplitude EM solitons

The acceleration of the relativistic EM solitons has been studied by many authors. And up to now, it is reported that, in the homogeneous plasmas, solitons have been found to exist for a long time, close to the regions where they were generated; however, in inhomogeneous plasmas, solitons are accelerated with the acceleration proportional to the gradient of plasma density towards the low density side [62, 74]. When a soliton reaches some critical plasma region, for example, the plasma-vacuum interface, it radiates away its energy in the form of a short burst EM radiation.

From this point of view, apart from the standing relativistic EM soliton, we can not explain our accelerated ones. In all our simulations, the plasma density in the front and back of the soliton regions is nearly homogeneous during the lifetime of the EM solitons. Recently, we have put some attention into the research on the relativistic EM solitons. As a new point on the acceleration of relativistic EM soliton, we noted that, in addition to the inhomogeneity of plasma density, the acceleration of relativistic EM soliton depends upon, not only the incident laser amplitude, but also upon the plasma length [75].

In fact, the motion of relativistic EM soliton depends upon the motion of the electrons inside soliton. In the nonlinear relativistic case, basically, the longitudinal electron motion is determined by the balance of the ES field and the ponderomotive force terms [58, 18], in the normalized units,

$$\frac{\partial p_x}{\partial t} = -E_x - \frac{\partial \gamma}{\partial x} \tag{2.7}$$

Here, p_x, E_x and γ stand for the momentum, ES field and relativistic factor, respectively.

Which direction, *forward or backward*, that the soliton can be accelerated, it depends upon, which term, *the ES field or the ponderomotive force*, is prevailing. It should be noted that, the two terms are the averaged effect for all electrons inside soliton region.

For both backward- and forward-accelerated solitons, the EM energy density profile shows a difference between the front and rear side of the soliton, the front value is always larger; with the laser amplitude increasing, the difference becomes larger and larger. This

is because in large laser amplitude case, the amplitude of the observed relativistic EM soliton is larger than that in the lower laser amplitude case. The difference of EM energy density is mainly converted into the EM energy of the soliton. The steep EM energy density gradient in the short transition layer of the soliton length (c/ω_p – classical skin depth) corresponds to the ponderomotive force which acts on plasma electrons. The resulting ponderomotive acceleration pushes the electron cavity with the soliton in the forward direction. Basically, the longitudinal electron motion is determined by the balance of the ES field and the ponderomotive force terms [58]. The large flow of relativistic electrons generated in forward direction (due to SRS, etc.) which drives ES fields, gets compensated by a cold (bulk) return current which

moves plasma electrons backwards. Possibly, this is why moderately large solitons are found to accelerate backwards. However, if at very large amplitudes, the ponderomotive term prevails, the acceleration of the EM soliton is reversed and solitons are pushed forwards.

2.5.2 Electron acceleration by large amplitude EM soliton

Particle acceleration by soliton has been studied by some authors. This is caused by the energy gain during the ion interaction with the EM field and/or ES field trapped inside soliton. Soliton propagating with high velocity provides the wakeless regions with regular electric and magnetic fields, with which the particle can interact and gain the energy, and the soliton energy transforms into the energy of the fast particles [57].

From our simulation data, we found that, at appropriate laser amplitude case, the ES field and EM field trapped inside soliton have fine spatial structures. Especially, its ES field nearly keeps unchanging during its lifetime. In figure 2.27, we plotted the ES field snapshots for the case of the plasma length $L = 500c/\omega_0$ and laser amplitude $a = 0.5$. In this case, the ES field trapped inside soliton has a very fine sine function structure and has almost unchanged amplitude with time. Its ES field inside soliton can be expressed $E_s(x) \approx -E_{max} \sin(2\pi x_s/L_s)$ approximately, where $L_s \approx 75c/\omega_0$ is soliton spatial length (size) and $E_{max} \approx 0.12m\omega_0 c/e$ is its amplitude, respectively; coordinate variable changes from $x = 0$ to $x = L_s$. Although the total area under the curve is zero, there is no net energy gain from the ES field when electrons traveling the whole soliton region; however we can use the positive part of ES field to accelerate electrons backward, or accelerate electrons forward by using negative part of ES field. It is easy to estimate the maximum electron net energy gain, which comes from the electron acceleration backward or forward by half ES field of the soliton region, that is, $E^{max} \approx |\int_0^{L_s/2} eE(x)dx| = eE_{max}L_s/\pi$. By substituting the values of L_s and E_{max}, one can estimate that, the maximum energy of an electron accelerated by half ES field inside soliton is $E^{max} \approx 1.46MeV$, approximately.

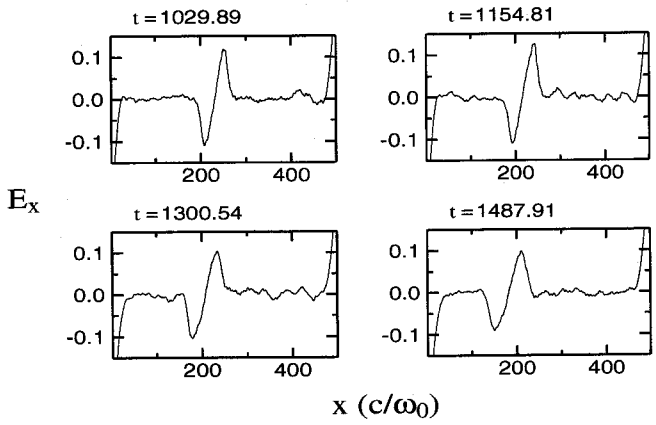

Figure 2.27: The snapshots for ES field E_x averaged over electron plasma period in the case of plasma $n = 0.032n_{cr}$, $L = 500c/\omega_0$ and laser amplitude $a = 0.5$, respectively.

2.5.3 Influences of plasma temperature and ion dynamics on the formation of large amplitude EM soliton

The plasma temperature and ion dynamics also have some influences on the formation and the acceleration of the large amplitude relativistic EM soliton.

In order to investigate the plasma temperature effect, we choose the plasma length L, the laser amplitude a and the plasma temperature T_e, as three control parameters, the other simulation parameters are kept the same as before. Several different simulations are performed and the results are tabulated in Table 2.2. For the three cases of $L = 500c/\omega_0$, $a = 0.5$ and $T_e = 1keV$, $2keV$ and $5keV$, the backward-accelerated relativistic EM solitons are observed as obtained in the case of $T_e = 350eV$. For the another three cases of $L = 900c/\omega_0$, $a = 0.5$ and $T_e = 1keV$, $2keV$ and $5keV$, besides the $T_e = 5keV$ case, the observed EM solitons are the same as $T_e = 350eV$ case, i.e., the backward-accelerated relativistic EM soliton. However, in the $T_e = 5keV$ case, a large initial thermal pressure could have lead to a different physical regime, perhaps, for the simulation parameters we took, the condition for the soliton formation was not satisfied. For the last three cases of $L = 900c/\omega_0$, $a = 0.7$ and $T_e = 1keV$, $2keV$ and $5keV$, the forward-accelerated relativistic EM solitons are observed, as has been shown in the case of $T_e = 350eV$.

Table 2.2: Temperature effect on EM soliton dynamics.

$T_e(eV)$	350	1000	2000	5000
$L = 500(c/\omega_0)$, $a = 0.5$	Backward	Backward	Backward	Backward
$L = 900(c/\omega_0)$, $a = 0.5$	Backward	Backward	Backward	No soliton
$L = 900(c/\omega_0)$, $a = 0.7$	forward	forward	forward	forward

The ion dynamics may have some influence on the formation of the relativistic EM soliton because the observed relativistic EM solitons are formed at a little later moment. By choosing the plasma length L and laser amplitude a as two control parameters, three simulations with electron and ion temperature $T_{ion} = T_e = 350eV$, the mass ratio of ion to electron $M_i/m_e = 1836$, are performed and the simulation results are tabulated in Table 2.3. All results are the same as that of the immobile ion cases. In the case of plasma length $L = 500c/\omega_0$ and laser amplitude $a = 0.5$, we found that, the ion dynamics (motion) could reduce the EM energy density of the soliton (amplitude) and slightly change the size of the EM soliton. The same type, i.e., the backward-accelerated large amplitude localized relativistic EM solitons, could still be observed. In the case of plasma length $L = 900c/\omega_0$ and laser amplitude $a = 0.3$, the standing large amplitude localized relativistic EM soliton; while, in the case of plasma length $L = 900c/\omega_0$ and laser amplitude $a = 0.7$, the forward-accelerated large amplitude localized relativistic EM solitons, could still be observed with reduced amplitude and slightly-changed size. In the three cases, large ion density cavities are also formed during the formation and existence of the relativistic EM solitons.

Table 2.3: Ion effect on the EM soliton dynamics

$T_e = T_{ion}(eV)$	350	350
M_{ion}/m_e	1836	∞ (motionless ions)
$L = 500(c/\omega_0)$ and $a = 0.5$	Backward	Backward
$L = 900(c/\omega_0)$ and $a = 0.3$	Standing	Standing
$L = 900(c/\omega_0)$ and $a = 0.7$	Forward	Forward

Chapter 3

Generation of ion-vortices in ion phase-space

Electron-acoustic wave (EAW), as a mode of internal plasma ES waves, has been studied by early authors. By examining the linearized Vlasov ES dispersion relation and ignoring particle trapping effect, EAW solutions in the long wavelength limit are obtained [20, 21, 22]. However, other analytical studies of nonlinear Vlasov-Maxwell solutions have been found that strong electron trapping can occur even for small amplitude ES wave, resulting in undamped nonlinear traveling wave solutions, the so-called BGK (Bernstein-Greene-Kruskal) modes allowing the EAW with a lower phase velocity to exist [23, 24, 25].

The stimulated electron-acoustic wave scattering (SEAWS), *as a novel stimulated scattering*, was proposed by Montgomery et al., in the recent single hot spot experiment to reinterpret an underdense homogeneous plasma experiment data from the Trident laser facility [12, 13]. In their experiment, plasma density $n \approx 0.03 n_{cr}$, plasma temperature $T_e \approx 350eV$, plasma length $L_p \approx 900c/\omega_0$, laser intensity $I \approx 1.6 \times 10^{16} W/cm^2$, respectively, they observed a wave in the backscattered spectra with phase velocity $v_{ph} \approx 1.4 v_{the}$ besides the backscattered EM signal which comes from the stimulated Raman scattering (SRS). It was shown that, among electronic instabilities, stimulated scattering of laser light from the trapped EAW (T-EAW) with frequency $\omega < \omega_{pe}$ can possibly explain the second anomalous backscattered signal apart from the first one comes from SRS.

Recently, this novel SEAWS has been studied by means of fully relativistic EM one-dimensional particle-in-cell (1D-PIC) simulations [14, 15, 16, 17]. In their simulations, a linearly-polarized intense laser pulse and a plasma layer at a subcritical density range, i.e., $n_{cr}/4 < n/\gamma < n_{cr}$ *(γ is relativistic factor), which are overdense for standard SRS*, are used. In the early stage of the SEAWS, the spectrum can well-explained by a resonant three-wave parametric decay of the relativistic laser pump into the slowed Stokes light sideband with $\omega_s \sim \omega_{pe}$ and the T-EAW with $\omega_{eaw} < \omega_{pe}$. They stated that the ion dynamics does not play a significant role in the growth of SEAWS instability. Here, it should be noted that the plasma layers used in their simulations are shorter than

$100c/\omega_0$.

Similar to that SRS instability, the SEAWS instability can also be explained as three-wave resonant decay of an incident laser EM wave (ω_0, k_0) into a scattered (Stokes) EM wave (ω_s, k_s) plus an EAW (ω_{eaw}, k_{eaw}) with the corresponding matching conditions for frequencies and wave numbers as follows:

$$\omega_0 = \omega_s + \omega_{eaw}, \quad \mathbf{k}_0 = \mathbf{k}_s + \mathbf{k}_{eaw} \tag{3.1}$$

We also put some efforts on the research of this novel SEAWS by using plasma layer length $L = 100c/\omega_0$, which is longer than that in the previous simulations [14, 15, 16, 17]. Similarly, the frequency spectra in the early stage of the SEAWS can be well-explained by a resonant three-wave parametric decay of the relativistic laser pump into the slowed Stokes light sideband with $\omega_s \sim \omega_{pe}$ and the T-EAW with $\omega_{eaw} < \omega_{pe}$.

Additionally, we also found, in nonlinear saturation of SEAWS instability, there is a rapid growth and strong localization of the Stokes EM wave by forming narrow intense EM soliton-like structures with (downshifted) laser light trapped inside. The train of relativistic EM solitons-like gets irradiated through the front vacuum-plasma boundary in a form of intense coherent reflection of the downshifted laser light. Large T-EAW excited in the plasma quickly heats up electrons to relativistic energies which eventually suppresses the SEAWS instability. In the case of long plasma layer, the ion dynamics does not play a significant role on SEAWS in its early stage. Its early physics behaviors are almost the same whether the ion dynamics is taken into account or not. As time goes on, an ion ES wave can be excited and ion ES wave breaks. At the breaking position, there appear large amplitude relativistic EM soliton and ion-vortex (ion-hole) in ion phase-space due to the ion acceleration and trapping by the formed EM soliton. As this EM soliton moves backwards, several ion-vortices (ion-holes) successively are formed.

The generation of the ion-vortices, as a new research results, will be the kernel of this chapter. In the following parts of this thesis, we put a term "T (trapped)" before SEAWS, namely, "T-SEAWS", because of the EAW belongs to the strong trapped one.

3.1 Simulation model

The geometry of simulation is the same as shown in Sketch 2.1. In the simulations, fully relativistic EM 1D3V-PIC code is used. The length of simulation system is $500c/\omega_0$, where c and ω_0 is the speed and carrier frequency of laser pulse, respectively. Plasma length is $100c/\omega_0$, it begins at $x = 0c/\omega_0$ and ends at $x = 100c/\omega_0$, in the front and back sides of the plasma, there are two $200c/\omega_0$ long vacuum regions. The number of cells is 20 per 1 c/ω_0, 100 electrons and 100 ions are put in each cell. Linearly-polarized laser

with its electric field E_0 directed along y direction, is launched at $x = -100c/\omega_0$. By taking the EM fields at the left and the right positions both are $50c/\omega_0$ long distance away from plasma, the reflectivity and transmissivity are measured, respectively. The electrons entering the vacuum region build a potential barrier that prevents electrons of leaving the plasma. For these electrons as well as for outgoing EM waves, two $50c/\omega_0$ long additional numerical damping regions are used at the ends of the system. The time, electric field and magnetic field are normalized to $2\pi/\omega_0$, $m_e\omega_0 c/e$ and $m_e\omega_0/e$, respectively; time is taken as zero, $t = 0.0$, when laser pulse arrives at left vacuum-plasma boundary.

3.2 Stimulated trapped electron acoustic wave scattering (T-SEAWS)

The first simulation has been done by using plasma length $L = 100c/\omega_0$, plasma density $n = 0.6n_{cr}$, electron and ion temperatures $T_e = 5T_{ion} = 1keV$, mass ratio of ion to electron $M_i/m_e = 1836$ and the normalized laser amplitude $a = 0.6$, where n_{cr} is the critical density of laser pulse.

In our simulations, plasma density are taken as $n > 0.25n_{cr}$, where the standard SRS is forbidden. It is found that when the laser amplitude $a > 0.4$, the T-SEAWS instability begins to take place. At the linear stage of the T-SEAWS instability, *as shown in figure 3.1, the plots for frequency spectra of reflected EM wave in vacuum and ES wave inside plasma*, the frequency spectra can be well explained by a resonant 3-wave parametric decay of intense laser pump into the slowed Stokes EM sideband and the T-EAW. The backscattered EM wave in vacuum regions is found to be driven and grows at frequency $\omega_s \approx 0.64\omega_0$, which is approximately equals to the perturbed electron plasma frequency $\omega_{pe}/\gamma^{1/2} \sim 0.69\omega_0$, where $\gamma = (1 + a^2)^{1/2}$ is relativistic factor, while the corresponding EAW detected inside plasma is $\omega_{eaw} \approx 0.40\omega_0$. Note that the natural EPW mode $\omega_{pe}/\gamma^{1/2} \approx 0.69\omega_0$ is also driven weakly in this process. *In figure 3.2, the plots for the wave number of the EM wave and ES wave both measured inside plasma are given.* One can observe that the wave number of the EM wave inside plasma have two peaks, one $k_s^p \approx 0.12k_0$ and another $k_0^p \approx 0.80k_0$ correspond to backscattered EM wave and laser EM wave which propagates inside plasma, while the corresponding wave number for EAW inside plasma is $k_{eaw} \approx 0.92k_0$, where $k_0 = \omega_0/c$ is the wavenumber of laser EM wave in vacuum. The perturbed electron plasma frequency $\omega_{pe}^* \approx 0.61\omega_0$ is smaller than $\omega_{pe}/\gamma^{1/2} \approx 0.69\omega_0$, because in the regions of strong EM wave stronger relativistic effect results in the electron plasma frequency decreasing more noticeable. In the early stage of the T-SEAWS instability, the corresponding resonant matching conditions for frequency $\omega_0 = \omega_s + \omega_{eaw}$ and for wave number $k_0^p = -k_s^p + k_{eaw}$ are well satisfied. The EM waves for both pump and Stokes satisfy standard dispersion relation $\omega_{0,s}^2 = \omega_{pe}^{*2}/\gamma + c^2(k_{0,s}^p)^2$.

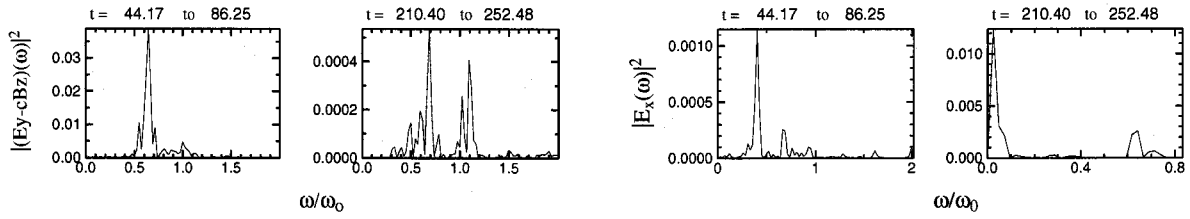

(a). Both electron component and ion component are considered. In the simulation, the mass ratio $M_i/m_e = 1836$ and temperature $T_e = 5T_{ion} = 1.0keV$ are used.

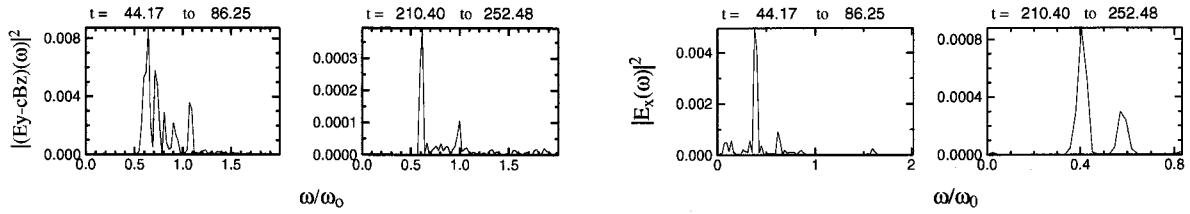

(b). Only electrons are considered. Ions as neutralized background are kept immobile.

Figure 3.1: The plots for the frequency spectra of reflected EM wave measured in vacuum region and ES wave measured inside plasma in the case of plasma length $L = 100c/\omega_0$, density $n = 0.6n_{cr}$ and laser amplitude $a = 0.6$, respectively.

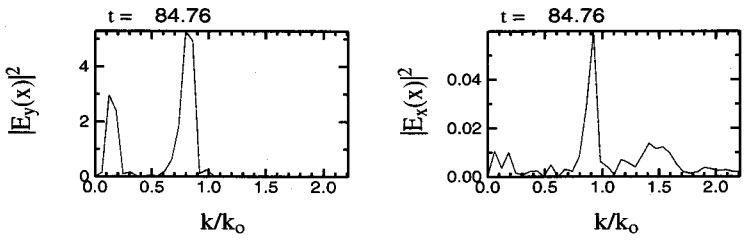

(a). Both electron component and ion component are considered. In the simulation, the mass ratio $M_i/m_e = 1836$ and temperature $T_e = 5T_{ion} = 1.0keV$ are used.

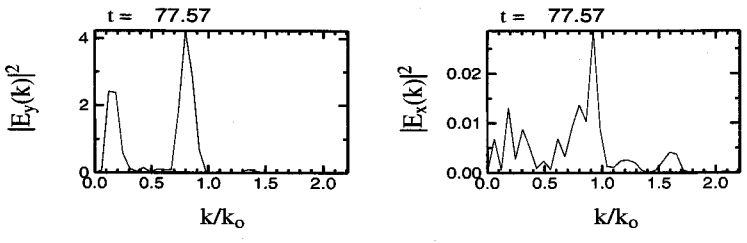

(b). Only electrons are considered. Ions as neutralized background are kept immobile.

Figure 3.2: The plots for the wave numbers of reflected EM wave and ES wave both measured inside plasma in the case of plasma length $L = 100c/\omega_0$, density $n = 0.6n_{cr}$ and laser amplitude $a = 0.6$, respectively.

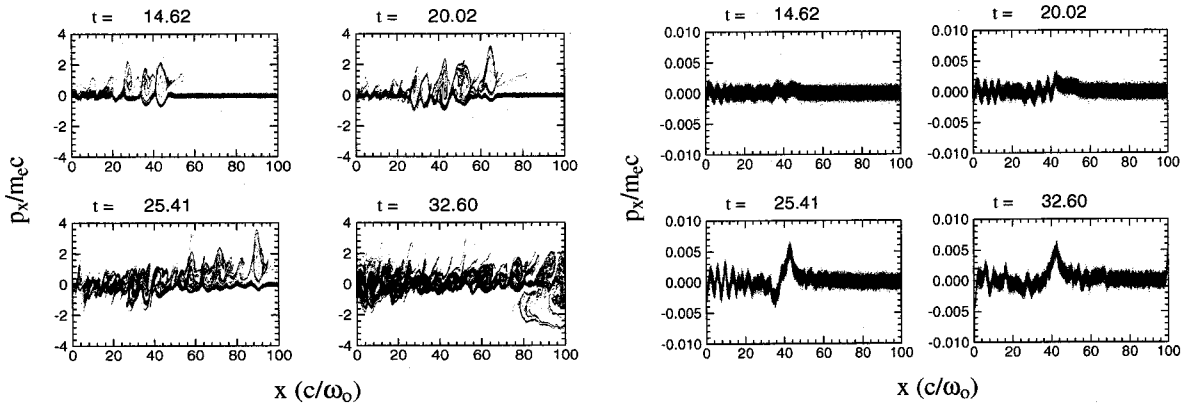

(a). Both electron component and ion component are considered. In the simulation, the mass ratio $M_i/m_e = 1836$ and temperature $T_e = 5T_{ion} = 1.0keV$ are used.

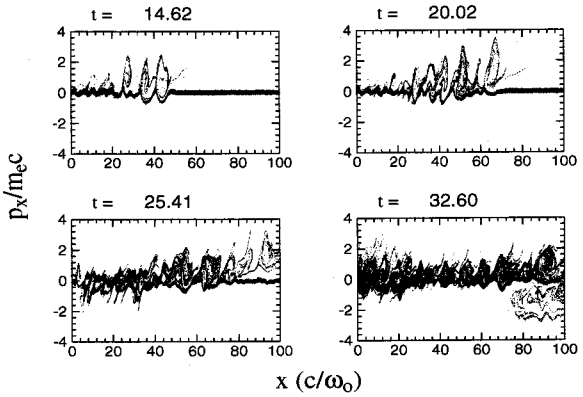

(b). Only electrons are considered. Ions as neutralized background are kept immobile.

Figure 3.3: The phase-space $x - p_x$ snapshots for both electron component and ion component in the case of plasma length $L = 100c/\omega_0$, density $n = 0.6n_{cr}$ and laser amplitude $a = 0.6$, respectively.

During the stage of the T-SEAWS instability, *as shown in figure 3.3, the phase-space* $x - p_x$ *snapshots*, large parts of electrons are trapped by the potential of trapped EAW. This is the reason why we put a term 'trapped' before 'SEAWS', namely, T-SEAWS.

To illustrate the onset and growth of the T-SEAWS instability, *in figure 3.4, the plots for the temporal evolution of dominant backscattered EM mode* $\mid E_y(k) \mid^2$ *and EAW mode* $\mid E_x(k) \mid^2$ *both measured inside plasma, are given.* We then can see its temporal evolution process clearly, the linear process in its early stage, following nonlinear process.

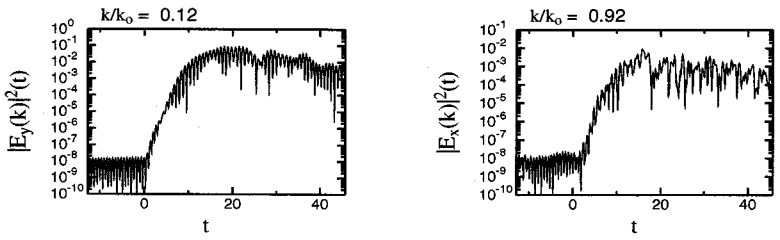

(a). Both electron component and ion component are considered. In the simulation, the mass ratio $M_i/m_e = 1836$ and temperature $T_e = 5T_{ion} = 1.0keV$ are used.

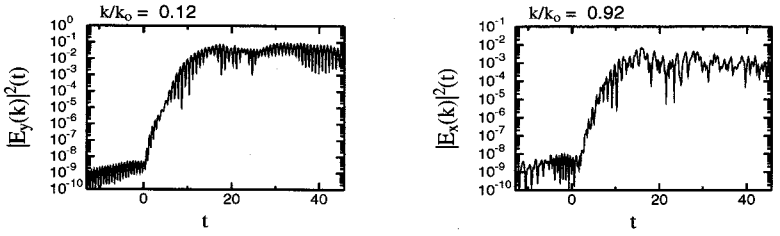

(b). Only electrons are considered. Ions as neutralized background are kept immobile.

Figure 3.4: The temporal growth plots for backscattered EM mode and EAW ES mode both measured inside plasma in the case of plasma length $L = 100c/\omega_0$, density $n = 0.6n_{cr}$ and laser amplitude $a = 0.6$, respectively.

If we assume that both EM mode and ES modes approximately satisfy $E_k(t) \sim E_k(0)e^{\gamma t}$, by using the data of figure 3.4 one can approximately calculate their corresponding growth in the linear stage of T-SEAWS instability. The growth rate for backscattered EM mode is $\gamma_s \approx 0.176\omega_s \sim 0.113\omega_0$, the corresponding growth rate for EAW is $\gamma_{eaw} \approx 0.267\omega_{eaw} \sim 0.107\omega_0$, respectively.

In nonlinear saturation, *as shown in figure 3.5 for the energy density of EM field* $E_y^2 + B_z^2$ *plots*, there is a rapid growth and strong localization of the Stokes EM wave by forming narrow intense EM soliton-like structures with downshifted laser light trapped inside. In the early stage of the T-SEAWS instability, the train of relativistic EM solitons-like gets irradiated through the front vacuum-plasma interface in a form of intense coherent reflection of the downshifted laser light. With time goes on, the large trapped EAW excited in the plasma quickly heats up electrons to relativistic energies, strong electron heating tends to suppress the further growth, eventually the T-SEAWS process will be suppressed by these heated relativistic energetic electrons.

In figure 3.6, the plots for reflectivity of reflected EM wave, are shown. The reflectivity is characterized by a large several peaks due to the radiation of the soliton-like structures. The process of T-SEAWS instability is mainly taken place within 100 laser pulse periods and very large portion of laser energy was reflected.

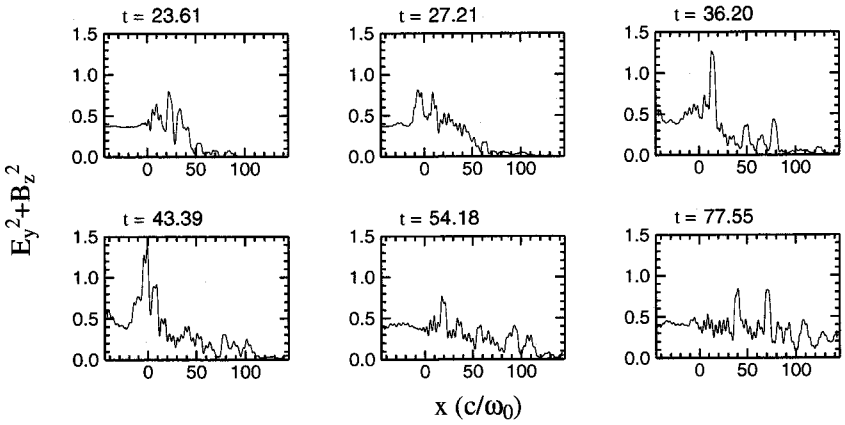

(a). Both electron component and ion component are considered. In the simulation, the mass ratio $M_i/m_e = 1836$ and temperature $T_e = 5T_{ion} = 1.0keV$ are used.

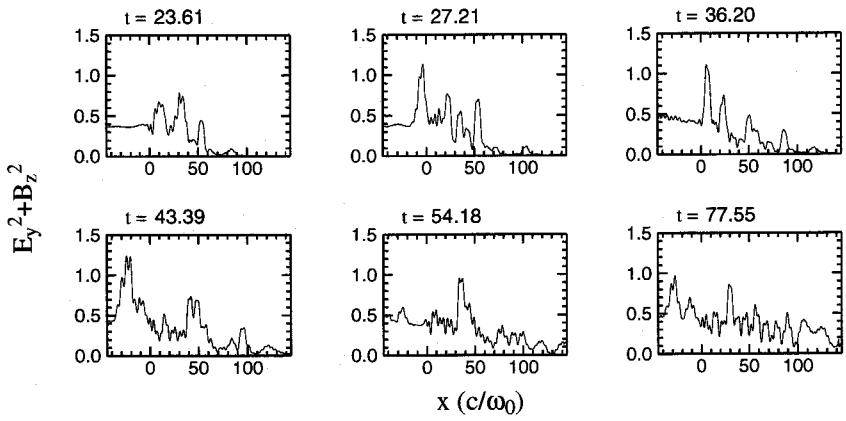

(b). Only electrons are considered. Ions as neutralized background are kept immobile.

Figure 3.5: The snapshots for the energy density of EM field $E_y^2 + B_z^2$ averaged over the laser period in the case of plasma length $L = 100c/\omega_0$, density $n = 0.6n_{cr}$ and laser amplitude $a = 0.6$, respectively.

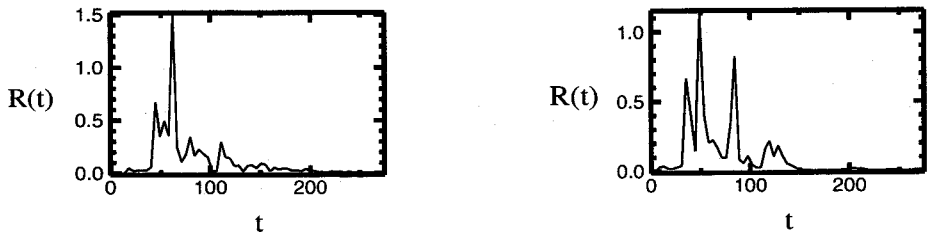

Figure 3.6: The plots for the reflectivity of EM wave. The left plot for both electron and ion components are considered; the right plot for only electron component is considered and ions as neutralized background are kept immobile, respectively.

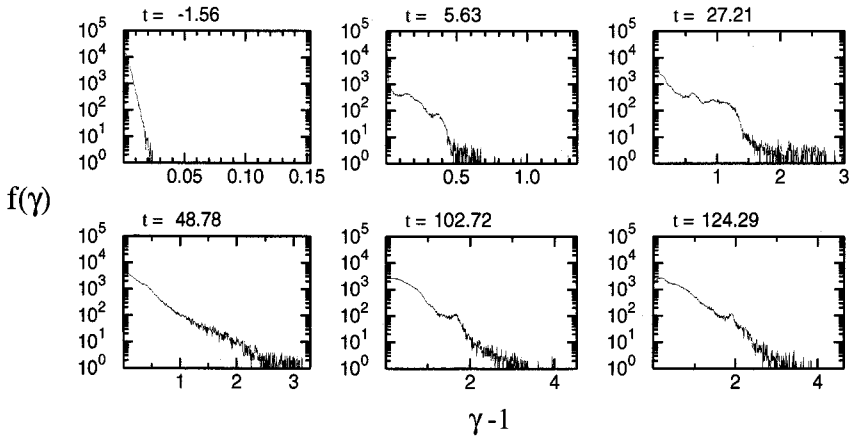

(a). Both electron component and ion component are considered. In the simulation, the mass ratio $M_i/m_e = 1836$ and temperature $T_e = 5T_{ion} = 1.0keV$ are used.

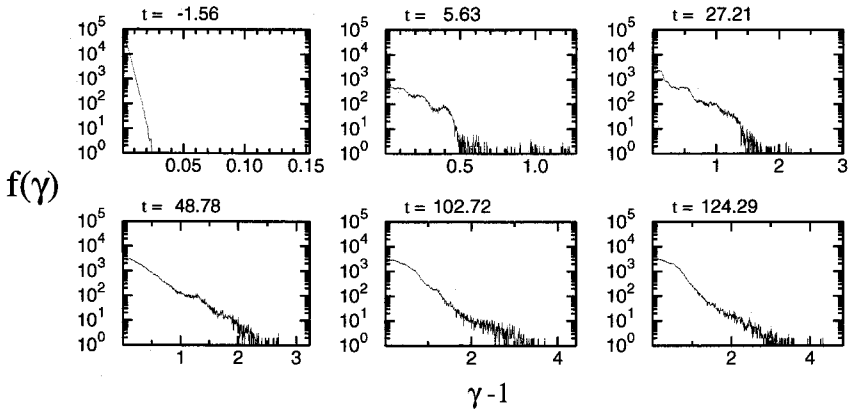

(b). Only electrons are considered. Ions as neutralized background are kept immobile.

Figure 3.7: The energy distribution $f(\gamma) - \gamma$ snapshots in the case of plasma length $L = 100c/\omega_0$, density $n = 0.6n_{cr}$ and laser amplitude $a = 0.6$, respectively.

As shown in figure 3.7, the energy distribution $f(\gamma) - \gamma$ snapshots, the strong trapped EAW heats up some electrons up to the energy about $3MeV$. A confirmation of strong electron heating is also coming from figure 3.8, *where the longitudinal distribution function $f(v_x/c)$ is plotted for different time.* As we can see, the T-SEAWS instability is so strong that can destroy the bulk of an initial Maxwellian electron distribution and produce a relativistic far-from Maxwellian distribution, namely, the "waterbag-like" distribution.

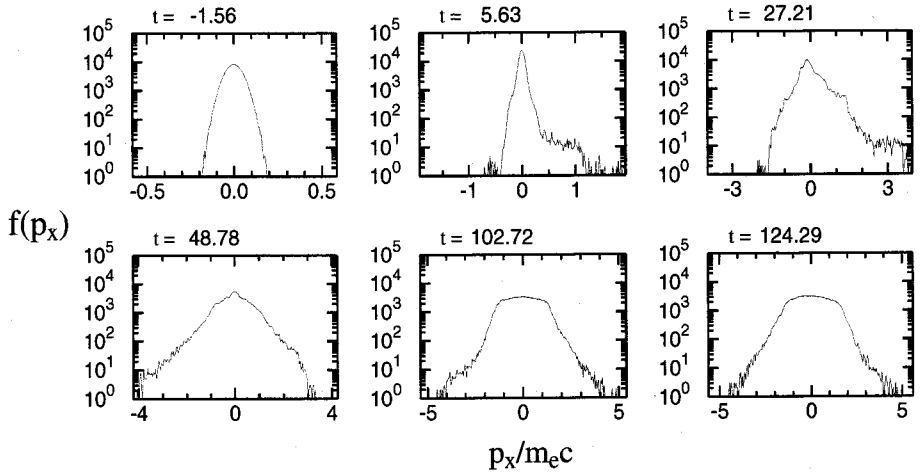

(a). Both electron component and ion component are considered. In the simulation, the mass ratio $M_i/m_e = 1836$ and temperature $T_e = 5T_{ion} = 1.0keV$ are used.

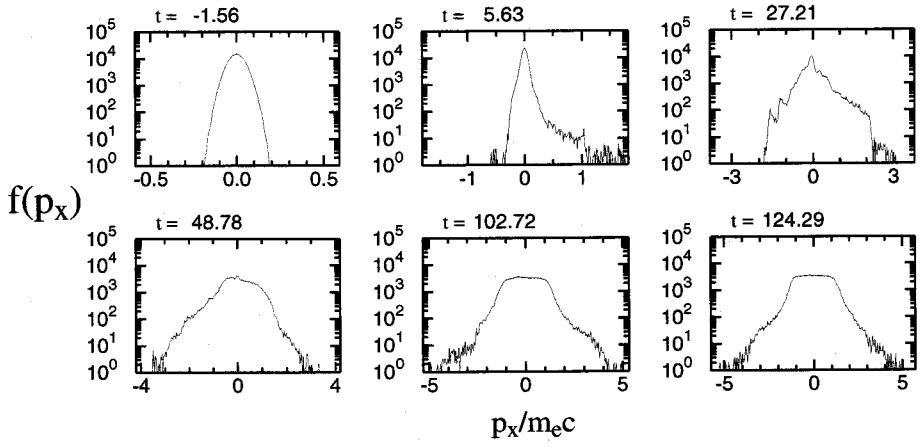

(b). Only electrons are considered. Ions as neutralized background are kept immobile.

Figure 3.8: The longitudinal distribution function $v_x - f(v_x)$ snapshots in the case of plasma length $L = 100c/\omega_0$, density $n = 0.6n_{cr}$ and laser amplitude $a = 0.6$, respectively.

In order to clarify the growth of such T-SEAWS instability, we discuss a simple model for parametric coupling between three waves $a_i(x,t)exp[i(k_i x - \omega_i t)]$, satisfying the frequency and wave number resonant matching conditions, which for weakly varying envelopes [112, 113] in dimensionless units [114, 115] reads.

$$\frac{\partial a_0}{\partial t} + V_0 \frac{\partial a_0}{\partial x} = -M_0 a_s a_{eaw} \tag{3.2}$$

$$\frac{\partial a_s}{\partial t} - V_s \frac{\partial a_s}{\partial x} = M_s a_0^* a_{eaw} \tag{3.3}$$

$$\frac{\partial a_{eaw}}{\partial t} + V_{eaw} \frac{\partial a_{eaw}}{\partial x} + \Gamma_{eaw} a_{eaw} = M_{eaw} a_0^* a_s \tag{3.4}$$

where $V_i > 0$ is the group velocity ($i = 0, s, eaw$ denoting pump EM, backscattered EM and EAW waves), Γ_{eaw} is the damping rate for EAW, the damping rates for pump and backscattered EM waves $\Gamma_0 = \Gamma_s = 0$ are used. $M_i > 0$ are the coupling coefficients and a_i are the wave amplitudes. With standard open boundary conditions $a_0(0,t) = E_0$ and $a_s(L,t) = a_{eaw}(0,t) = 0$, the backscattering grows as an absolute instability, only if $L/L_0 > \pi/2$, where $L_0 = (V_s V_{eaw})^{1/2}/\gamma_0$ is the interaction length and $\gamma_0 = E_0(M_s M_{eaw})^{1/2}$ is the uniform growth rate [112, 113].

As we have stated before, the group velocity of the backscattered EM wave is $V_s = c^2 k_s/\omega_s \approx 0.19c$, even that we assume the group velocity for EAW is so large that $V_{eaw} \approx c$ and a very small uniform growth rate $\gamma_0 \approx 0.1\omega_0$ (the growth rates for both backscattered EM wave and EAW are greater than $0.1\omega_0$ as have shown before), then the $L_0 \approx 4.3c/\omega_0$. For the plasma length $L = 100c/\omega_0$ we used, so the the condition $L/L_0 > \pi/2$ which for the instability taking place, is readily satisfied, that means this new type of T-SEAWS instability can take place in our simulation conditions.

In all above figures, as have been noted, we have plotted all the corresponding figures what the ion dynamics are not considered. These figures are almost the same as what the ion dynamics are considered ones. Therefore, one can say that, the T-SEAWS instability can appear and its physics behavior in early stage are almost the same whether the ion dynamics is taken into account or not.

However, from the plots in figure 3.1(a) the frequency of ES wave $\omega_{ion}^{es} \approx 0.023\omega_0$ and the plots for ion phase-space snapshots in figure 3.3 (a), the ion ES wave is excited in the meantime. If the ion dynamics are considered in our simulations, in addition to the excitation of ion ES wave, what kind of new physics phenomena will show us? The answer will be given in the following sections.

3.3 Large amplitude EM soliton and ion-vortices in homogeneous plasmas

When ion dynamics are considered, in addition to T-SEAWS, an ion ES wave is also excited at early stage and still exists with time. One can see this clearly from figure 3.9, *the phase-space plots for ion component.* However its peak in the spectrum is hard to discern in the early stage due to this ion ES wave is suppressed by strong TEAW. When the T-SEAWS instability finished, *as in the figure 3.1, the frequency spectra of ES wave inside plasma, shown us*, an ion ES wave with frequency $\omega_{ion}^{es} \approx 0.023\omega_0$, which approximately equals to natural ion plasma wave frequency $\omega_{pi} \approx (m_e\gamma/m_i)^{1/2}\omega_{pe} \approx 0.021\omega_0$, can be observed clearly, where $\gamma = (1+a^2)^{1/2}$ is relativistic factor. Like trapped EAW, ion ES wave will eventually be suppressed, because of plasma heating and particle acceleration.

The ion ES wave will propagate inside plasma forward after its excitation. As time goes on, at the time about $t \approx 21.82$, *as shown in figure 3.9(a), the phase-space plots for ion component*, this ion ES wave breaks at the position of nearly $x = 40c/\omega_0$. After this ion ES wave breaking, *as shown in figure 3.9(b), the energy density of EM field snapshots*, one relativistic EM soliton begins to emerge at the same position. This new formed EM soliton then grows with time and saturates at $t \approx 251.94$ with its maximum energy density of EM field $E_y^2 + B_z^2 \approx 2.5$ without changing its position. During its growing, large part of electrons and ions inside the EM soliton region are pushed away from the high EM field region by the large ponderomotive force of this high EM field. Therefore, in the meantime, plasma density cavities both for electrons and ions are created, *as shown in figure 3.9(c) the electron density and ion density snapshots, respectively.* At the rear edge of soliton $x \approx 40c/\omega_0$, *as in figure 3.9(c), the ion density plots at* $t = 214.18$, *shown us*, because of the large ion inertia, ions pile up and one sharp ion density peak then formed. At the front edge of soliton, there are no ion density peak to form, perhaps, this is because the most of ions are accelerated forward by ion ES breaking, or at the front edge of soliton has lower plasma density than that the rear edge of soliton. As the electron density plot shown, in the same time, electrons does not pile up to form an electron density peak at the front and rear edges of soliton due to its small inertia. Therefore, at a narrow region around the soliton rear edge $x \approx 40/\omega_0$, a net positive charge region then forms, *as shown in figure 3.9(d) the left one for the* $(n_i - n_e)/n_0$ *plots.* Behind the ion density peak, i.e., inside the EM soliton region, in order to keep the electrical neutralization, more electrons will be accelerated to close the ion density peak region by the electric field of charge separation (Coulomb force), as a result, there will form a net negative charge region. This charge distribution can result in an ES field structure *as shown in figure 3.9(d), the right plot one for ES field* E_x *plots.* Both the large amplitude EM soliton and the formed E_x can interplay each other and they can together accelerate

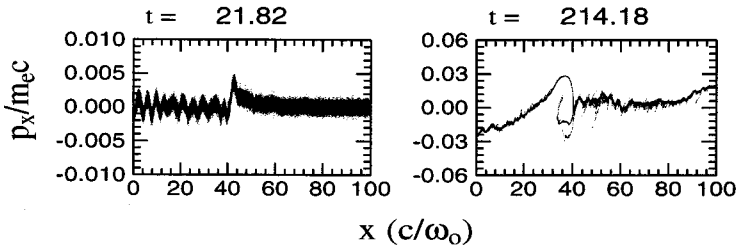

(a). The ion phase-space $x - p_x$ snapshots.

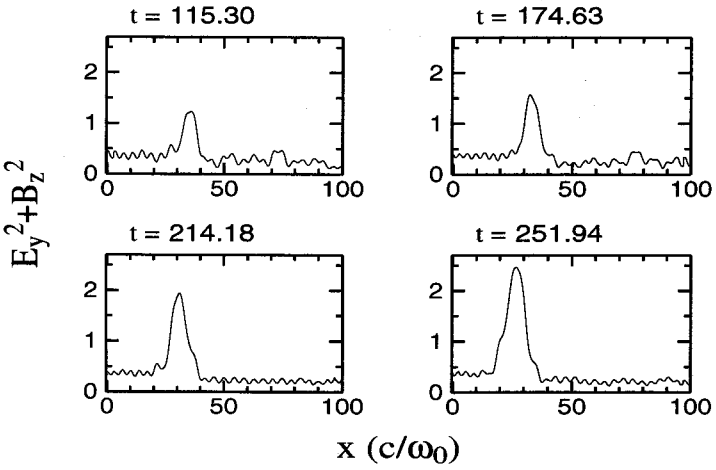

(b). The energy density of EM field $E_y^2 + B_z^2$ snapshots.

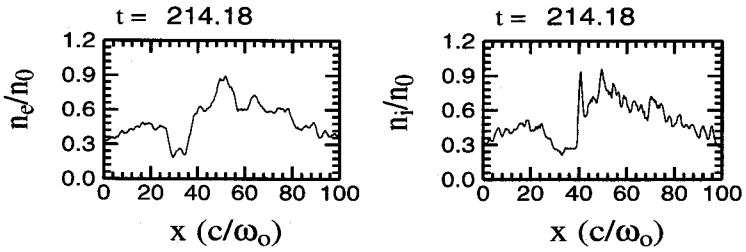

(c). The electron density and ion density snapshots.

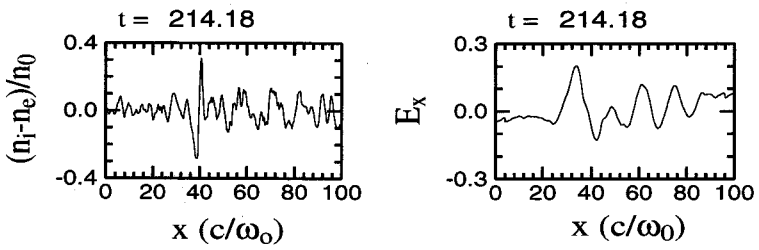

(d). The $(n_i - n_e)/n_0$ and ES field E_x plots.

Figure 3.9: The snapshots for ion phase-space, energy density of EM field averaged over laser period, plasma density and ES field E_x in the case of $L = 100c/\omega_0$, $n = 0.6n_{cr}$ and $a = 0.6$, respectively. In the simulation, both electrons and ions with mass ratio $M_i/m_e = 1836$ and temperatures $T_e = 5T_i = 1.0keV$ are considered.

or decelerate ions. For these ions with negative velocity inside soliton or reflected by right sharp ion density peak, they will first experience a deceleration process, most of these decelerated ions will eventually be stopped in time, after that, they are accelerated again by EM soliton and ES field E_x; while for these ions with positive velocity, they experience just reverse processes. As a result, *as shown in figure 3.9(a), the right one at* $t = 214.18$, eventually, a trapped ion-vortex (ion-hole) structure in phase-space, *which like two-stream instability*, can be formed.

When intense laser pulse enters and passes through plasma layer, with the formation of sheath ES fields at both boundaries, ions will leave from boundaries with time, electrons then follows ions in order to keep electrical neutralization. As a result, the plasma density decreases from the middle part to front and rear boundaries gradually with time. In this formed inhomogeneous plasma, the saturated EM soliton will be accelerated with an acceleration proportional to the gradient of plasma density towards the low density side [62, 74]. When soliton reaches plasma-vacuum interface, it radiates away its energy in the form of short burst EM radiation. By some other simulations, it is found that, this kind of large amplitude relativistic EM soliton often appears in the front region of plasma layer which side laser pulse enters, and it eventually accelerated backward to the plasma-vacuum boundary.

As large amplitude EM soliton propagates in the plasma-vacuum boundary, by large amplitude EM field and large charge separation inside the soliton region, the energy exchange between ions and soliton takes place in the meantime. Since large part of ions then gain energy from EM soliton continuously, they are accelerated and trapped inside soliton region. Because of the continuous energy exchange among the kinetic energy of the accelerated and trapped ions, the EM soliton accelerates backward towards plasma-vacuum interface. In the path of soliton acceleration, *as shown in figure 3.10(a) the energy density of EM field snapshots and in figure 3.10(b) the phase-space snapshots for ion-component*, several ion-vortices (ion-holes) then successively form and persist with time. On the other hand, by continuous energy exchange with ions, EM soliton will lose the large part of its EM energy to ions and its EM amplitude become weaker and weaker. After the soliton arrives at plasma-vacuum boundary or disappears in bulk plasma, the corresponding ion acceleration and trapping then finish, therefore, the formation of new ion-vortex will stop. After that, these formed ion-vortices in phase-space will blur and become hard to see with time. Eventually, they will disappear in bulk plasma due to the plasma heating and other complex nonlinear processes.

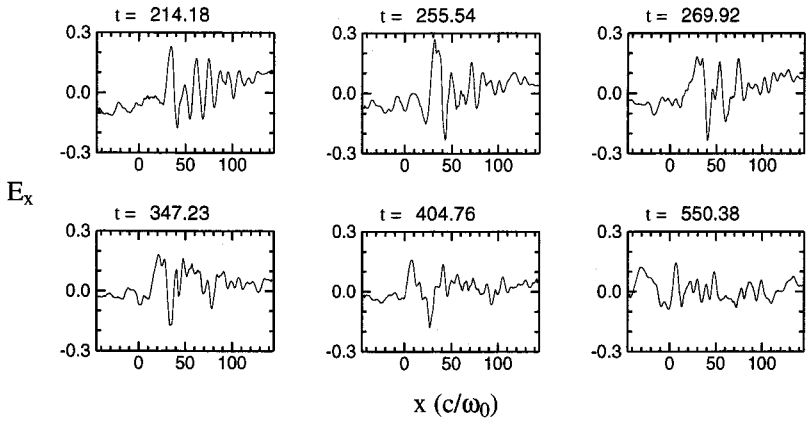

(a). The electrostatic field E_x snapshots.

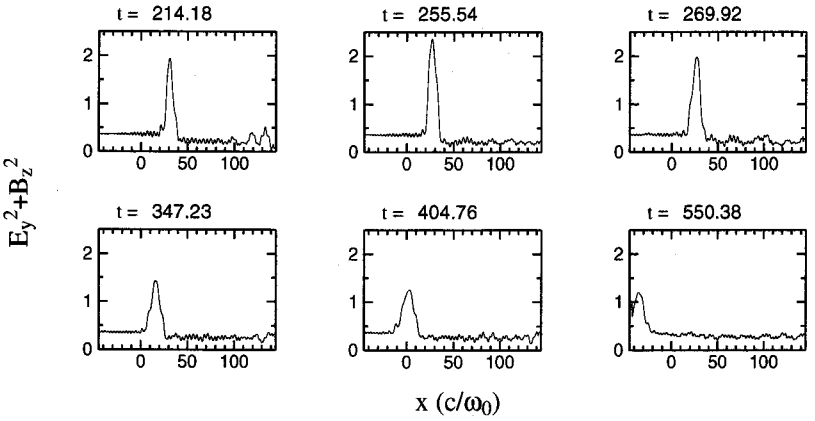

(b). The energy density of EM field $E_y^2 + B_z^2$ snapshots.

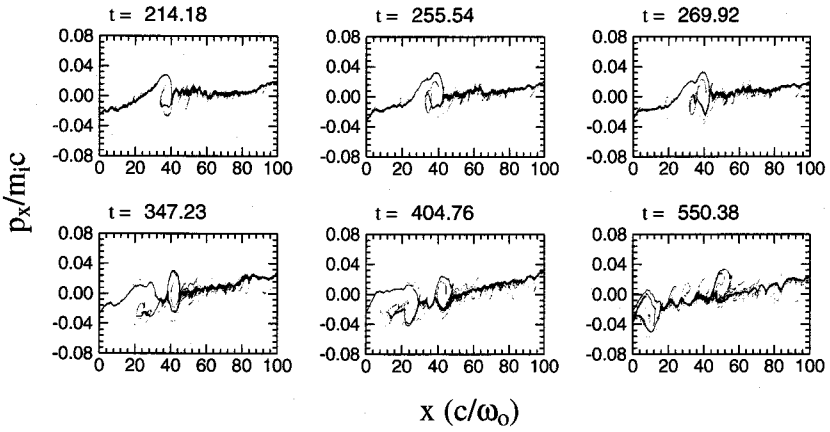

(c). The ion phase-space $x - p_x$ snapshots.

Figure 3.10: The snapshots for ES field, energy density of EM field averaged over laser period and ion phase-space, in the case of $L = 100c/\omega_0$, $n = 0.6n_{cr}$ and $a = 0.6$, respectively. In the simulation, both electrons and ions with mass ratio $M_i/m_e = 1836$ and temperatures $T_e = 5T_i = 1.0keV$ are considered.

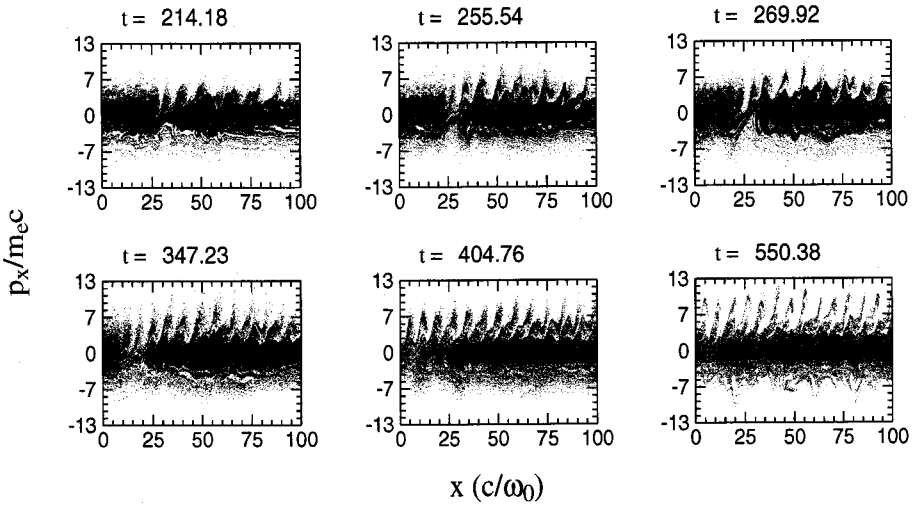

Figure 3.11: The snapshots for electron phase-space in the case of $L = 100c/\omega_0$, $n = 0.6n_{cr}$ and $a = 0.6$, respectively. In the simulation, both electrons and ions with mass ratio $M_i/m_e = 1836$ and temperatures $T_e = 5T_i = 1.0keV$ are considered.

In figure 3.11, the phase-space snapshots for electron component is also given. We can see that, during the formation of ion-vortices, for electrons inside soliton region, by obtaining energy from soliton, they are also accelerated and trapped like what the ions did. However, due to small electron mass, they will soon merge into bulk electron component, therefore, there is no clear electron-vortices to form in electron phase-space.

Figure 3.12 shows the EM field structure of the large amplitude EM soliton (averaged over laser wavelength λ_0), its transverse electric field E_y is the half-cycle structure, while the corresponding magnetic field B_z is the one-cycle structure, respectively. The spatial EM structure of the EM soliton is oscillatory in time. The explanation comes directly from Maxwell's equations. The Faraday law gives $B_z \sim \partial E_y/\partial x$; indeed, the x-derivative of the Gaussian soliton profile E_y gives B_z in figure 3.12.

The size of ion-vortices Δx_{vortex} approximately equals to the size of EM soliton $\Delta x_{soliton}$. From figure 3.12, one can measure the size of EM soliton, it is about $\Delta x_{soliton} = \Delta x_{vortex} \approx 1 \sim 2\lambda_{pe}$, where $\lambda_{pe} = 2\pi c/\omega_{pe}$ is the wavelength of electron plasma wave.

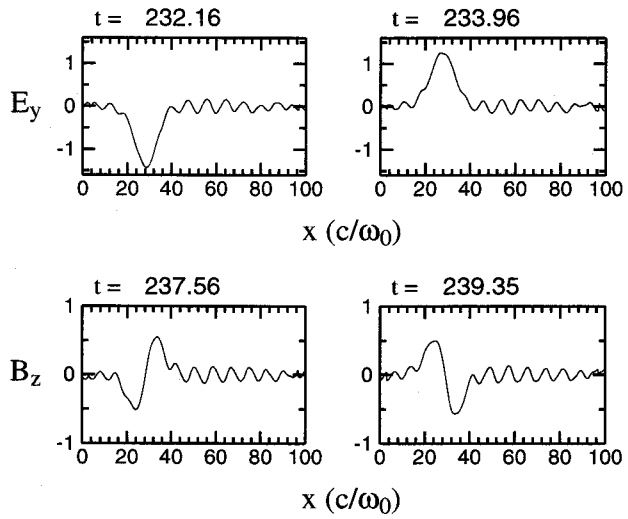

Figure 3.12: The EM field snapshots for electric field E_y and magnetic field B_z both are average over laser period, in the case of $L = 100c/\omega_0$, $n = 0.6n_{cr}$ and $a = 0.6$, respectively. In the simulation, both electrons and ions with mass ratio $M_i/m_e = 1836$ and temperatures $T_e = 5T_i = 1.0keV$ are considered.

Some other simulations are also performed in order to investigate the above physics processes. We found that, when plasma density $n > 0.25n_{cr}$, which are overdense for standard SRS, by choosing appropriate laser amplitude and taking account into the ion dynamics, the T-SEAWS instability, the formation of one large amplitude backward-accelerated relativistic EM soliton and the consequent ion-vortices can often be observed.

They have the same scenarios as the case we have stated before. From now on, we will neglect all the discussion on the T-SEAWS, the generation of EM soliton and the formation of ion-vortices by EM soliton. Here another two simulation results are given, the first simulation is performed in the case of plasma length $L = 100c/\omega_0$, density $n = 0.4n_{cr}$, mass ratio of ion to electron $M_i/m_e = 1836$ and temperatures $T_e = 5T_{ion} = 1keV$ and laser amplitude $a = 0.6$; the second simulation is done in the case of plasma length $L = 100c/\omega_0$, density $n = 0.7n_{cr}$, mass ratio of ion to electron $M_i/m_e = 1836$ and temperatures $T_e = 5T_{ion} = 1keV$ and laser amplitude $a = 0.8$, respectively. The corresponding energy density of EM field and phase-space for ion-component snapshots are plotted in figure 3.13 and figure 3.14, respectively. From the two simulation results, the generation of large amplitude relativistic EM soliton and the formation of ion-vortex structures in phase space by EM soliton are also observed.

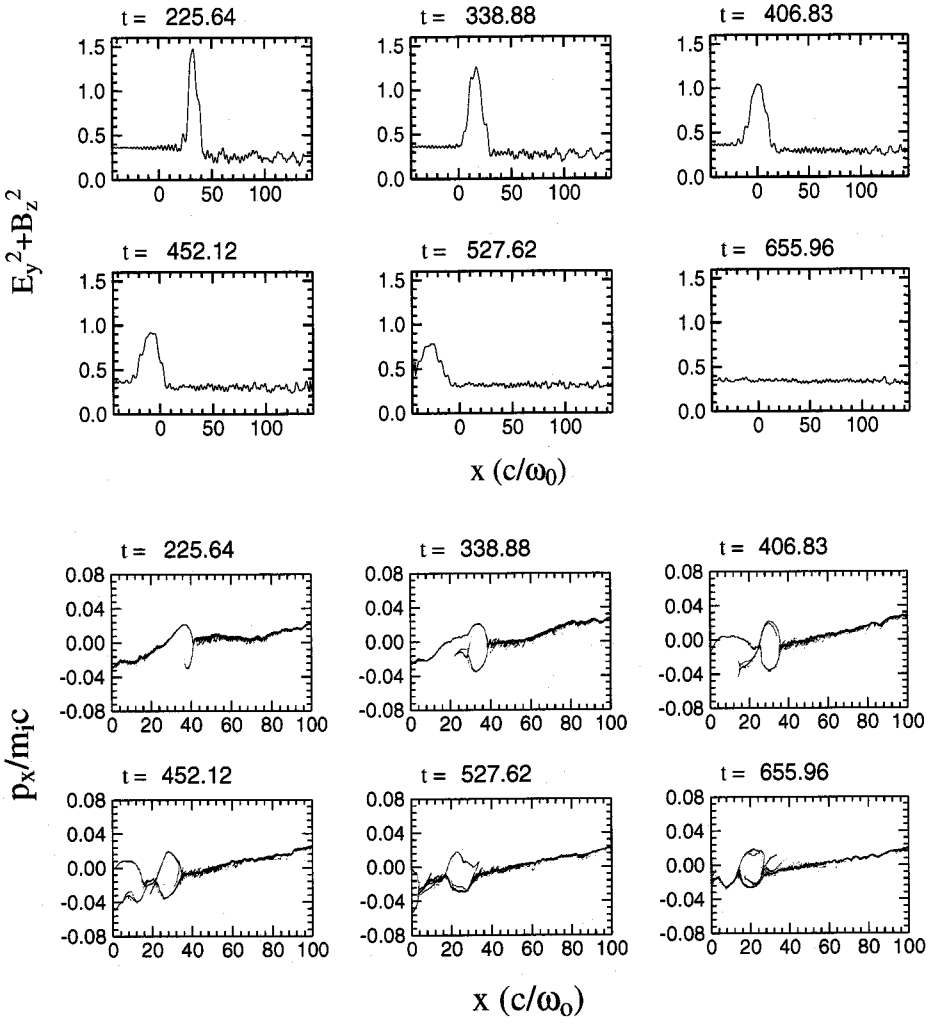

Figure 3.13: The snapshots for energy density of EM field averaged over laser period and ion phase-space in the case of $L = 100c/\omega_0$, $n = 0.4n_{cr}$ and $a = 0.6$, respectively. In the simulation, both electrons and ions with mass ratio $M_i/m_e = 1836$ and temperatures $T_e = 5T_i = 1.0keV$ are considered.

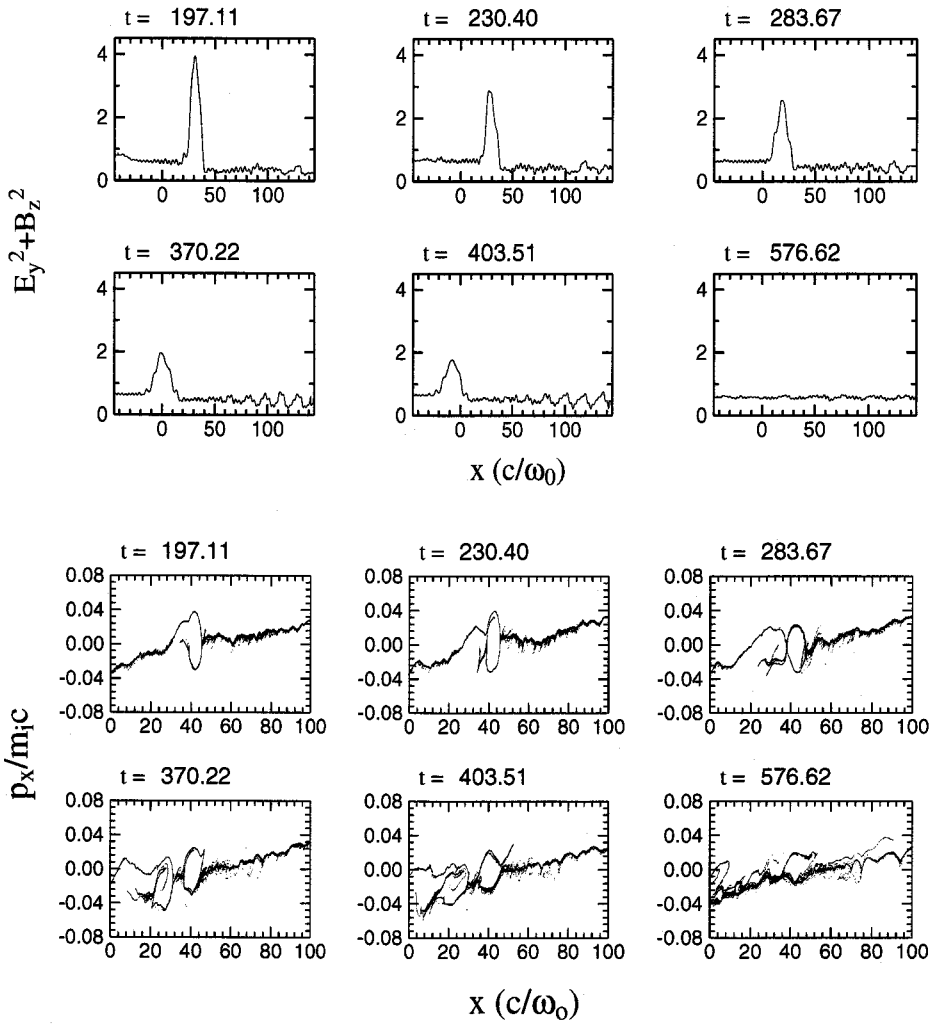

Figure 3.14: The snapshots for energy density of EM field averaged over laser period and ion phase-space in the case of $L = 100c/\omega_0$, $n = 0.7n_{cr}$ and $a = 0.8$, respectively. In the simulation, both electrons and ions with mass ratio $M_i/m_e = 1836$ and temperatures $T_e = 5T_i = 1.0keV$ are considered.

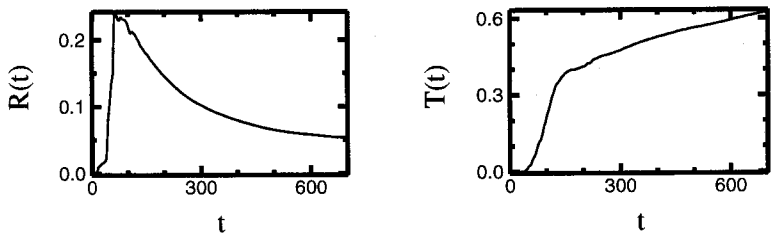

(a). In the case of $n = 0.6n_{cr}$ and $a = 0.6$

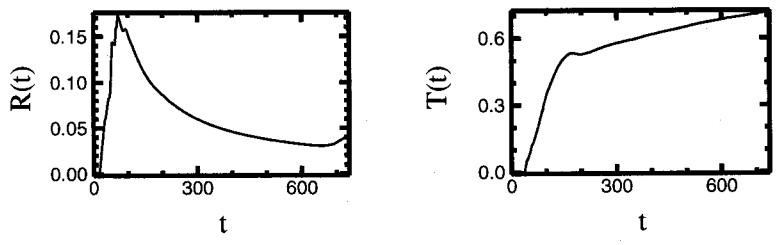

(b). In the case of $n = 0.4n_{cr}$ and $a = 0.6$

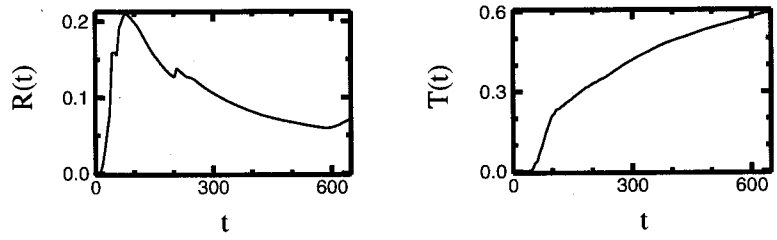

(c). In the case of $n = 0.7n_{cr}$ and $a = 0.8$

Figure 3.15: The reflectivity and transmissivity in the case of $L = 100c/\omega_0$ and $T_e = 5T_i = 1.0keV$, respectively. In simulations, both electrons and ions with mass ratio $M_i/m_e = 1836$ and temperatures $T_e = 5T_i = 1.0keV$ are used.

In figure 3.15, we plotted the time-integrated reflectivities and transmissivities of EM waves for the above three simulation models. It is should note here, that, in the case of $n = 0.6n_{cr}$ and $a = 0.6$, there is only about 55% of laser pulse energy transmits within 500 laser periods while propagating through the $100c/\omega_0$ thick uniform plasma layer. In the case of $n = 0.4n_{cr}$ and $a = 0.6$, about 65% of laser pulse energy, and in the case of $n = 0.7n_{cr}$ and $a = 0.8$, about 60% of laser pulse energy are transmitted while propagating through $100c/\omega_0$ thick uniform plasma layer within 500 laser periods, respectively. In the above three cases, large part of laser pulse energy, about 40% of total laser pulse energy, are reflected and absorbed by plasma layer.

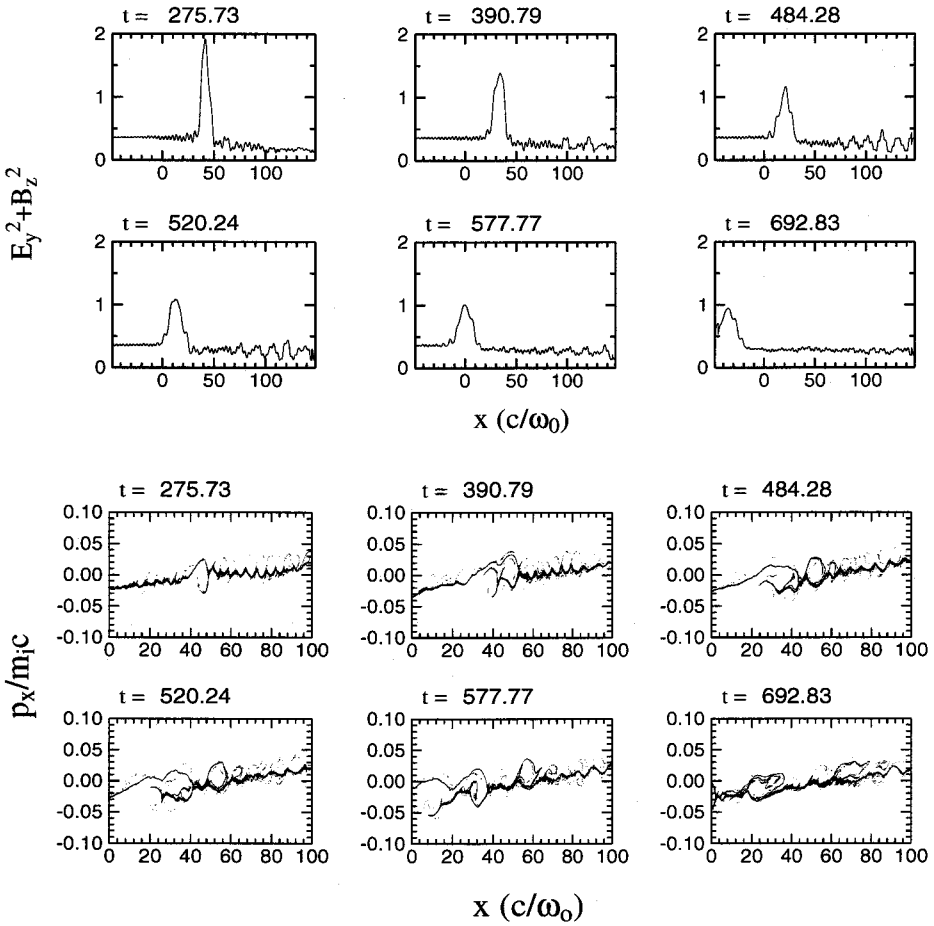

Figure 3.16: The energy density of EM field $E_y^2 + B_z^2$ averaged over laser period and ion phase-space $x - p_x$ snapshots. Plasma length is $L = 100c/\omega_0$ and density increases linearly from $n = 0.3n_{cr}$ to $0.9n_{cr}$, electron and ion temperatures are $T_e = 5T_{ion} = 1keV$ with mass ratio $M_i/m_e = 1836$ and laser amplitude is $a = 0.6$, respectively.

3.4 Large amplitude EM soliton and ion-vortices in inhomogeneous plasmas

All the simulations showed before are performed in homogeneous plasma condition, in fact, not only in the interaction between intense laser EM wave and subcritical homogeneous plasmas, by our some other simulations, in the interaction between intense laser EM wave and subcritical inhomogeneous plasma layers, the T-SEAWS process, the generation of large amplitude relativistic EM soliton and the consequent formation of ion-vortices in phase-space are also be observed.

Two simulations have been performed in inhomogeneous plasma conditions. In the

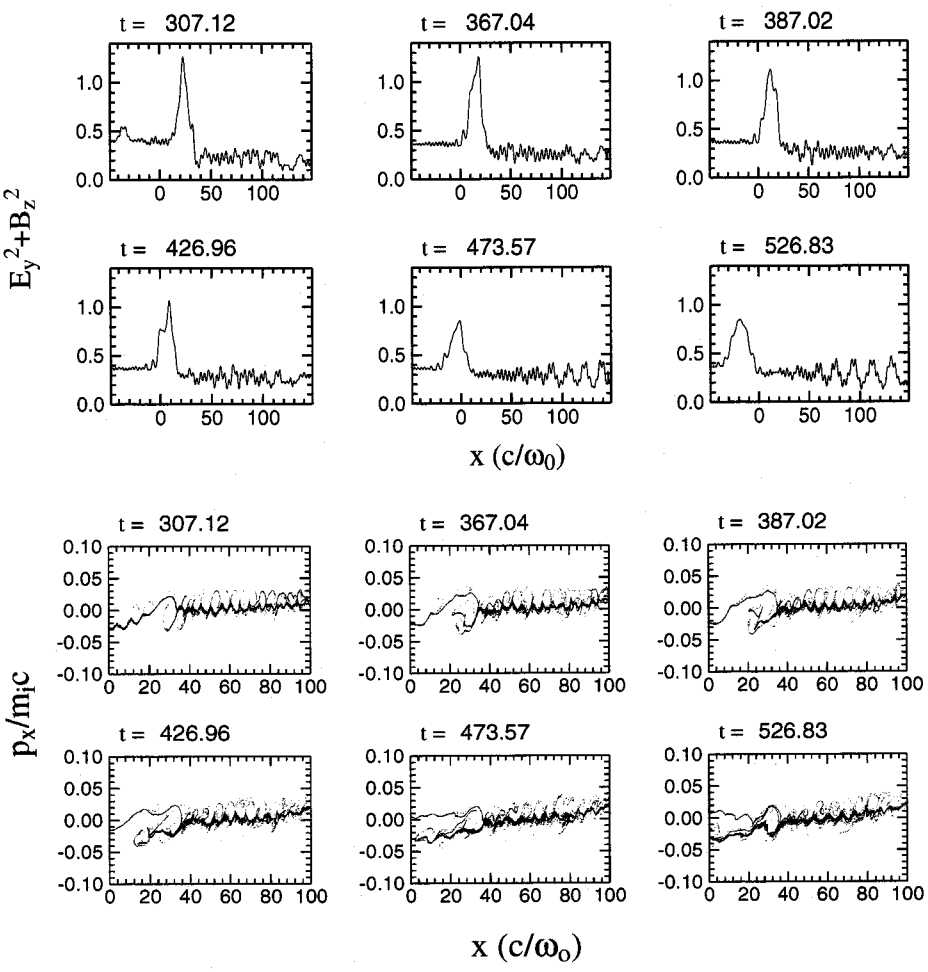

Figure 3.17: The energy density of EM field $E_y^2 + B_z^2$ averaged over laser period and ion phase-space $x - p_x$ snapshots. The plasma length is $L = 100c/\omega_0$ and density increases linearly from $n = 0.35n_{cr}$ to $1.05n_{cr}$, electron and ion temperatures are $T_e = 5T_{ion} = 1keV$ with mass ratio $M_i/m_e = 1836$ and laser amplitude is $a = 0.6$, respectively.

first simulation, plasma density is taken from $n = 0.3n_{cr}$ to $0.9n_{cr}$, while, in the second simulation, plasma density is taken from $n = 0.35n_{cr}$ to $1.05n_{cr}$, the laser amplitude is $a = 0.6$ for the two simulations. The other simulation parameters are the same as used before, for example, the mass ration of ion to electron is $M_i/m_e = 1836$ and the temperatures are $T_e = 5T_{ion} = 1keV$, etc. Here, only the energy density of EM field $E_y^2 + B_z^2$ snapshots and the phase-space $x - p_x$ snapshots for ion-component are given in figure 3.16 and figure 3.17, respectively. From the two simulation results, the same scenarios as observed in homogeneous plasma conditions, i.e., the generation of large amplitude EM soliton and the consequent formation of ion-vortices in ion phase-space are also observed in inhomogeneous plasmas.

(a). The pattern of the Rayleigh-Taylor (R-T) instability

(b). The pattern of the Kelvin-Helmholtz (K-H) instability.

(c). The Ying-Yang pattern of the K-H instability.

Figure 3.18: The patterns of the R-T and K-H instabilities.

3.5 Kelvin-Helmoholtz ion-vortices in phase-space

From the topological point of view it is remarkable that the flow instabilities and wakes often take on one or another of two basic scroll patterns. The first scroll pattern is epitomized by the Kelvin-Helmholtz (K-H) instability as shown in figure 3.18(a) and the second scroll pattern is epitomized by the Rayleigh-Taylor (R-T) instability as shown in figure 3.18(b) [116]. The conventional perspective presumes that the wake is approximated as a tangential discontinuity, defined as a vortex sheet. The basic physical mechanism for wake production is assumed to be associated with the fact that all real fluids have a finite speed of sound, hence a finite compressibility. Therefore, there can exist domains in every (perhaps slightly) compressible fluid where the system of partial differential equations (PDEs) describing the fluid evolution is hyperbolic. Hyperbolic domains have the feature that they can be associated with topological limit sets upon which the solutions to the PDFs are not unique. Therefore topological discontinuities are admissible in such dynamical systems. Such discontinuities are of two types: shock waves and tangential discontinuities. It is this set of limit points associated with the tangential discontinuities that can be put into correspondence with the two basic instability patterns describe above. In the Kelvin-Helmholtz instability pattern, if the wave pattern describes a curve exhibits double tangency, the pattern is named after Ying-Yang pattern as shown in figure 3.18(c) [116]

From the above point of view, it seems that, for the structure of ion-vortices we observed in our simulations, they can be classified as the Kelvin-Helmholtz instability pattern. More precisely, if we think the formation of ion-vortices in phase-space is due to topological defect, i.e., plasma density cavity in relativistic EM soliton region, the ion-vortex structures should belong to the class of Ying-Yang pattern.

Chapter 4

High-quality and well-collimated return relativistic electron beam

Particle acceleration by high-intensity laser pulse propagating in plasmas has recently become a very attractive research topic after the advent of short-pulse and high-intensity lasers, due to their many potential applications. Up to now, various concepts of laser accelerators in plasma, such as, beat-wave accelerator [78, 79], laser wakefield accelerator [80, 81, 82], electron beam wakefield accelerator [83, 84] and plasma accelerator of photon beams [85, 86], are presently under discussion and investigation as possible approaches to accelerate particles to ultra-high energies.

High-energy particles and/or particle beams with high-quality and high-energy have wide potential applications, for example, in the concept of fast ignition of inertial confinement fusion (FI-ICF) [88], laser induced nuclear reaction [89], radiography and so on. Stochastic heating and acceleration of electrons by two counter-propagating laser pulses are also studied by some authors [90, 91, 92, 93].

Much attention on particle acceleration, induced by high-intensity laser-plasma interaction, has been put by theoretical analysis, particle simulation and experiment in the past years. In our recent works, by means of fully relativistic EM one-dimensional particle-in-cell (1D-PIC) simulations, a new phenomenon of short high-quality and well-collimated return relativistic electron beam with thermal energy spread, in the opposite direction to the laser propagation, by intense laser pulse interacting with an underdense plasma layer is observed [87].

4.1 Laser wakefield acceleration

When an intense laser EM wave enters into and propagates in an underdense plasma, by stimulated backward and forward Raman scattering (B-SRS/F-SRS) and other nonlinear laser-plasma processes, e.g., the ponderomotive force of an intense laser EM field, a large

amplitude electron plasma wave (wakefield) can be excited behind the front of the laser EM pulse. Such a relativistic electron plasma wave (wakefield) can also be generated by a beat-wave scheme which requires two laser beams and a plasma frequency precisely tuned to their frequency difference. This large amplitude plasma wave (EPW) has very high phase velocity close to the group velocity of laser pulse and can be used to accelerate electrons, protons or ions to high energies.

4.2 High-quality and well-collimated return relativistic electron beam

From now on, we will pay our attention to the simulation and observation of the new phenomenon of electron acceleration, i.e., the generation of short high-quality and well-collimated return relativistic electron beam with thermal energy spread in the direction opposite to incident laser propagation, which induced by intense laser pulse interacting with an underdense plasma layer.

4.2.1 Simulation model

One-dimensional fully relativistic EM 1d3v PIC code is used as before. The length of the simulation system is $5L(c/\omega_0)$, where c and ω_0 are the speed and carrier frequency of laser pulse in vacuum, respectively. The plasma length is taken as L, it begins at $x = 2L$ and ends at $x = 3L$. At the front and rear sides of plasma layer, there are two $2L$ long vacuum regions. The number of cells are 10 per 1 c/ω_0, 70 electrons are put in each cell. The ions are initially placed as a neutralizing background and are kept immobile. The plasma density is $n = 0.01n_{cr}$, which means $\omega_0/\omega_{pe} = 10$, where ω_{pe} is the electron plasma frequency, $n_{cr} = \omega_0^2 m_e \epsilon_0/e^2$ is the critical density for laser propagation in a plasma. The plasma temperature is $T_e = 1keV$. The laser pulse is linearly-polarized with the electric field E_0 along y-direction and launched at the position between $x = L$ and $x = 2L$. The normalized amplitude of the incident laser electric field is $a = eE_0/m_e\omega_0 c$, where e and m_e are the electron charge and mass, respectively.

The electrons which are blown-off into vacuum, build a potential barrier that prevents electrons to leave from bulk plasma. For fast escaping electrons as well as for EM waves, two additional numerical damping regions at system ends are used.

The time, electric field and magnetic field are normalized to $2\pi/\omega_0$, $m_e\omega_0 c/e$ and $m_e\omega_0/e$, respectively, and the time is taken zero, $t = 0$, when laser pulse arrives at the front (left) vacuum-plasma boundary.

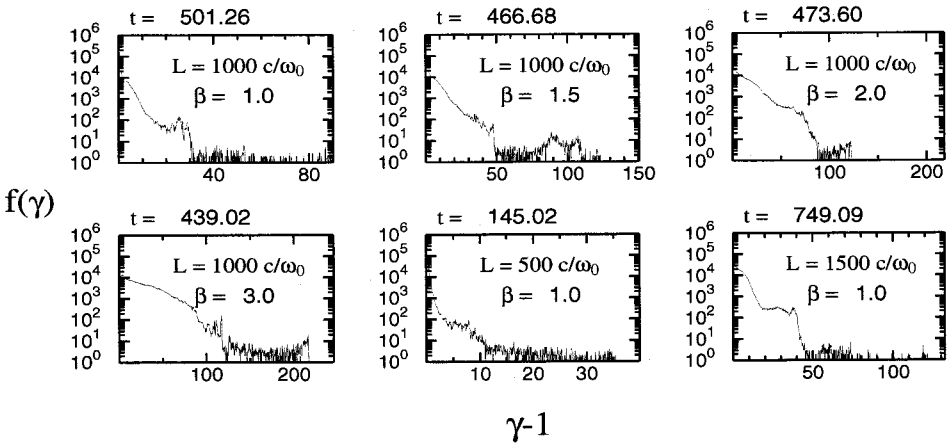

Figure 4.1: The electron energy distribution $f(\gamma) - \gamma$ plots for six simulations in the case of plasma density $n = 0.01 n_{cr}$ and temperature $T_e = 1.0 keV$. The plasma length L and laser amplitude a are inserted in each plot, respectively.

4.2.2 Electron acceleration by stimulated Raman scattering

As has been stated before, when an intense laser EM wave enters and propagates in an underdense plasma, by stimulated Raman scattering (SRS), and other nonlinear processes, e.g., the ponderomotive force of an intense laser EM field, a large amplitude EPW can be excited. The resulting large EPW grows and saturates quickly with time until it reaches the wave-breaking limit, after which, large number of background electrons are self-trapped and accelerated to high energies.

In order to study particle acceleration by an intense laser pulse, as shown in figure 4.1 for the electron energy distribution $f(\gamma) \sim \gamma$ plot, six different simulations have been performed by varying plasma length L and laser amplitude a. Here γ is electron relativistic Lorentz factor. The maximum momentum and energy of an electron after the breaking of large amplitude EPW for different plasma length and laser amplitude are tabulated in Table 4.1.

In the same plasma length $L = 1000c/\omega_0$, for the cases of laser amplitude $a = 1.0$, 1.5, 2.0 and 3.0, the maximum obtained electron momentum goes up to are $p^{max}/m_e c \approx 91$, 151, 219 and 246, corresponding to maximum electron energy: $E^{max} \approx 46$, 77, 112 and 126 MeV, respectively. As a result, the maximum energy of an electron increases with increasing laser amplitude, i.e., $E^{max} \propto a$, approximately.

In addition to the above simulation runs, by changing the plasma length $L = 500$, 1000 and $1500c/\omega_0$, and fixing the laser amplitude to $a = 1.0$ and other plasma parameters, we get the maximum relativistic factor $\gamma^{max} \approx 41$, 91 and 134, with the corresponding maximum electron energy $E^{max} \approx 21$, 47 and $68 MeV$, respectively. A fact is found that, that is, the longer the plasma length, the larger the Lorentz factor.

Table 4.1: Six simulation results for different plasma length L and laser amplitude a. The "I" stands for laser intensity for wavelength $\lambda_0 = 1\mu m$ laser, p^{max} and E^{max} stand for the maximum obtained electron momentum and energy, respectively.

Simulation No.	1	2	3	4	5	6
$L(c/\omega_0)$	1000	1000	1000	1000	500	1500
a	1.0	1.5	2.0	3.0	1.0	1.0
$I(10^{18}W/cm^2)$	1.37	3.09	5.49	12.4	1.37	1.37
p^{max}/m_ec	91	151	219	246	41	134
$E^{max}(MeV)$	46	77	112	126	20	68

An electron interacting with a plane EM wave (laser field) acquires the energy equal to $E_e = m_ec^2a^2/2$, for example, $a = 2.0$, $E_e \approx 1.0MeV$. From this point of view, one cannot expect that energetic electrons obtained in our simulations are directly accelerated by an ultra-intense laser EM field.

The self-modulated regime of laser-plasma interaction is defined by a laser pulse with a normalized vector potential of the order of unity $a = eE_0/m_e\omega_0c \approx 1$, pulse length of several times the electron plasma wave periods and the laser frequency of several times the electron plasma wave frequency. In the one-dimensional limit, the interaction between such intense laser pulses and a low-density plasmas is dominated by the stimulated forward Raman scattering (F-SRS) instability [97, 98, 99]. As shown in the above paragraphs about the stimulated Raman scattering and cascade-into-condensate, F-SRS modulates incident intense laser pulse at the plasma frequency with a corresponding modulation of the plasma density. The resulting large EPW grows quickly with time until it reaches the wave-breaking limit (standard dephasing limit). After that, large number of background electrons are self-trapped by EPW and are accelerated to high energy level. The self-modulated laser wakefield accelerator (SM-LWFA) utilizes this mechanism to generate a beam of highly energetic electrons.

The large amplitude electron plasma waves (EPWs) are generated by a self-modulation or stimulated forward Raman scattering instability with a phase velocity v_p, near the group velocity v_g of the laser pulse, i.e., $v_p \approx v_g$, so the relativistic Lorentz factor corresponding to the phase velocity v_p of EPW is $\gamma_p = (1 - v_p^2/c^2)^{-1/2} \approx (1 - v_g^2/c^2)^{-1/2} \approx \omega_0/\omega_{pe}$. According to Ref. [79], in the two-dimensional cold plasma theory, the critical amplitude of the electron plasma wave (plasmon) is determined by the wave-breaking limit (standard dephasing limit), the maximum energy of an electron, *trapped by the potential of a relativistic EPW, having an amplitude* $e\varphi^{max} \approx \gamma_p m_ec^2$, is given by

$$E^{max} = 2\gamma_p^2 m_e c^2 \tag{4.1}$$

By taking the parameter $\omega_0/\omega_{pe} = 10$ we used, the maximum energy of an electron obtained is $E^{max} \approx 102MeV$.

For the same plasma length $L = 1000c/\omega_0$, in the two cases of laser amplitude $a = 1.0$ and $a = 1.5$, the maximum relativistic factor of an electron obtained are $\gamma^{max} \approx 91$ and 151, the corresponding maximum energy $E^{max} \approx 46$ and $77MeV$, respectively, which are less than $102MeV$; this means that the large amplitude EPWs do not exceed the wave breaking limit (standard dephasing limit). However, for the same plasma length $L = 1000c/\omega_0$, in another two cases of laser amplitude $a = 2.0$ and $a = 3.0$, the maximum relativistic factor of an electron obtained are $\gamma^{max} \approx 219$ and 246, the corresponding maximum energy $E^{max} \approx 112$ and $126MeV$, respectively, the maximum electron energies are exceeding the wave-breaking limit (standard dephasing limit).

In recent years, large efforts have been made to understand why the maximum electron energy can exceed the standard dephasing limit. It was also reported in experiments [100, 101] and studied by PIC simulations [102, 103] that maximum relativistic electron energies observed are in an excess of the standard dephasing limit $E^{max} = 2\gamma_p^2 m_e c^2$. For example, in Ref. [104], by including the space-charge field due to self-channeling, it was shown that the maximum energy gain $E^{max} = 4\gamma_p^2 m_e c^2$, which is greater by a factor of ≥ 2. A new kind of mechanism that leads to efficient acceleration of electrons in underdense plasma by two counter-propagating laser pulses may help to explain how the maximum energy gain can possibly exceed the standard dephasing limit, as suggested by some authors [92, 93].

In this thesis, we do not want to study why the maximum electron energy can exceed the standard dephasing limit and will leave this problem in the next paragraphs. Our goal is to focus on a generation of a pulsed high-quality and well-collimated return relativistic electron beam; and to study the ultra-relativistic beam characteristics, the mechanism of beam formation and the time-history of the beam electrons in phase-space $x - p_x$.

4.2.3 High-quality and well-collimated return relativistic electron beam and two-stage electron acceleration

To show this phenomenon, *in figure 4.2, the electron phase-space $x - p_x$ snapshots* are plotted for four simulation runs, where the incident laser amplitude are $a = 0.5$, 1.0, 2.0 and 3.0. One can see that, besides the laser amplitude $a = 0.5$ case, a short high-quality and well-collimated return relativistic electron beam propagating in the direction opposite to laser propagation is created. We also found that, when laser amplitude between $a = 1.0$ and $a = 2.0$, the quality of the return relativistic electron beam is

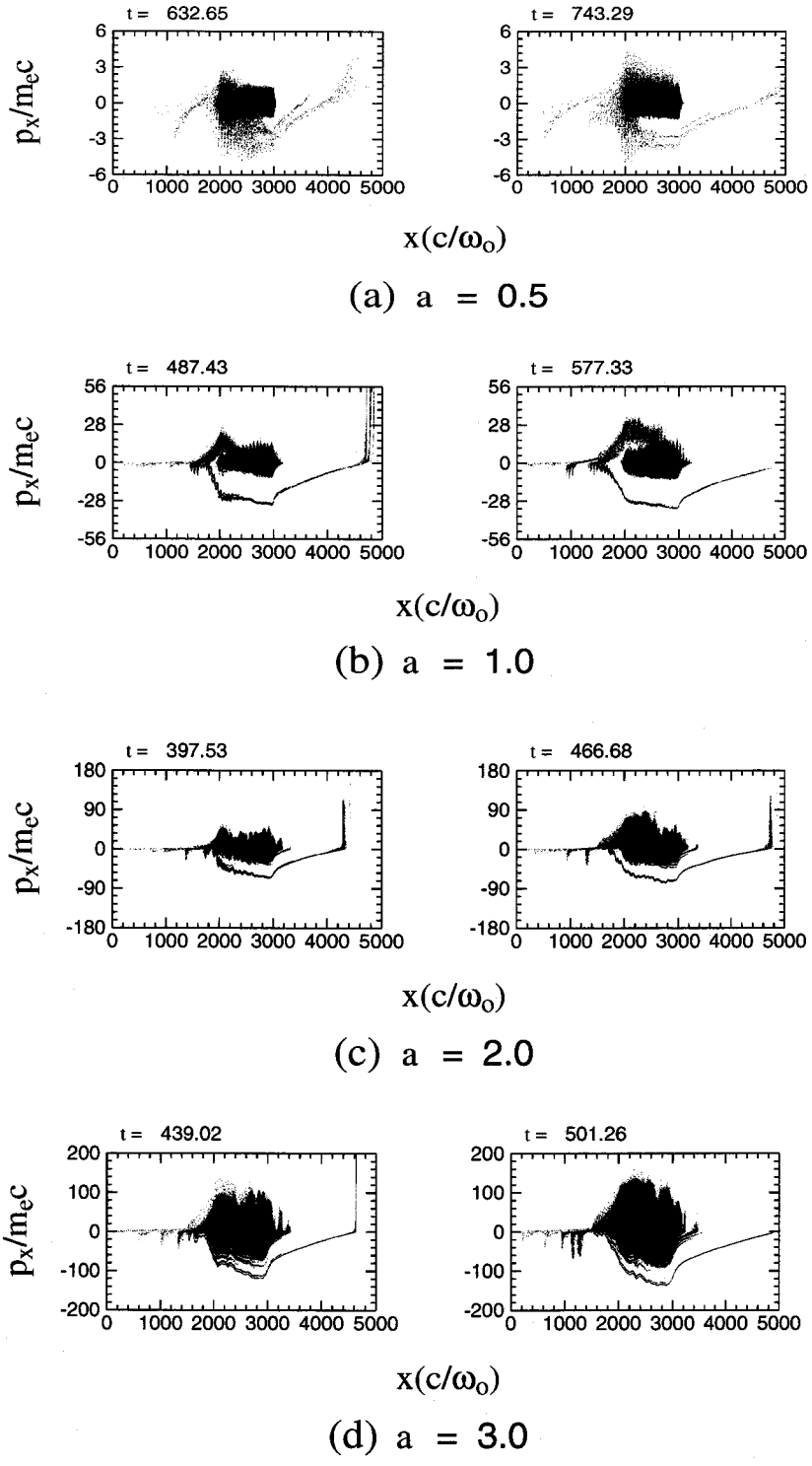

Figure 4.2: The electron phase-space $x - p_x$ snapshots in the case of plasma length $L = 1000c/\omega_0$ and temperature $T_e = 1.0keV$. Four simulations are performed for different laser amplitude (a) $a = 0.5$; (b) $a = 1.0$; (c) $a = 2.0$; and (d) $a = 3.0$, respectively.

better than that of other laser amplitude cases under the condition of our simulation parameters.

As an example, from now on, we will concentrate on the case of plasma length $L = 1000c/\omega_0$ and laser amplitude $a = 1.0$, to study and explain the details of the high-quality and well-collimated return relativistic electron beam.

In figure 4.3, the snapshots for electron longitudinal momentum in phase-space $x - p_x$, is given. Physics of electron acceleration by intense laser interacting with underdense plasma can be seen clearly and directly. At an early stage, large part of the background electrons start to interact with a forward propagating relativistic EPW generated mainly by F-SRS and are accelerated to large positive momenta p_x. As has shown in figure 4.1 and Table 4.1, in this case, the maximum electron momentum and energy obtained are $p_x^{max}/m_e c \approx 91$ and $E^{max} \approx 46MeV$, respectively. The accelerated electrons move forward to the right plasma-vacuum boundary, where they escape from plasma layer into vacuum region to build a potential barrier, *as shown in figure 4.4 for the snapshots of ES field E_x*, a large ES field that is formed quickly. This sheath ES field structure gradually decreases from plasma-vacuum interface to vacuum region. The accelerated electrons entering this region experience deceleration to be eventually stopped. Further, these electrons reverse their motion to be accelerated backwards into the bulk plasma. However, some ultra-fast electrons overcome the potential barrier and eventually are lost in the numerical-damping region, that we introduced.

Electrons travelling backward through the bulk plasma will be additionally accelerated by the ES sheath at the front interface. As time progresses, a mono-energetic well-collimated relativistic electron beam bunch (energy about $12 - 17MeV$ is eventually formed. When these electrons get through the front interface into vacuum, they again experience deceleration and reverse acceleration by the ES sheath potential. Most of the electrons returning into the bulk plasma are moving forward to the rear boundary. However, in the meantime, the high-quality well-collimated relativistic electron beamlet will gradually separate from the rest of the beam. Since the sheath ES field at the plasma-vacuum boundary still exists, electrons which arrive at the rear side experience the similar process as before. Moving back and forth energetic electrons recirculate through the bulk plasma. In time, due to electron beam interaction with the bulk plasma, relativistic beam features will be lost via thermalization with the rest of the heated bulk plasma.

Why at appropriate intense laser amplitude condition, for example, $a = 1 \sim 2$, this kind of high-quality and well-collimated relativistic electron beams can be formed? We think that, perhaps, this result comes from the mutual-modulation between the accelerated electrons and the large sheath ES field formed at right vacuum region. Possibly, at lower laser amplitude condition, because of no strong electron acceleration by SRS and the small sheath ES field formed at right vacuum region which keeps its structure too

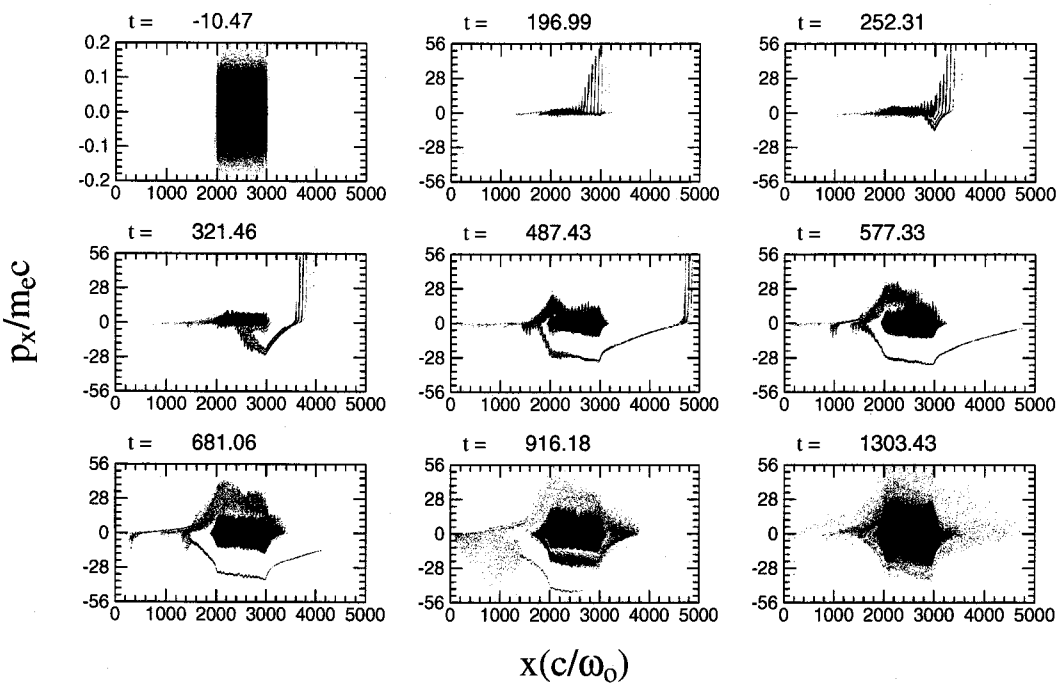

Figure 4.3: The snapshots for electron phase-space $x - p_x$ in the case of plasma length $L = 1000c/\omega_0$, temperature $T_e = 1.0keV$ and laser amplitude $a = 1.0$, respectively.

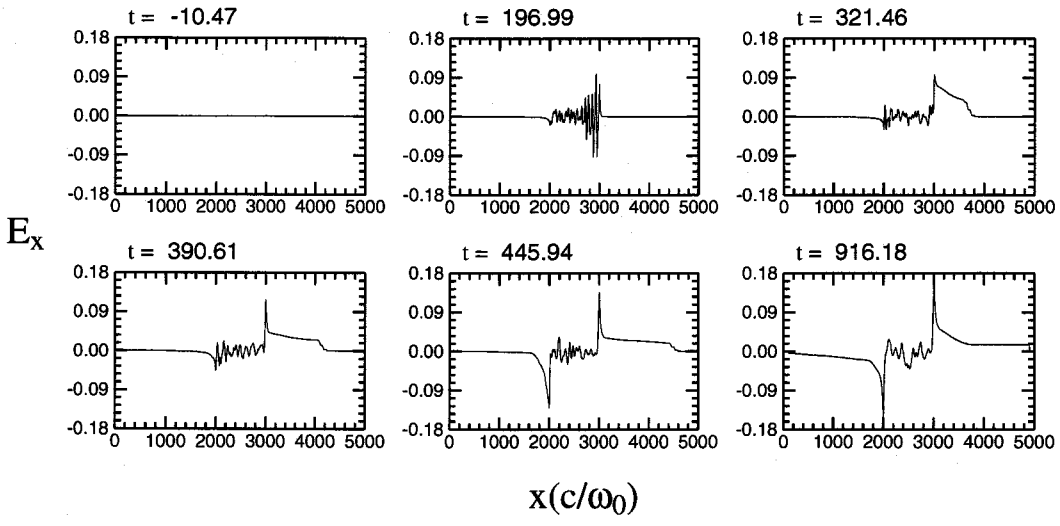

Figure 4.4: The snapshots for electrostatic field E_x in the case of plasma length $L = 1000c/\omega_0$, temperature $T_e = 1.0keV$ and laser amplitude $a = 1.0$, respectively.

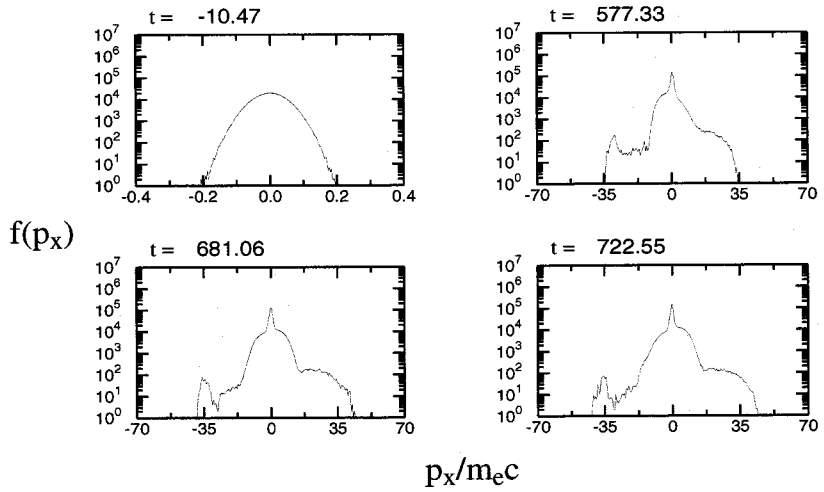

Figure 4.5: The snapshots for electron longitudinal momentum distribution $p_x - f(p_x)$ in the case of plasma length $L = 1000c/\omega_0$, temperature $T_e = 1.0keV$ and laser amplitude $a = 1.0$, respectively.

long time not to be changed, while, at higher laser amplitude condition, strong electron acceleration due to SRS and large sheath ES field with fast-changed structure at right vacuum region; as a result, in the two cases of lower and higher laser amplitudes, the mutual-modulation between the accelerated electrons and the sheath ES field formed right vacuum region are not properly satisfied the condition which for the high-quality and well-collimated relativistic electron beam to form.

In Figure 4.5, the snapshots of electron longitudinal momentum distribution $p_x - f(p_x)$ *is shown.* The peaked distributions can tell us about the formation of the relativistic electron beam and its energy distribution in the opposite direction to the laser propagation. The relativistic electron beam is formed as the accelerated electrons are reflected and pulled into the bulk plasma from the right plasma-vacuum interface. This formation of high-quality and well-collimated return relativistic electron beam is characterized by the peak around the electron longitudinal momentum $p_x/m_ec \approx -35$.

Based on the above simulation results, we propose that, electron acceleration by intense laser EM wave interacting with underdense plasma layer, *plasma density* $n < \gamma n_{cr}/4$ *for SRS taking place*, can be divided two phases, i.e., the initial rapid electron acceleration by F-SRS and the second electron acceleration due to large sheath ES field at right vacuum region. *The electron acceleration in the second phase corresponds to the formation of high-quality and well-collimate return relativistic electron beam.* This two-phase electron acceleration operates just like a two-stage accelerator.

In order to see the process of high-quality and well-collimated relativistic electron

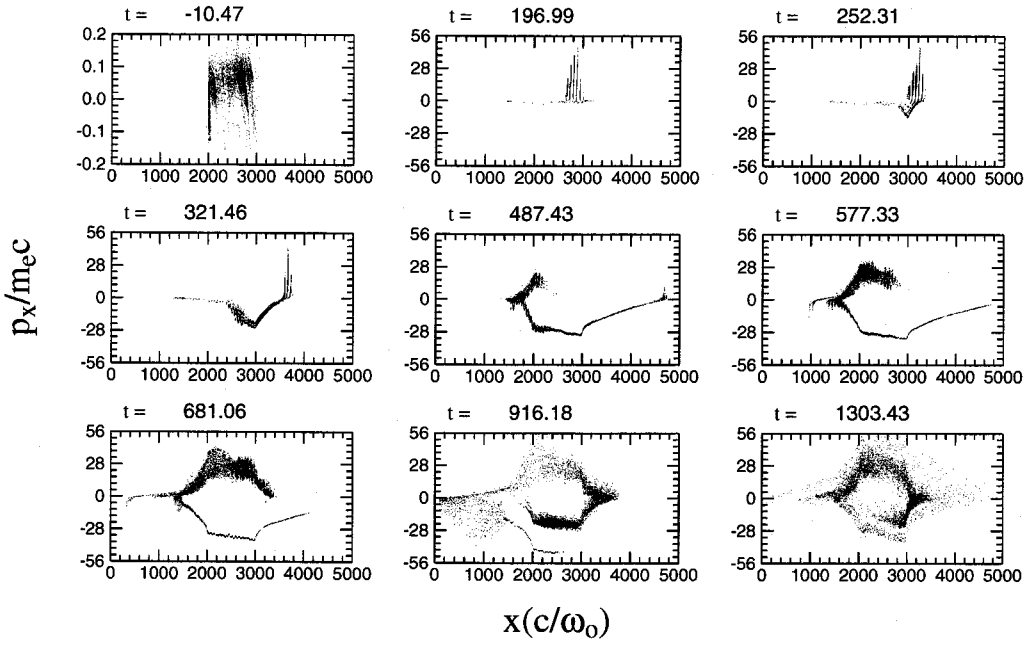

Figure 4.6: The snapshots of electron phase-space $x - p_x$ for these selected electrons which have negative momenta between $-20 \leq p_x/m_ec \leq -90$ during the time interval of $239 \leq t \leq 955$ in the case of plasma length $L = 1000c/\omega_0$, temperature $T_e = 1.0keV$ and laser amplitude $a = 1.0$, respectively.

beam formation clearly, we select test electrons which have negative momenta between $-20 \leq p_x/m_ec \leq -90$ during the time interval of $239 \leq t \leq 955$. The time interval corresponds to the start and the end for this high-quality and well-collimated return relativistic electron beam to form. These two conditions almost include all beam electrons. About 1.3% of the total number of electrons satisfy the two conditions in our simulation. This means that, at least 1.3% of total electrons are accelerated to $\gamma \geq 20$ in the case of laser amplitude $a = 1.0$. These test electrons almost cover the whole range of the accelerated electrons that we discussed above. By introducing test electrons, we can trace back their earlier time history easily and vice versa.

In Figure 4.6, we have plotted the snapshots of longitudinal momentum in phase-space $x - p_x$ for these test electrons. Clear physics pictures for electron acceleration, deceleration, and the formation of high-quality and well-collimated return relativistic electron beam, are shown directly. We can also see that the number of accelerated electrons come from the electrons which have positive initial velocities in an initial Maxwell distribution.

For the plasma length of $L = 1000c/\omega_0$, intense laser pulse propagates in a plasma and arrives at the right plasma-vacuum interface at $t \approx 159$; after that, although the

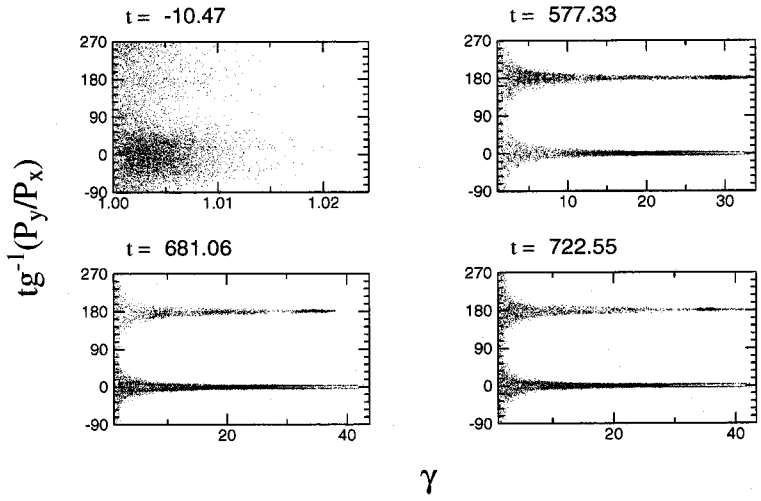

Figure 4.7: The angular-energy distribution snapshots for these selected electrons which have negative momenta between $-20 \leq p_x/m_e c \leq -90$ during the time interval of $239 \leq t \leq 955$ in the case of plasma length $L = 1000c/\omega_0$, temperature $T_e = 1.0keV$ and laser amplitude $a = 1.0$, respectively.

laser pulse still propagates in a plasma, the electron acceleration by large amplitude EPW is almost finished by this time. Nearly all of the forward accelerated electrons are accelerated by the transient electron plasma wave before laser pulse arrives at the right plasma-vacuum boundary.

As in figure 4.7 the angular-energy distribution $\gamma \sim tan^{-1}(p_y/p_x)$ *of test electrons shown*, the initial number of electrons which will be accelerated, which has angular-energy distribution between $-90°$ and $90°$ (moving forward, initially) is greater than that of between $90°$ and $270°$ (moving backward, initially). When these electrons accelerated in time, the electron angular-energy distribution is mostly concentrated around two angles $90°$ and $-270°$, that means,

$$|p_x| \gg |p_y|. \tag{4.2}$$

The accelerated electrons have larger longitudinal momentum p_x than that of transverse momentum p_y, *in other words*, it demonstrates that electrons are accelerated mainly by longitudinal waves, not by transverse waves.

In order to better visualize, electron orbits in space are shown for these accelerated electrons. The time history of orbits $x(t)$ and momentum $p_x(t)$ for six representative test electrons selected from all of the accelerated electrons, are plotted in figure 4.8. The scenarios shown in the figure are consistent with our above discussions.

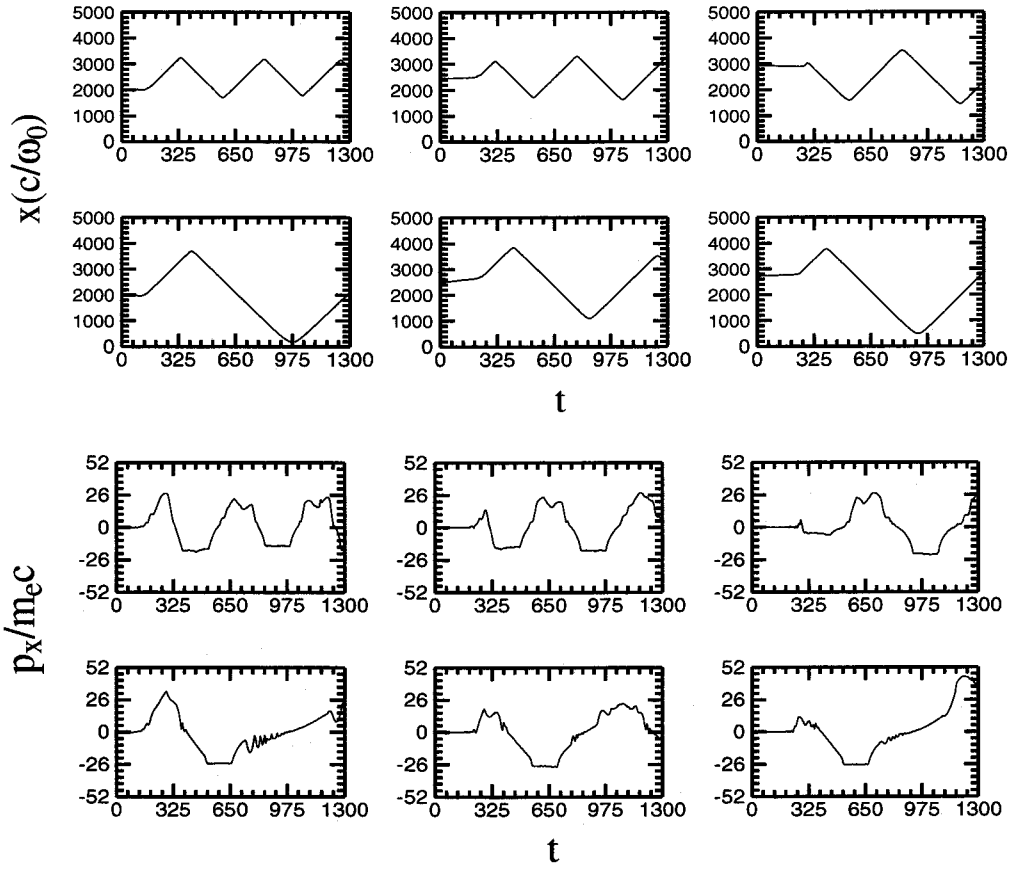

Figure 4.8: The time history of orbits $x(t)$ and momentum $p_x(t)$ for six representative test electrons selected from all of the accelerated electrons in the case of plasma length $L = 1000c/\omega_0$, temperature $T_e = 1.0keV$ and laser amplitude $a = 1.0$, respectively.

When intense laser propagates in the low-density plasma, a large amplitude EPW is generated mainly by SRS [18]. Rapid SRS heating in forward direction produces a massive electron blow-off into vacuum region. The large sheath ES fields build up to drive return currents and accelerate the background electrons to high energies. *As shown in figure 4.4, for the electrostatic field E_x plots*, at time $t = 196.99$ (the laser pulse has passed through the right boundary) SRS driven large amplitude EPW is propagating. At later times, as SRS gradually saturates, an intense narrow sheath ES field structure (Debye sheath) with a steep gradient forms at each plasma interface. The maximum ES field goes up to $E_x^{max} \approx 0.18 m_e \omega_0 c/e$. The electrons get accelerated by this sheath electric field, which spreads over the hot-electron Debye length [105]. Assuming that the electron experiences the Dirac delta-function field, $E(x) \sim \delta(x)$; the maximum electron energy estimate is $E^{max} = \int_0^L e\delta(x)dx = 46MeV$ which well agrees with the result $E^{max} \approx 46MeV$, measured above. This leads to impressive effective accelerating electric fields of the order of few hundreds GV/m.

4.2.4 Influences of ion dynamics and numerical-damping region on electron acceleration

In this section, we will briefly discuss the influences of the ion dynamics and the numerical damping region on the formation of short high-quality and well-collimated return relativistic electron beam.

In our simulations, the plasma density is taken as $n = 0.01n_{cr}$, i.e., the ratio of the laser to the plasma frequency $\omega_0/\omega_{pe} = 10$, that is, the electron plasma period $T_p = 10T_0$, where T_0 is laser pulse period. As known, due to large ion inertia $M_i = 1836m_e$, the ion plasma frequency is only about $\omega_{ion} = (m_e/M_i)^{1/2}\omega_{pe} \approx \omega_{pe}/43$, the corresponding ion plasma period $T_{ion} \approx 43T_p = 430T_0$, i.e., 430 times the laser pulse period. Our total simulation time is about $t_{simu} \approx 1300T_0 \approx 3T_{ion}$. The high-quality and well-collimated return relativistic electron beam has been already formed before the time of $900T_0$. Therefore, it seems plausible to neglect the ion dynamics. Our additional PIC runs, *as shown in figure 4.9, both the electron phase-space $x - p_x$ snapshots (top) and the electrostatic field E_x snapshots (bottom)*, has proved that above assertion is correct.

In order to study the influence of numerical-damping region, another simulation has been performed for long vacuum regions both in front and rear side of plasma layer by increasing the vacuum region from $2L = 2000c/\omega_0$ to $3L = 3000c/\omega_0$, the other simulation parameters are the same as before, i.e., in the case of plasma length $L = 1000c/\omega_0$, temperature $T_e = 1000eV$ and laser amplitude $a = 1.0$, etc. By this new simulation results, *as shown in figure 4.10, both the electron phase-space $x-p_x$ snapshots (top) and the electrostatic field E_x snapshots (bottom)*, we can say that the numerical-damping region which we introduced does not have influence on the formation of high-quality and well-collimated return relativistic electron beam. In fact from figure 4.3 and figure 4.10, one can clearly see during the formation of this electron beam, for these electrons which overcome the sheath ES field enter numerical-damping region, they have no enough time to come back to the region of plasma vacuum interface, i.e., the region of large sheath ES field, so we need not worry these electrons come back to influence the formation of this high-quality and well-collimated return relativistic electron beam.

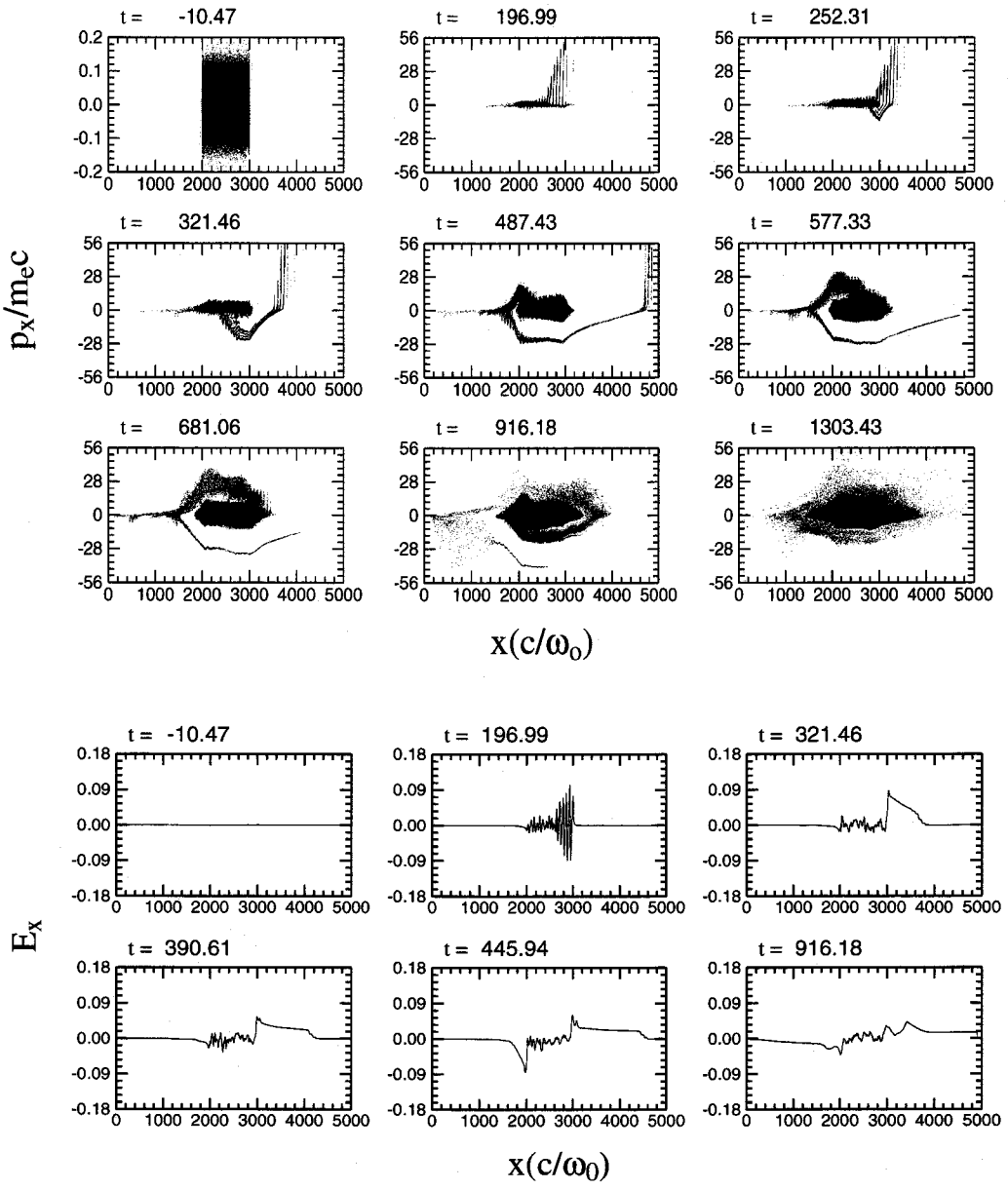

Figure 4.9: The electron phase-space $x - p_x$ and electrostatic field E_x snapshots in the case of plasma length $L = 1000c/\omega_0$ and laser amplitude $a = 1.0$. In this simulation, ion dynamics is considered with the mass ratio of electron to ion is taken as $M_i/m_e = 1836$ and temperature $T_i = T_e/2 = 500eV$, respectively.

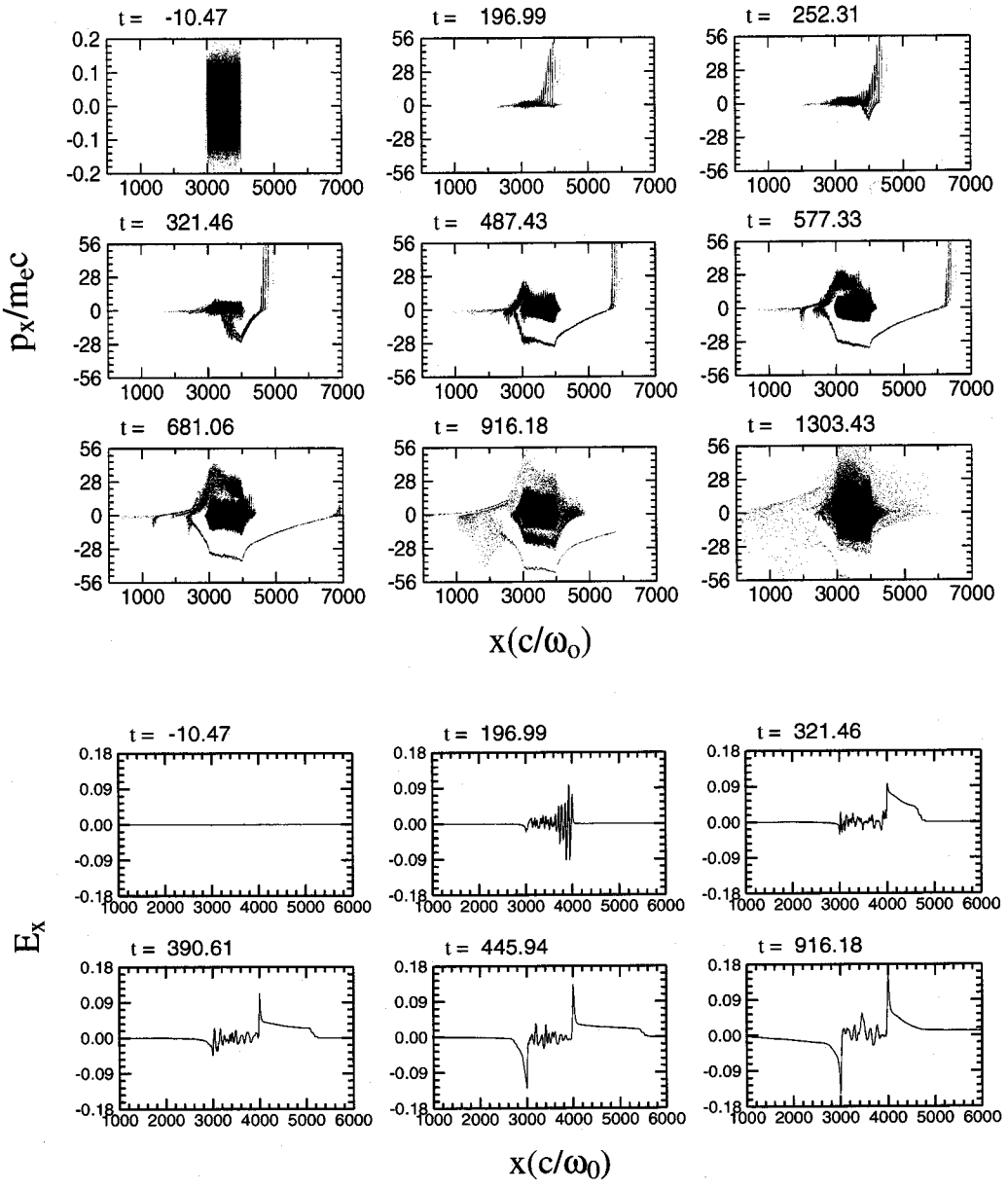

Figure 4.10: The electron phase-space $x - p_x$ and electrostatic field E_x snapshots in the case of plasma length $L = 1000c/\omega_0$, temperature $T_e = 1.0keV$ and laser amplitude $a = 1.0$. In this simulation, the vacuum regions used for both left side and right side are $3000c/\omega_0$, which is longer than that used in above simulations $2000c/\omega_0$.

Chapter 5

Conclusions and Summary

The interaction between ultra-intense laser EM waves and plasmas now is a basic and important topic due to the rich physical phenomena both in wave-wave and wave-particle interaction and its widespread applications ranging from astrophysics to fusion science.

ICF, as an attractive energy source, has become one of the most challenging goals in current energy research, which motivates many scientists to pay more attentions to the research of laser-plasma interactions. Laser-plasma interaction is a source of various instabilities, and the study of instabilities is of an essential importance for the success of ICF. In particular, the most of researches have been put into the studies of SRS and SBS, concerning their ability to reflect laser energy and produce energetic particles that can preheat the core of a fusion pellet in laser fusion applications, which reduce the energy gain of laser-fusion targets. Recently, SEAWS instability was proposed in experiment and was also studied by particle simulation. Although much effort has been devoted to this subject, many aspects of scattering instabilities remain unresolved and observations and theoretical models are rarely in good agreement. In addition to the various instabilities, ultra-intense laser pulse propagating in a plasma, dispersion effects come into play due to the finite inertia with which plasma particles respond to the high laser EM field, while the nonlinearity appears due to the plasma density redistribution under the action of the ponderomotive force that pushes the plasma particles away from the region of maximum EM field. These effects can lead to well-known nonlinear phenomena such as self-focusing, transparency of an overdense plasma, and the generation of EM soliton. After the advent of short-pulse, high-intensity laser pulse, particle acceleration by intense laser interacting with plasma has also become a very attractive research topic due to its widespread applications, such as photon acceleration, in the concept of fast ignition of ICF, medical treatment, radiography and so on.

In the thesis, our researches are mainly concentrated on instabilities, relativistic EM soliton and electron acceleration, induced by linearly-polarized intense laser interacting with underdense plasmas, by means of fully relativistic EM 1D-PIC simulations.

(1). The first part is the generation of accelerated large amplitude relativistic EM solitons in long underdense homogeneous plasma

In simulations, ions are initially placed as a neutralizing background and are kept immobile. In the case of low plasma density $n = 0.032 n_{cr}$, the physical phenomena take place according to the temporal series as follows.

1.1. SRS takes place, which can be described as a resonant decay of an incident laser EM wave (ω_0, k_0) into a scattered EM wave (ω_s, k_s) plus an EPW (ω_{epw}, k_{epw}), with following matching condition for frequencies and wavenumbers are well-satisfied;

$$\omega_0 \approx \omega_s + \omega_{epw} \quad ; \quad k_0 \approx \mp k_s + k_{epw} \tag{5.1}$$

1.2. After B-SRS and F-SRS, there is typically the stimulated Raman cascade process with the following dominant frequencies and wave numbers,

$$\omega_{s,j} = \omega_0 \pm j\omega_{epw} \quad ; \quad \mp k_{s,j} = k_0 \pm j k_{epw} \quad (j = \pm 1, \pm 2, \pm 3, ...) \tag{5.2}$$

The scattered EM waves include not only the Stokes modes ($j = -1, -2, \cdots$) but also the anti-Stokes modes ($j = 1, 2, \cdots$), respectively.

1.3. After Raman cascade, the transition from Raman cascade into photon condensation takes place. It becomes more pronounced with increasing laser intensity. It downshifts the power maximum from the fundamental to the bottom of EM wave spectra, i.e., the EM energy accumulation at perturbed electron plasma frequency ω_{pe}.

1.4. The standing, backward- and forward-accelerated large amplitude relativistic EM solitons are observed after the photon condensation process. As a new research result, we found that, in homogeneous plasma condition, the acceleration of soliton depends not only upon the incident laser intensity but also upon the plasma length. The accelerated solitons arrive at the plasma-vacuum interface, where radiating their energy in the form of low-frequency intense EM bursts. In the region of soliton, the transverse electric, magnetic and ES fields have half-, one- and one-cycle structure in space, respectively. Only from the point of view of frequency, this phenomenon can be roughly explained as a three-wave resonant coupling process.

(2). The second part is the generation of ion-vortices in phase-space in subcritical density plasmas ($\mathbf{n_{cr}/4 < n/\gamma < n_c}$, γ is relativistic factor).

2.1. When laser enters the plasma layer, a novel T-SEAWS instability takes place. It can be well-explained by a resonant 3-wave parametric decay of the relativistic laser pump into the slowed Stokes EM wave with $\omega_s \sim \omega_{pe}$ and the T-EAW with $\omega_{eaw} < \omega_{pe}$, with following matching condition for frequencies and wavenumbers are well-satisfied;

$$\omega_0 \approx \omega_s + \omega_{eaw} \quad ; \quad k_0 \approx -k_s + k_{eaw} \tag{5.3}$$

In nonlinear saturation, there is a rapid growth and strong localization of the Stokes wave by forming narrow intense EM soliton-like structures with downshifted laser light

trapped inside. The train of soliton-like structures gets irradiated through the front vacuum-plasma boundary. Large trapped EAW quickly heats up electrons to relativistic energies which eventually suppresses the T-SEAWS instability. The ion dynamics does not play a significant role on the early physics behaviors of T-SEAWS.

2.2. When ion dynamics are considered, an ion ES wave is excited. As time goes on, ion ES wave breaks, accompanying with the generation of a large amplitude EM soliton in its breaking place, and therefore the formation of large ES field inside.

2.3. As a new physics phenomenon, an ion-vortex in phase-space forms because the large part of ions are accelerated and trapped by the regular EM and ES fields inside large amplitude soliton. As the soliton accelerating backwards, several ion-vortices form due to the continuing ion acceleration and trapping. Not only in homogeneous but also in inhomogeneous plasma at subcritical density, at appropriate laser amplitude, the ion-vortices can form due to the large amplitude EM soliton.

2.4. From the topological point of view, the ion-vortex structure can be classified as the Kelvin-Helmholtz instability pattern. More precisely, if we think the formation of ion-vortices is due to topological defect, i.e., plasma density cavity in the region of soliton, the ion-vortex structure should belong to the class of Ying-Yang pattern.

(3). In the third part of this thesis, the formation of high-quality and well-collimated return relativistic electron beam is studied.

3.1. When an intense laser propagates in a long underdense homogeneous plasma, an EPW can be excited by SRS and the resulting EPW grows and saturates quickly with time until it reaches the wave-breaking limit. Large number of background electrons are trapped and accelerated to high energies due to the breaking of the large EPW;

3.2. The novel point is that, at appropriate laser intensities, a new phenomenon of pushed short high-quality and well-collimated return relativistic electron beam, is observed in the direction opposite to laser propagation;

3.3. Based on our research result, we propose that, electron acceleration by intense laser interacting with underdense plasma, can be divided two phases, i.e., the initial rapid electron acceleration by SRS and the followed electron acceleration due to large sheath ES field at right vacuum region which corresponds to the formation of high-quality and well-collimated return relativistic electron beam. This two-phase electron acceleration operates like a two-stage accelerator.

Although the above results presented in this thesis are based on 1D geometry, they can serve as useful background to investigate multi-dimensional plasma complexity in the further research on parametric instabilities, nonlinear phenomena and particle acceleration, etc., which induced by ultraintense laser EM waves interacting with underdense plasmas.

Abbreviations

EM: Electromagnetic

ES: Electrostatic

ICF: Inertial confinement fusion

PIC: Particle-in-cell

1D-PIC: One-dimensional particle-in-cell

EPW: Electron plasma wave

IAW: Ion acoustic wave

SRS: Stimulated Raman scattering

SBS: Stimulated Brillouin scattering

B-SRS: Stimulated backward Raman scattering

F-SRS: Stimulated forward Raman scattering

RMI: Relativistic modulational instability

EAW: Electron acoustic wave

T-EAW: Trapped electron acoustic wave

SEAWS: Stimulated electron acoustic wave scattering

T-SEAWS: Stimulated trapped electron acoustic wave scattering

MHD: Magneto-hydro-dynamics

Acknowledgments

I would like to express my gratitude to Professor Seiji Ishiguro for his great patient and elaborate guidance based on his remarkable understanding in the complex of laser-plasma interaction. I have received many benefits from every discussion with him in this three-year PhD course life.

I also wish to extend my thanks to Professor Tetsuya Sato for his providing me with an opportunity to study in Theory and Computer Simulation Center (TCSC) of National Institute for Fusion Science (NIFS), Japan.

I owe special thanks to Prof. M. M. Škorić. In my past three-year studies, he helped me understand the physics of laser-plasma interaction, I have received many helpful knowledge from every discussions with him.

I am greatly indebted to Dr. H. Takamamu for providing the 1D-PIC code for the EM simulation, helping me understand the physics of laser-plasma interaction, and giving many helps on computation and scientific visualization.

I owe special thanks to Prof. R. Horiuchi, Prof. K. Mima, Prof. T. Hayashi, Prof. M. Okamoto, Dr. Y. Tomita and Dr. S. Todo for their guidances, supports, encouragements and many helpful discussions.

My thanks are also extended to Dr. T. Watanabe, Dr. H. Miura, Dr. H. Nakamura, Dr. S. Goto, Dr. A. Takayama, Dr. H. Ohtani, Dr. N. Mizuguchi, Dr. A. Ishizawa, Mr. K. Matsuura, Ms. K. Shimazaki, Ms. S. Urushihara and my Japanese teacher Mr. N. Hayashi for their kind helps in my research and life in Japan.

I am indebted to all other members of Theory and Computer Simulation Center of National Institute for Fusion Science (NIFS) for their helps in my staying in Japan.

I would to express my gratitude to Fusion Science Association, Japan, for the Research Student Scholarship and for the opportunity to live and study in Japan.

My appreciation is extended to Professor He Xiantu, Professor Zhu Shaoping, Professor Pei Wenbing and Professor Li Jinghong in Institute of Applied Physics and Computational Mathematics, for their constant encouragements and supports.

Finally, I would like to thank my family, especially for my mother Liu Wanzhen, for their encouragement and constant mental supports.

Bibliography

[1] William L. Kruer, *The physics of Laser Plasma Interactions*, Addisson-Wesley, California, 1987

[2] T. Yamanaka, *Overview of laser fusion research in Asia*, in Proceedings of the Inertial fusion sciences and applications 2001, edited by K. A. Tanaka, D. D. Meyerhofer and J. Mayer-ter-Vehn, (Elsevier, 2002), p.3.

[3] M. H. R. Hutchinson, *High power laser applications in the EU*, in Proceedings of the Inertial fusion sciences and applications 2001, edited by K. A. Tanaka, D. D. Meyerhofer and J. Mayer-ter-Vehn, (Elsevier, 2002), p.22.

[4] C. B. Tarter, *Inertial fusion and high-energy-density science in the United States*, in Proceedings of the Inertial fusion sciences and applications 2001, edited by K. A. Tanaka, D. D. Meyerhofer and J. Mayer-ter-Vehn, (Elsevier, 2002), p. 9.

[5] D. S. Montgomery, B. B. Afeyan, et al., Phys. Plasmas **5**, 1973 (1998).

[6] J. C. Fernández, J. A. Cobble, et al., Phys. Plasmas **7**, 3743 (2000).

[7] H. X. Vu, D. F. DuBois and B. Bezzerides, Phys. Rev. Lett. **86**, 4306 (2001).

[8] H. X. Vu, D. F. DuBois and B. Bezzerides, Phys. Plasmas **9**, 1745 (2002).

[9] Ljubomir Nikolić, *Complexity in a Relativistic Wave-Plasma Interaction*, Doctor of Philosophy, Department of Fusion Science, School of Mathematical and Physical Science, The Graduated University for Advanced Studies, 2002

[10] M. N. Rosenbluth and R. Z. Sagdeev, Eds., *Handbook of Plasma Physics, Volume 3: Physics of Laser Plasmas*, A. M. Rubenchik and S. Witkowski, Eds. (Elsevier Science Publishers, B. V., 1991), Chapter 9 and references therein

[11] F. Ze, L. J. Suter, et al., Comments Plasma Phys. and Controlled Thermonuclear Fusion **10**, 33 (1986).

[12] D. S. Montgomery, R. J. Focia, et al., Phys. Rev. Lett. **87**, 155001 (2001)

[13] D. S. Montgomery, J. A. Cobble, et al., Phys. Plasma **9**, 2311 (2002)

[14] Ljubomir Nikolić, M. M. Škorić, S. Ishiguro, et al., Phys. Rev. E **66**, 036404 (2002)

[15] Ljubomir Nikolić, M. M. Škorić, S. Ishiguro, et al., Fusion Science Technology **43**, 359 (2003)

[16] M. M. Škorić, S. Ishiguro, Li Baiwen and Lj. Nikolić; *Intense Scattering of Relativistic Laser Light in Subcritical Plasmas*, in 'Atom, Solids and Plasmas in Super-Intense Laser Fields', Erice, Italy, 2003.

[17] Ishiguro Seiji, Nicolić Lj, Škorić M. M. and Li Baiwen; *Intense Reflection of a Relativistic Laser Pulse in Subcritical Plasmas*, to be published in Journal of Plasma and Fusion Research, Series Vol. **6**, 2004.

[18] K. Mima, M. S. Jovanović, Y. Sentoku, et al., Phys. Plasma 8, 2349 (2001)

[19] C. D. Decker, W. B. Mori and T. Katsouleas, Phys. Rev. E **50**, R3338 (1994)

[20] B. D. Fried and R. W. Gould, Phys. Fluid **4**, 139 (1961)

[21] T. H. Stix, *The Theory of Plasma waves*, McGraw-Hill, New York, 1962

[22] D. C. Montgomery, *The Theory of Unmagnetized plasma*, Gordon and Breach, New York, 1971

[23] H. Schamel, J. Plasma Phys. **13**, 139, (1975); Phys. Scr. **20**, 336 (1979)

[24] H. Schamle, Phys. Plasma **7**, 4831 (2000)

[25] J. P. Holloway and J. J. Dorning, Phys. Lett. A **138**, 279 (1989); Phys. Rev. A **44**, 3856 (1991)

[26] P. Sprangle, Cha-Mei Tang, et al., IEEE Trans. Plasma Sci. **PS-15**, 145 (1987)

[27] A. Pukhov and J. Meyer-ter-Vehn, Phys. Rev. Lett. **76**, 3975 (1996)

[28] J. Scott. Russell. *Report on waves*, Fourteenth meeting of the British Association for the Advancement of Science, 1844.

[29] A. C. Scott, *Introduction to Nonlinear Waves, in: Nonlinear Phenomena in Physics and Biology*, eds. R. Enus et al., (Plenum Press, 1980)

[30] R. Z. Sagdeev, Rev Plasma Physics **4**, 23 (1966)

[31] C. S. Gardner and G. K. Morikawa, Sc. Pep. **N40**, 9082 (1960)

[32] E. A. Kuznetsov and A. M. Rubenchik, *Soliton stability in plasmas and hydrodynamics* Phys. Reports, **142**, No.3, 103-165 (1986)

[33] S. P. Novikov, V. E. Zakharov, S. V. Manakov and L. P. Pitaevsky, *Theory of Solitons* Consultants Bureau, New York, (1984)

[34] G. Whitham, *Linear and Nonlinear Waves*, Wiley, New York, 1974

[35] V. I. Karpman, V. E. Zakharov, S. V. Manakov and L. P. Pitaevsky, *Nonlinear Wave in Dispersive Media*, pergamon, Oxford, 1975

[36] A. C. Scott, F. Chu and P. W. McLanghlin, Proc. IEEE **61**, 1447 (1975)

[37] V. E. Zakharov, S. L. Musher and A. M. Rubenchik, Phys. Reports, **129**, 285 (1985)

[38] V. E. Zakharov and E. A. Kuznetsov, Physica **18D**, 455 (1986)

[39] B. B. Kadomtsev and V. I. Petviashvili, Sov. Phys. Doclady **15**, 539 (1970)

[40] D. E. Pelinovshy, V. V. Afanasjev, and Y. S. Kivshar, Phys. Rev. E **53**, 1940, (1996)

[41] M. J. Ablowitz, H. Segur, *Solitons and Inverse Scattering Transform*, SIAM, Philadelphia, PA, 1981

[42] A. C. Neweel, *Solitons in Mathematics and Physics*, SIAM, University of Arizona, Tucson, AZ, 1985

[43] N. M. Naumova, S. V. Bulanov, et al., Phys. Rev. Lett. **87**, 185004 (2001).

[44] A. G. Litvak, Phys. JETP **30**, 344 (1969)

[45] C. E. Max and J. Arons, Phys. Rev. Lett. **33**, 209 (1974)

[46] G. Schmidt and W. Horton, Comments Plasma Phys. Control. Fusion **9**, 85 (1985)

[47] A. B. Borisov, A. V. Borovskiy, O. B. Shiryaev et al., Phys. Rev. A **45**, 5830 (1992)

[48] Guo-Zheng Sun, Edward Ott, et al., Phys. Fluids **30**, 526 (1987)

[49] M. D. Feit, A. M. Komashko and S. L. Musher, et al., Phys. Rev. E **57**, 7122 (1998)

[50] A. I. Akhiezer and R. V. Polovin, Sov. Phys. JETP **30**, 915 (1956)

[51] P. K. Kaw and J. Dawson, Phys. Fluids **13**, 472 (1970)

[52] S. V. Bulanov, T. Tz. Esirkepov, et al., Phys. Rev. Lett **82**, 3440 (1999)

[53] S. V. Bulanov, F. Califano, et al., Plasma Fusion Res. **75**, 506 (1999)

[54] K. A. Tanaka, Y. Sentoku, A. A. Offenberger, et al., Phys. Rev. E **62**, 2672 (2000)

[55] V. E. Zakharov et al., *Theory of Solitons*, New York, 1984.

[56] V. A. Kozlov, A. G. Litvak and E. V. Suvorov, Sov. Phys. JETP **49(1)**, 75 (1979)

[57] D. Farina and S. V. Bulanov, Phys. Rev. Lett. **86**, 5289 (2001)

[58] Lj. Hadžievshi, M. S. Jovanović, M. M. Skorić and K. Mima, *Stability of one-dimensional electromagnetic solitons in relativistic laser plasmas*, Phys. Plasma **9**, 2569 (2002)

[59] S. V. Bulanov, I. N. Inovenkov, V. I. Kirsanov et al., Phys. Fluids **B 4**, 1935 (1992)

[60] S. V. Bulanov, T. Th. Esirkepov, et al., Plasma Phys. Rep. **21**, 550 (1995)

[61] S. V. Bulanov and M. Lontano, Phys. Rev. Lett. **76**, 3562 (1996)

[62] S. V. Bulanov, F. Califano, et al., Phyica D 152-153, 682-693 (2001)

[63] G. A. Askar'yan, S. V. Bulanov, F. Pegoraro, et al., JETP Lett. **60**, 251 (1994)

[64] V. E. Zakharov and A. B. Shabat, Sov. Phys. JETP **34**, 62 (1972)

[65] Hsing-Hen Chen and Chuan-Sheng Liu, Phys. Rev. Lett. **37**, 693 (1976)

[66] P. K. Kaw, A. Sen, and T. Katsouleas, Phys. Rev. Lett. **68**, 3172 (1992)

[67] R. N. Sudan, Y. S. Dimant and O. B. Shiryaev, Phys. Plasma **4(5)**, 1489 (1997)

[68] S. Poornakala, A. Das, A. Sen, and P. K. Kaw, Phys. Plasma **9**, 1820 (2002)

[69] A. V. Kochetov V. A. Mironov, et al., Physica D **152-153**, 723 (2001)

[70] T. Esirkepov, F. F. Kamenets, et al., JETP letters. **68**, 36 (1998)

[71] D. Farina and S. V. Bulanov, Plasma Physics Reports, **27**, 641 (2001)

[72] M. Borghesi S. V. Bulanov, et al., Phys. Rev. Lett. **88**, 135002 (2002)

[73] T. Esirkepov, K. Nishihara, et al., Phys. Rev. Lett. **89**, 275002 (2003)

[74] Y. Sentoku, T. Zh. Esirkepov, K. Mima, et.al., Phys. Rev. Lett. **83**, 3434 (1999)

[75] Li Baiwen, S. Ishiguro, M. M. Škorić, H. Takamaru and T. Sato, *Stimulated Raman Scattering, Cascade-into-Condensate and Accleration of Large Relativistic Electromangnetic Solitons in Intense Laser Interaction with an Underdense Plasma*, to be published in Journal of Plasma and Fusion Research, Series Vol. **6**, 2004.

[76] Yuri S. Kivshar, Barry Luther-Davies, *Dark Optical Solitons: Physics and Applications*, Physics Reports, **298**, 2, (1998)

[77] S. , K. Bongs, S. Dettmer, et al., *Dark Solitons in Bose-Einstein Condensates*, Phys. Rev. Lett. **83**, 5198, (1999)

[78] C. E. Clayton at el., Phys. Rev. Lett. **70**, 37 (1993)

[79] T. Tajima and J. M. Dawson, Phys. Rev. Lett.**43**, 267 (1979)

[80] P. Sprangle et al., Phys. Rev. Lett. **69**, 2200 (1992)

[81] E. Esarey et al., Phys. Fluids B **5**, 2690 (1993)

[82] T. M. Antonsen and P.Mora, Phys. Rev. Lett. **69**, 2204 (1992)

[83] P. Chen et al., Phys. Rev. Lett. **54**, 693 (1985)

[84] J. D. Miller et al., Phys. Rev. Lett. **67**, 1747 (1991)

[85] S. C. Wilks et al., Phys. Rev. Lett. **61**, 337 (1988)

[86] S.C.Wilks et al., Phys. Rev. Lett. **62**, 2600 (1989)

[87] Li Baiwen, S. Ishiguro, M. M. Škorić, H. Takamaru and T. Sato, *Acceleration of High-Quality, Well-Collimate Return Beam of Relativistic Electrons by Intense Laser Pulse in a Low-Density Plasma*, Laser and Particle Beam, **22**, 1-7 printed in the USA, 2004.

[88] M. Tabak et al., Phys. Plasmas **1**, 1626 (1994)

[89] P. L. Shkolnikov et al., Appl. Phys. Lett. **71**, 3471-3773 (1997)

[90] J. T. Mendonca and F. Doveil, J. Plasma Phys. **28**, 485 (1982)

[91] J. T. Mendonca, Phys. Rev. A **28**, 3592 (1983).

[92] Z-M.Sheng et al., Phys. Rev. Lett. **88**, 055004 (2002)

[93] G. Shvets et al., Phys. Rev. Lett. **81**, 4879 (1998)

[94] R. W. Hockney and J. W. Eastwood, *Computer Simulation Using Particles*, McGraw-Hill, USA, 1981

[95] C. K. Birdsall and A. B. Langdon, *Plasma Physics via Computer Simulation*, McGraw-Hill, 1985

[96] Y. Omura and H. Matsumoto, *Computer Space Plasma Physics*, Terra Scientific Publishing Company, Tokyo, 1993

[97] W. B. Mori et al., Phys. Rev. Lett. **72**, 1482 (1994)

[98] W. B. Mori IEEE J. Quantum Electron. **33**, 1942 (1997)

[99] E. Esarey et al., Phys. Rev. Lett. **72**, 2887 (1994)

[100] A. Ting et al., Science **273**, 472 (1996)

[101] R. Wagner et al., Phys. Rev. Lett. **78**, 3125 (1997)

[102] K. C. Tzeng et al., Phys. Rev. Lett. **79**, 5258 (1997)

[103] D. Gordon et al., Phys. Rev. Lett. **80**, 2133 (1998)

[104] E. Esarey et al., Phys. Rev. Lett. **80**, 5552 (1998)

[105] A. J. Mackinnon et al., Phys. Rev. Lett. **88**, 215006 (2002)

[106] G. Malka et al., Phys. Rev. Lett. **78**, 3314 (1997)

[107] J. J. Santos et al., Phys. Rev. Lett. **89**, 025001 (2002)

[108] S. P. Hatchett et al., Phys. Plasmas **7**, 2076 (2000)

[109] C. Rousseaux et al., Phys. Plasma **9**, 4261 (2002)

[110] Y. Sentoku et al., Phys. Rev. E **65**, 046408 (2002)

[111] A. Zhidkov et al., Phys. Rev. Lett. **89**, 215002 (2002)

[112] R. W. Harvey et al., Phys. Fluids **18**, 1395 (1975)

[113] D. W. Forslund et al., Phys. Fluids **18**, 1002 (1975)

[114] S. Miyamoto et al., J. Phys. Soc. Jpn **67**, 1281 (1998)

[115] M. M. Skorić et al., Phys. Rev. E **53**, 4056 (1996).

[116] Robert M. Kiehn, Instability patterns, wakes and toplological limit sets